

NOAA Grant NA37RJ0202
National Oceanic and Atmospheric Administration

**SURFACE FLUXES AND BOUNDARY LAYER
RECOVERY IN TOGA COARE:
SENSITIVITY TO CONVECTIVE ORGANIZATION**

by Thomas R. Saxen

Steven A. Rutledge, P.I.

**Colorado
State
University**

**DEPARTMENT OF
ATMOSPHERIC SCIENCE**

PAPER NO. **629**

**SURFACE FLUXES AND BOUNDARY LAYER
RECOVERY IN TOGA COARE:
SENSITIVITY TO CONVECTIVE ORGANIZATION**

by

Thomas R. Saxen

Department of Atmospheric Science

Colorado State University

Fort Collins, CO 80523-1371

**Research Supported by
National Oceanic and Atmospheric Administration
under Grant NA37RJ0202**

December 1996

Atmospheric Science Paper No. 629

ABSTRACT

SURFACE FLUXES AND BOUNDARY LAYER RECOVERY IN TOGA COARE: SENSITIVITY TO CONVECTIVE ORGANIZATION

Shipboard radar data collected during the Tropical Ocean Global Atmospheres Coupled Ocean-Atmosphere Response Experiment (TOGA COARE) were used in conjunction with surface meteorological data from the Woods Hole Oceanographic Institute's Improved Meteorology (IMET) buoy to describe in detail how four different classifications of convective systems affect the atmospheric boundary layer and alter the surface fluxes of heat, moisture, and momentum. Atmospheric convective systems observed by radar were separated into four classifications based on spatial scale (sub-MCS vs. MCS scale) and horizontal morphology (non-linear vs. linear organization). Composite analyses of the surface fluxes along with the pertinent bulk variables have been constructed for each of the four classes of convective organization. During the compositing process, the convectively active and recovery periods were separated, allowing *both* of these distinctly different phases to be accurately represented in the final composite analyses.

All four types of convective organization affected the boundary layer and altered the surface fluxes in a similar manner, however, the duration and magnitude of the response was highly dependent on the type of convective organization. The sub-MCS

scale events tended to develop in environmental conditions which inhibited their upscale growth and accordingly produced the weakest and shortest response at the surface. The MCS scale events, on the other hand, tended to develop in environmental conditions which allowed the systems to intensify and organize, including strong convective scale downdrafts, which promoted a greater response at the surface. The MCS scale events also had a significant amount of stratiform precipitation associated with them which slowed the rate at which the boundary layer recovered to the pre-convective state. This, combined with the fact that the MCS scale events perturbed the boundary layer to a greater extent, accounted for the recovery phase of the MCS scale events being more than twice as long as the sub-MCS scale events.

Thomas Ronald Saxen
Department of Atmospheric Science
Colorado State University
Fort Collins, CO 80523
Spring 1997

ACKNOWLEDGMENTS

I would like to thank my advisor Dr. Steven Rutledge for the opportunity to pursue a dream and also for the guidance and support which allowed it come true. I would also like to thank Dr. David Randall and Dr. Theodore Chamberlain for serving on my graduate committee. I also graciously acknowledge all the members of the Radar Meteorology group for providing helpful comments and suggestions along the way. I would especially like to thank Tom Rickenbach and Charlotte DeMott for providing the rain rate calculation algorithm used in this study. I would also like to thank Paul Hein for always being available to answer my numerous computer related questions. Dr. Robert Weller and Mark Baumgardener of Woods Hole Oceanographic Institute are gratefully acknowledged for providing the data collected by the IMET buoy during TOGA COARE and answering questions regarding the data. This research was funded by the National Oceanic and Atmospheric Administration TOGA COARE Grant NA37RJ0202.

TABLE OF CONTENTS

1. Introduction	1
2. Scientific Background	6
2.1 Introduction	6
2.2 Background on TOGA COARE	7
2.3 Convective Organization in the COARE Region	10
2.4 The Surface Energy Budget in the Tropical Western Pacific	14
2.5 Related Results from Previous Experiments	17
2.6 Related Results from TOGA COARE	20
2.7 Convective System Effects on Upper Ocean Processes	23
3. Procedures	36
3.1 Introduction	36
3.2 Data	37
3.3 Classification of Atmospheric Convection	41
3.4 Calculation of Rain Rates	42
3.5 Calculation of Surface Fluxes	46
3.6 Compositing Scheme	54
4. Results	69
4.1 Introduction	69
4.2 Rainfall	72

4.3 Wind Stress	73
4.4 Sensible Heat Flux	75
4.5 Latent Heat Flux	80
4.6 Rainfall Heat Flux	83
4.7 Evaluation of Composites	84
5. Conclusions	106
References	112
Appendix A Individual Sub-MCS Scale Non-Linear Events	A-1
Appendix B Individual Sub-MCS Scale Linear Events	B-1
Appendix C Individual MCS Scale Non-Linear Events	C-1
Appendix D Individual MCS Scale Linear Events	D-1

LIST OF TABLES

Table 3.1	Technical specification of MIT C-band Doppler radar.	57
Table 3.2	Summary of IMET buoy instrumentation.	58
Table 3.3	Estimated accuracy of IMET buoy instruments.	59
Table 3.4	The lower boundary values of the sublayer profiles.	60
Table 4.1	Mean correlation coefficients between the individual events and the final composites.	87
Table 4.2	Comparison of current results to previous studies.	88

LIST OF FIGURES

Figure 2.1	Depiction of TOGA COARE observational domains.	28
Figure 2.2	Global map of long-term mean (1959-1989) December-February sea surface temperature.	29
Figure 2.3	Global map of December-February total diabatic heating in an atmospheric column between 700 mb and 50 mb.	30
Figure 2.4	Map of mean annual precipitation over the Pacific Ocean.	31
Figure 2.5	Example of sub-MCS scale non-linear classification of convective organization.	32
Figure 2.6	Example of sub-MCS scale linear classification of convective organization.	33
Figure 2.7	Example of MCS scale non-linear classification of convective organization.	34
Figure 2.8	Example of MCS scale linear classification of convective organization.	35
Figure 3.1	Nominal positions of observational platforms.	61
Figure 3.2	Line drawing of WHOI IMET buoy deployed in TOGA COARE.	62
Figure 3.3	Schematic illustrating the four different classifications of convective organization.	63
Figure 3.4	Summary of rain rate calculation methodology.	64
Figure 3.5	Radius of convective circle as a function of the mean reflectivity within the background area.	65
Figure 3.6	Summary of methodology used to partition reflectivity field into convective and non-convective components.	66

Figure 3.7	Schematic depicting methods used to interpolate the dBR values along a path from the radar origin to the point being corrected for attenuation.	67
Figure 3.8	Summary of the implementation of the COARE Bulk Flux Algorithm.	68
Figure 4.1	Summary of composite bin lengths for the different classifications of convective organization.	89
Figure 4.2	Composite time series of rain rate for the different classifications of convective organization.	90
Figure 4.3	Composite time series of wind speed for the different classifications of convective organization.	91
Figure 4.4	Composite time series of drag coefficient for the different classifications of convective organization.	92
Figure 4.5	Composite time series of wind stress for the different classifications of convective organization.	93
Figure 4.6	Composite time series of air temperature for the different classifications of convective organization.	94
Figure 4.7	Composite time series of the rate of temperature change for the different classifications of convective organization.	95
Figure 4.8	Composite time series of sea surface temperature for the different classifications of convective organization.	96
Figure 4.9	Composite time series of the air-sea temperature difference for the different classifications of convective organization.	97
Figure 4.10	Composite time series of the transfer coefficient for heat for the different classifications of convective organization.	98
Figure 4.11	Composite time series of sensible heat flux for the different classifications of convective organization.	99
Figure 4.12	Composite time series of specific humidity for the different classifications of convective organization.	100

Figure 4.13 Composite time series of sea surface saturation specific humidity for the different classifications of convective organization.	101
Figure 4.14 Composite time series of the air-sea humidity difference for the different classifications of convective organization.	102
Figure 4.15 Composite time series of the transfer coefficient for moisture for the different classifications of convective organization.	103
Figure 4.16 Composite time series of latent heat flux for the different classifications of convective organization.	104
Figure 4.17 Composite time series of rainfall heat flux for the different classifications of convective organization.	105

CHAPTER 1

INTRODUCTION

In recent years there has been a heightened interest in understanding climate variability on time scales of months to years in the hope that better long range forecasts can be produced. It has also become more and more apparent that in order to understand and predict climate variability, the ocean and the atmosphere must be considered together as a coupled system. The tropical W. Pacific, in particular, is thought to be the genesis region of the interannual climate variation known as El Niño-Southern Oscillation (ENSO) (see Philander, 1990 for ENSO overview). ENSO events are thought to be caused by complex interactions between the Pacific Ocean and the overlying atmosphere. During ENSO events, the warmest waters, which are usually found in the W. Pacific, migrate to the east. This tends to alter the Walker circulation which is a major component in the global general circulation of the atmosphere. Therefore, this migration of warm water in the tropical Pacific can affect the climate on the global scale.

In order to better predict climate variations such as ENSO on time scales of months to years, our understanding of the interactions between the ocean and the atmosphere needs to improve. Realizing this, the Tropical Ocean Global Atmosphere (TOGA) program designed an observational and modeling program, the TOGA Coupled Ocean-Atmosphere Response Experiment (TOGA COARE), to help gain a better

understanding of the coupled ocean-atmosphere system in the vital tropical W. Pacific region (Webster and Lukas 1992).

One of the main scientific goals of TOGA COARE was to describe and understand the processes responsible for the coupling of the ocean and the atmosphere in the tropical W. Pacific. The ocean and the atmosphere interact with each other through surface fluxes of heat, moisture, and momentum and it is known that these surface fluxes are greatly enhanced in the regions of active atmospheric convection (Gaynor and Ropelewski, 1979; Johnson and Nicholls, 1983; Young et al., 1995). These convective events can have important short term effects on the structure and thermodynamics of the upper ocean this region (Gautier, 1978; Price, 1979; Flament and Sawyer, 1995; Tomczak, 1995), but there cumulative effects on monthly to seasonal time scales remains less certain. However, recent modeling studies from TOGA COARE are beginning to indicate that the surface flux enhancements due to active convection may be an important part of the heat budget in this region. Weller and Anderson (1996) found that in order to accurately model the sea surface temperature response during the four month TOGA COARE period, the short time scale variability associated with atmospheric convection needed to be considered.

In order to gain an improved understanding of the cumulative effects that atmospheric convective systems have on the upper ocean on monthly to seasonal time scales, the effect that the individual convective systems have on the surface fluxes of heat, moisture, and momentum needs to be quantified. Previous studies have addressed the effects that atmospheric systems have on the boundary layer over tropical oceans.

These studies have typically approached the problem in one of two ways, either describing the effects of individual cases limited to squall line events (Johnson and Nicholls, 1983; Jabouille et al., 1996), or they explored the average effects of atmospheric convective systems without differentiating between any different classifications of convective organization (Gaynor and Ropelewski, 1979; Young et al., 1995)

Rickenbach and Rutledge (1996) used radar reflectivity data to identify four different types of convective organization during TOGA COARE. Their classification scheme was based on the spatial scale and horizontal morphology of the convective system. Rickenbach and Rutledge also related these different types of convective organization to the environmental conditions in which they developed. This classification scheme is used in the current study to determine how the different types of convective organization effect the boundary layer and enhance the surface fluxes of heat, moisture, and momentum.

The primary goal of the current study was to describe in detail how the different types of convective organization effect the surface fluxes during both the convectively active and boundary layer recovery time periods. In order to achieve this goal, a composite analysis of the surface fluxes, along with the pertinent bulk variables, was done for each type of convective organization. During the compositing process, the convectively active and boundary layer recovery time periods of each individual time series were separated so that the distinctly different processes occurring during the two periods were not mixed in the final composites. This practice allowed the final

composites to contain much of the detailed response present in the individual time series. These composites were the result of many individual flux time series, stratified by convective organization.

The results of the composite analyses indicate that the different types of convective organization effect the surface fluxes in a similar manner. However, the magnitude and duration of the surface flux response is dependent on the type of convective organization creating the response. This dependence can be related to the degree of organization and convective intensity, which are largely controlled by the large scale environment in which the convective system develops. Convective systems which develop in favorable environmental conditions will organize on a larger scale and intensify, leading to a greater enhancement in the surface fluxes. On the other hand, unfavorable environmental conditions will inhibit the intensification of the convective systems and the surface flux enhancements will be much weaker.

Some background on the TOGA COARE experiment will be included in Chapter 2 along with a summary of previous studies dealing with the heat budget and the organization of convection in the tropics. Results from previous studies which relate to the effects that atmospheric convective systems have on the atmospheric boundary layer and upper ocean will also be summarized in Chapter 2. The data sources used in this study along with a summary of the general analysis procedures employed are given in Chapter 3. A summary of the COARE Bulk Flux Algorithm, the methods used derive rain rates from radar reflectivity data, and a description of the compositing scheme are

also provided in this chapter. The results of this study will be presented in Chapter 4 and the conclusions will be stated in Chapter 5.

CHAPTER 2

SCIENTIFIC BACKGROUND

2.1 Introduction

In recent years there has been a dramatic increase in interest in the ocean-atmosphere coupling in the tropical W. Pacific, in part due to evidence which indicates that the tropical W. Pacific is the origin of the ENSO phenomena which has climate variation implications on a world-wide scale (Horel and Wallace, 1981; Rasmusson and Wallace, 1983; Philander, 1990). Prior to the 1990's the majority of the observational data from the tropical oceanic environment came from the GATE experiment which took place in the Atlantic in 1974. Because of the lack of observational data from the tropical W. Pacific, the international community organized a combined oceanographic and atmospheric experiment (TOGA COARE) to obtain an unprecedented dataset to study the air-sea coupling in this vital region.

The goal of the present study is to gain a better understanding of how the different types of convective systems observed during TOGA COARE affect the surface fluxes of heat, moisture, and momentum. A number of studies related to this goal came out of previous field experiments and a few are starting to appear in the literature from TOGA COARE. Some of these results will be summarized below. Some background on TOGA COARE will also be presented along with an overview of the organization of

convection in the COARE region. A discussion on the heat budget of the tropical W. Pacific will be included and lastly, a discussion on how convective systems can affect upper ocean processes will be presented.

2.2 Background on TOGA COARE

As part of the TOGA program, which is a major component of the World Climate Research Programme (WCRP), it was deemed that the tropical Pacific Ocean is the most important region to consider when trying to understand climate variability (WCRP, 1990; Webster and Lukas, 1992). However, there was a lack of comprehensive, high quality datasets which covered all of the different spatial and temporal scale processes that occur in the ocean and the atmosphere in this vital region. Realizing this, the TOGA program designed an observational and modeling program (TOGA COARE) to provide an unprecedented dataset from which the international scientific community can study the complex interactions between the ocean and the atmosphere in this vital region. This new, comprehensive dataset was to be used to further our understanding of the physical processes occurring in this region and to aid in the improvement of atmospheric, oceanic, and coupled ocean-atmosphere models.

During the planning stages of TOGA COARE four general scientific goals of the program were established. They were to describe and understand:

- 1) the principle processes responsible for the coupling of the ocean and the atmosphere in the W. Pacific warm-pool system;
- 2) the principle atmospheric processes that organize convection in the warm-pool region;

- 3) the oceanic response to combined buoyancy and wind-stress forcing in the W. Pacific warm-pool region; and
- 4) the multiple-scale interactions that extend the oceanic and atmospheric influence of the W. Pacific warm-pool system to other regions and vice versa.

The aim of this study is directed towards achieving the first goal in this list.

The observational component of TOGA COARE took place during an Intensive Operation Period (IOP), which ran from November 1992 through February 1993. Multifaceted observations were obtained within the Intensive Flux Array (IFA) centered at 2° S, 156° E with its outer boundaries defined by the meteorological sounding stations at Kapingamaringi and Kavieng, and ships positioned near 2° S, 158° E and 4° S, 155° E. The majority of the atmospheric and oceanic data, including that used in this study, was collected within the IFA during the IOP. Two larger COARE domains included the Outer Sounding Array (OSA) and the Large-Scale Domain (LSD). The OSA was centered around the IFA and its outer boundaries were defined by the meteorological sounding stations at Truk, Pohnpei, Nauru, Honiaria, Misima, and Manus. The LSD was defined by the region within 10° N to 10° S and 140° E to 180°. These three regions are depicted in Fig. 2.1. The IOP was also augmented by atmospheric and oceanic enhanced monitoring periods which ran from July 1992 through July 1993 and September 1991 through October 1993 respectively.

The observational domain described above was chosen for a number of reasons. First of all, this region is found in the W. Pacific warm pool where the sea surface

temperatures (SSTs) are generally greater than 29° C (Fig. 2.2). This region of warm surface waters helps produce an extensive region of atmospheric diabatic heating above it (Fig. 2.3). A major component of this diabatic heating comes from the latent heat that is released in the atmosphere as a result of the large amount of precipitation that falls in this region. It has been estimated that over 3 m of rain falls on this region each year with maxima of over 5 m per year (Fig. 2.4). This large amount of precipitation leads to an estimated net freshwater flux into the ocean of 1 - 2 m per year. This large net freshwater input tends to help stabilize the upper ocean in this region by creating a halocline which is usually shallower than the thermocline (Lukas and Lindstrom, 1991). This leads to a shallower oceanic mixed layer which can have important thermodynamic and dynamic implications (Godfrey and Lindstrom, 1989; Lukas and Lindstrom, 1991).

During TOGA COARE, an unprecedented oceanographic/atmospheric dataset was collected from a number of different types of platforms; including islands, buoys, ships, aircraft, and satellites. Surface meteorological data was obtained from island sites, buoys, and ships. Upper air meteorological data was obtained from island sites, ships, and aircraft. Oceanographic data was obtained from buoys and ships. Two of the ships and three of the aircraft involved in TOGA COARE also carried Doppler radars providing information on the structure and kinematics of precipitating systems. Satellite observations were carried out by both geosynchronous and polar orbiting satellites, thus providing information about a number of geophysical variables including radiation, clouds, sea surface temperature, ocean surface level, surface wind speed, atmospheric moisture and temperature profiles. Webster and Lukas (1992) provide a more complete

discussion of the experimental design including a listing of observational platforms employed and the measurements that were made during the experiment.

2.3 Convective Organization in the COARE Region

As stated in the previous section, one of the main goals of TOGA COARE was to describe and understand the organization of convection in the warm pool region. This has proven to be a difficult problem since convection in the tropical W. Pacific is extremely complex, occurring at a wide range of temporal and spatial scales (Sui and Lau, 1992; Chen et al., 1996; Rickenbach and Rutledge, 1996). These different scales also tend to interact with each other which adds even more complexity to the problem (Sui and Lau, 1992). Understanding the organization of convection in the tropical W. Pacific is crucial to achieving the overall goal of TOGA COARE (i.e. understanding the physical processes responsible for the coupling of the ocean and the atmosphere in the region) since the ocean and the atmosphere interact with each other through the surface fluxes of heat, moisture, and momentum. These surface fluxes are greatly enhanced in regions of active convection.

During the COARE experiment, there were two ships with Doppler radars on board which gave a nearly continuous picture of the evolving structure of the precipitating systems that developed over the W. Pacific warm pool (Rutledge et al., 1993). These radars had a distinct advantage over the radars on aircraft in that they provided a near continuous sample of convection whereas the aircraft provided more or less snapshots of convective systems. The shipboard radars also provided information about the internal structure of these precipitating systems at a high time resolution which

can not be deduced with satellite data. Therefore, the shipboard radars provided an excellent avenue for studying the organization of convection in this region.

Rickenbach and Rutledge (1996) used reflectivity data in conjunction with radiosonde data to study the organization of convection during TOGA COARE. The reflectivity data was obtained by the Massachusetts Institute of Technology (MIT) C-band Doppler radar, located on board the R/V Vickers which was positioned near 2° S 156° E for approximately 90 days during the COARE IOP (three - 30 day deployments). Rickenbach and Rutledge examined the horizontal morphology, the frequency of occurrence, and the rainfall production of convection during TOGA COARE. They also related the organization of convection to the larger scale atmospheric environment. The systems were classified as Mesoscale Convective System (MCS) scale if there was contiguous radar echoes with a spatial scale of at least 100 km in length and sub-MCS scale if the spatial scale of the radar echoes were less than 100 km in length. The systems were also classified based on horizontal morphology. The systems were classified as linearly organized if they were organized in a line-like fashion and randomly organized if no linear features were observed. This classification scheme, which is the similar to the classification scheme used in the present study, provided four general types of convective organization; each of which will be discussed below.

Figure 2.5 provides an example of the sub-MCS scale non-linear type of convective organization. These events were the most frequently observed type of convective organization, being present about half of the time. It was also determined that these events produced a small, but non-negligible portion (16%) of the total rainfall

observed by the MIT radar during the 90 days that the R/V Vickers was on station during TOGA COARE. Even though these events occurred so frequently, they are spatially small compared to the other types of convection organization and hence they produced a small portion of the total rain. Sub-MCS scale non-linear events typically occurred during periods of weak ascent throughout the troposphere and deemed to be more prevalent during periods of weak horizontal flow. The environment condition which best distinguished the sub-MCS scale non-linear events from the other types of convective organization was a troposphere that was considerably drier compared to the other modes of convective organization. Rickenbach and Rutledge (1996) suggested that this may have limited the vertical development of the convective cells for this class of convective organization.

Figure 2.6 provides an example of the sub-MCS scale linear type of convective organization. The length of the lines for this type was defined to be between 50 km and 100 km with lines shorter than 50 km in length being classified as sub-MCS scale non-linear events and lines longer than 100 km being classified as MCS scale linear events. Because of this limitation, sub-MCS scale linear events were observed only about 10% of the time and produced about a tenth of the total observed rainfall. These events typically did not have a significant trailing stratiform precipitation region and furthermore tended to develop during periods characterized by strong tropospheric shear, dry mid level air, strong low level winds, and strong ascent below 650 mb. Rickenbach and Rutledge (1996) hypothesized that the dry mid level air and strong shear may have inhibited these events from growing into MCS scale events.

Figure 2.7 provides an example of the MCS scale non-linear type of convective organization. These events were present about 10% of the time and produced nearly 30% of the total rainfall observed by the radar. MCS scale non-linear events typically developed during periods when the troposphere was very moist and there was strong ascent throughout the troposphere. As a result, these events generally contained very deep convective features (15 - 16 km) which dominated the rainfall production (Rickenbach and Rutledge, 1996).

Figure 2.8 provides an example of the MCS scale linear type of convective organization. These events were present about 30% of the time and produced approximately 50% of the total rainfall observed by the radar. A significant trailing stratiform precipitation region was also generally associated with these events. This type of convective organization typically occurred during periods of strong mid-level convergence and strong ascent in the mid and upper-levels of the troposphere. They were also more common during strong low-level winds and deep tropospheric shear.

The radar study of Rickenbach and Rutledge (1996) provided a mesoscale description of convective organization during TOGA COARE. Satellite data, which gives a larger scale perspective compared to the radar, has also been used to study the organization of convection in the tropical W. Pacific. Chen et al. (1996) used hourly infrared (IR) satellite images from the Japanese Geosynchronous Meteorological Satellite to study the multiscale variability of convection and its relation to the larger scale environment during TOGA COARE. Infrared temperatures served as an indicator of deep convection. They used IR temperature thresholds of 235 K to indicate high

cloudiness associated with deep convection and 208 K to indicate very cold (deep) cloud.

Chen et al. (1996) found that the greatest modulator of convection during the COARE IOP was the passage of three Inter-Seasonal Oscillations (ISOs) with the active phase of each ISO being separated by a period of suppressed convection. The active phase of the ISOs were indicated by the eastward propagation of anomalous westerlies at low levels and increased convective activity indicated by increased values of percent high cloudiness using the 235 K threshold. Chen et al. observed westward propagating disturbances, which had periods of about two days, embedded within this eastward propagating region of enhanced convection.

Chen et al. (1996) also examined the size distributions of the cloud clusters. They found that the small cloud clusters ($< 6,800 \text{ km}^2$) were the most common, being present more than 80% of the time while the largest cloud cluster ($> 92,800 \text{ km}^2$) were only observed on about 10% of the days during the IOP. During the active phase of the ISO they observed a dramatic increase in the total number of cloud clusters. They also found that the largest cloud clusters typically occurred during the active phase of the ISO with mostly small clusters being observed during the suppressed period.

2.4 The Surface Energy Budget in the Tropical Western Pacific

The surface energy budget in the tropical W. Pacific has very important implications because it plays a major role in controlling the SST. The accurate determination of the surface energy budget in the tropical W. Pacific has proven to be a

difficult task. A number of studies of the heat budget in the equatorial Pacific have been conducted using climatological data and a wide range of net surface heating values have emerged. Esbensen and Kushnir (1981) found a net surface heating of about 30 W m^{-2} in the tropical W. Pacific, Weare et al. (1981) found values around 50 W m^{-2} , and Reed (1985) found values around 70 W m^{-2} . Until the heat budget in the tropical W. Pacific is determined with a higher degree of accuracy, the success of coupled ocean-atmosphere models will likely be limited.

The surface energy budget can be expressed in the following manner (Weare et al., 1981; Reed, 1985):

$$Q_N = Q_{sw} - Q_{LW} - Q_{LH} - Q_{SH}$$

where: Q_N is the net surface heating,
 Q_{sw} is the absorbed shortwave radiation at the surface,
 Q_{LW} is the net loss of longwave radiation at the surface,
 Q_{LH} is the surface latent heat flux, and
 Q_{SH} is the surface sensible heat flux.

The dominant terms in the surface energy budget are the absorption of shortwave radiation and the latent heat flux which have been estimated to be between 200 and 250 W m^{-2} , and 100 and 200 W m^{-2} respectively (Weare et al., 1981; Reed, 1985). The typical climatological values of the other terms are much smaller, with the net loss of longwave radiation at the surface being around 30 W m^{-2} and the sensible heat flux being around 10 W m^{-2} (Weare et al., 1981; Reed, 1985).

A more complete expression for the surface energy budget would include two additional terms which would account for the sensible heat flux associated with rainfall (Gosnell et al., 1995) and the removal of heat by oceanic transport. On time scales on the order of years, Flament and Sawyer (1995) have estimated the sensible heat flux associated with rainfall to be around 7 W m^{-2} in the tropical W. Pacific. This was deduced using an average annual rainfall of 3 m. The removal of heat by oceanic transport can be separated into a vertical mixing component and an advective (both horizontal and vertical) component. The vertical mixing component is generally thought to be small because of the existence of a near surface, salt stratified isothermal layer in the tropical W. Pacific (Lukas and Lindstrom, 1991). This near surface salt stratification acts to effectively inhibit the vertical mixing of heat except during sustained strong wind periods such as those observed during westerly wind bursts (Godfrey and Lindstrom, 1989). The horizontal advection component is thought to be small in the tropical W. Pacific (McPhaden and Hayes, 1991). The vertical advection component can play a significant role along the equator during upwelling or downwelling episodes (McPhaden et al., 1990).

The large scale environment, along with its resulting effects on atmospheric convection, can act to modulate the surface energy budget on interseasonal time scales. During the active phase of the ISO, atmospheric convective activity is enhanced and the upper ocean undergoes a net cooling due largely to enhanced wind speeds and reduced incoming solar radiation associated with extensive cloud cover. On the other hand,

during the suppressed phase of the ISO, the upper ocean undergoes a net heating due to weak winds and strong incoming solar radiation (Anderson et al., 1996).

On shorter time scales, the surface energy budget has even more variability which can be attributed to atmospheric convection. In the vicinity of atmospheric convection, the latent and sensible heat fluxes are known to be greatly enhanced (Gaynor and Ropelewski, 1979; Johnson and Nicholls, 1983; Young et al., 1995; Jabouille et al., 1996) and the heavy precipitation which often results can lead to the sensible heat associated with rainfall being very large (Flament and Sawyer, 1995; Gosnell et al., 1995). Convective systems also act to greatly reduce the incoming solar radiation due to enhanced cloudiness. For these reasons atmospheric convective systems generally result in a net upper ocean cooling (Gautier, 1978).

What effect the shorter term variations in the surface energy budget have on longer time scales is not known at this time. However it is known that the tropical SST is sensitive to wide range of spatial and temporal scale processes that interact with each other in a complex way (McPhaden and Hayes, 1991; Hartmann and Michelsen, 1993). Determining the significance of short time scale processes on longer time scales is a specific goal of TOGA COARE (Webster and Lukas, 1992).

2.5 Related Results from Previous Experiments

Previous field experiments, such as the GATE experiment which took place in the tropical E. Atlantic Ocean in the summer of 1974, provide some background on atmospheric convection that develops in a tropical oceanic environment. Air motions

within the convective systems were deduced using radar, aircraft, sounding, and ocean surface data. The effects that these air motions have at the surface were also inferred leading to an assessment of how these system affected the surface fluxes of heat, moisture, and momentum. The types of systems that were previously studied were mainly squall lines with significant trailing stratiform regions. A review of some of these works will be discussed below.

Tropical squall lines have certain airflow characteristics which can have pronounced effects at the surface. The convective scale downdraft, which occurs in the heavy precipitation region of the squall line itself, brings air from the mid to upper troposphere down to the surface (Zipser, 1969, 1977; Gamache and Houze, 1982). The convective scale downdraft is induced by precipitation loading and evaporational cooling and results in the formation of a gust front at the leading edge of the squall line. The air within the convective scale downdraft is generally significantly cooler and slightly drier than the environmental surface air. However, observations have indicated that air within the gust front can either be drier or more moist relative to the environmental air (Addis et al., 1984). The convective scale downdraft also causes the wind speeds to be enhanced in the gust front region.

Another type of air motion within tropical squall lines that can affect the surface layer is the mesoscale downdraft. The sinking motion within the mesoscale downdraft, which is induced by the evaporation of precipitation below the base of the trailing stratiform region, occurs over a much larger area and is weaker than the convective scale downdraft (Zipser, 1977; Gamache and Houze, 1982). The mesoscale downdraft, which

is typically warm and dry, often does not reach the surface due to its weak sinking motion not being able to break through the low level stable layer created by the convective scale downdraft (Zipser, 1977). Since the mesoscale downdrafts often do not reach the surface, their effects are much more subtle. Zipser (1977) hypothesized that the mesoscale downdrafts helped to maintain a shallow mixed layer in the stratiform region. He also observed that the lowest dew point temperatures were observed 3 - 5 hours after the passage of the squall line. He attributed this to the entrainment of dry air from the mesoscale downdraft into the low level stable layer.

It is clear that the above described features, especially the convective scale downdraft, can modify the boundary layer and alter the surface fluxes of heat, moisture, and momentum. During GATE, Gaynor and Ropelewski (1979) found a boundary layer modified by convection about 30% of the time. They also found that in the region of the density current (or gust front), the surface sensible heat flux was clearly enhanced, but they did not find any conclusive changes in the latent heat flux or wind stress. Johnson and Nicholls (1983) also found a dramatic increase in the sensible heat flux in the region of the gust front, however they also observed a significant increase in the latent heat flux. It should be noted here that the results of Johnson and Nicholls (1983) are for one particular squall line case from GATE whereas the results of Gaynor and Ropelewski (1979) were based on a composite analysis of 137 disturbances observed during GATE.

Barnes and Garstang (1982) analyzed the modifications of the boundary layer energetics by precipitating convection using moist static energy arguments. A change in the moist static energy can be brought about in two ways; by a drop in air temperature or

by a drop in specific humidity. Note that a change in height can also change the moist static energy, but Barnes and Garstang used data from a sensor whose height was constant. In light rain cases, they found that the changes in the moist static energy were small because the drop in air temperature was basically balanced by an increase in specific humidity. They hypothesized that these cases lacked strong, penetrative convective scale downdrafts which would have brought cool, dry air down to the surface. The heavy rain cases, which they hypothesized had penetrative downdrafts, showed a distinct drop in moist static energy due to the combined effects of a drop in air temperature and a drop in specific humidity.

The above described studies show that precipitating convective systems can significantly alter the properties of the boundary layer thereby leading to enhanced surface fluxes. These studies have generally examined mostly squall line type systems observed during GATE. During TOGA COARE, while squall line type systems were frequently observed, other specific types of convective organization were also observed (Rickenbach and Rutledge, 1996). The effect that these other types of convective organization have on the boundary layer has not been systematically determined and thus is the general goal of the current study.

2.6 Related Results from TOGA COARE

Recently, a number of studies dealing with the modification of the boundary layer and the enhancement of fluxes in the wakes of atmospheric convection have started to appear in the literature. Young et al. (1995) used hourly averaged data to study the modifications of the boundary layer in convective wakes and Jabouille et al. (1996) used

a cloud-resolving model to study the enhancement of the surface fluxes by atmospheric convection.

Young et al. (1995) analyzed 42 convective wakes in the tropical W. Pacific using hourly averaged data collected on the R/V Wecoma during a COARE pilot cruise and the R/V Moana Wave during TOGA COARE. They produced composite time series of a number of atmospheric variables to describe the evolution of convective wakes in the tropical W. Pacific. The composites were produced by separating each of the 42 convective wakes into six equally spaced bins with a one hour pre-storm bin and a one hour post-wake bin, thus giving eight total bins. The start time of the convective wake was determined using a minimum rain rate criteria of 2 mm hr^{-1} . The end of the wake recovery period was assumed when either the value of the sea surface temperature minus the air temperature became equal to or less than zero or the five hour running mean air temperature began to decrease. Because they were using hourly averaged data, only wakes lasting six hours or longer were considered.

The composite analysis of Young et al. (1995) found that the latent and sensible heat fluxes and the wind stress were markedly enhanced by the effects of atmospheric convection. They found that the latent heat flux, the sensible heat flux, and the wind stress increased by about 50% to 100%, 300%, and 200% to 500% respectively. They attributed the increased latent heat flux and wind stress to enhanced wind speeds caused by convective scale downdrafts. The wind stress showed the largest enhancements because it is proportional to $|U|^2$ whereas the heat fluxes are proportional to $|U|$. They attributed the increased sensible heat flux to the combined effect of enhanced wind speed

and a distinct drop in air temperature. In their study they also hypothesized that the enhancements in the wind speeds due to atmospheric convection were independent of the pre-convective environmental wind speed.

Jabouille et al. (1996) used a cloud resolving model to simulate two convective events which were observed during TOGA COARE. The first event that they simulated occurred on 26 November 1992 and the second occurred on 17 February 1993. The 26 November case was characterized by weak surface winds (2 m s^{-1}), large scale ascent, and moderate shear in the lower levels, while the 17 February case was characterized by moderate surface winds (about 4 m s^{-1}) and a lack of large scale ascent. The resulting surface flux enhancements were similar for both cases with latent and sensible heat flux enhancements of approximately 200% and 300% respectively. They also found that the latent heat flux enhancements were generally limited to the gust front region whereas the sensible heat flux enhancements occurred over a larger area. This was because the wind speed enhancements, which were generally confined to the gust front region, were largely responsible for the increase in the latent heat flux (i.e. the humidity changes played a very limited role.). The sensible heat flux, on the other hand, was enhanced not only by increased wind speeds, but also by the drop in air temperature which occurred throughout the region of rainfall.

The studies of Young et al. (1995) and Jabouille et al. (1996) both showed that atmospheric convective systems cause significant enhancements in the surface fluxes. However, their studies did not systematically determine how the surface flux response

varies with different types of convective organization. The goal of the current study is to address this issue.

2.7 Convective System Effects on Upper Ocean Processes

It is known that individual convective systems can have a dramatic affect on the stability and thermal structure of the upper ocean (Elliott, 1974; Gautier, 1978; Price, 1979; Flament and Sawyer, 1995; Tomczak, 1995). However, the effects that these convective systems have on monthly to seasonal time scales is not well understood. Determining if the short time scale variations in the surface fluxes of heat, moisture, and momentum associated with atmospheric convection are significant on monthly to seasonal time scales is a specific goal of TOGA COARE (Webster and Lukas, 1992). The effects that individual convective systems have on the oceanic mixed layer will be discussed below along with a brief summary of some of the longer term effects.

In the tropics, atmospheric convective systems are known to have a cooling affect on the upper ocean because of the effects of rainfall, reduced solar insolation, and enhanced heat fluxes. Rainfall in the tropics has a cooling effect on the ocean surface because the temperature of the rainfall, which is known to be approximately at the local wet-bulb temperature (Gosnell et al. 1995), is typically less than the SST. Therefore, there is a sensible heat flux associated with rainfall (Gosnell et al., 1995). Flament and Sawyer (1995) and Gosnell et al. (1995) found that during heavy rain events the sensible heat flux due to rainfall can be very large (often $> 100 \text{ W m}^{-2}$). During the event which Flament and Sawyer (1995) examined, the sensible heat flux due to rainfall accounted for about 40% of the net heat flux during the time period when rain was observed. On

longer time scales the effect was much reduced. Flament and Sawyer (1995) deduced an annual sensible heat flux due to rainfall of approximately 7 W m^{-2} , which was about 23% of the maximum net heat flux deduced by Gent (1991). Using data obtained from the R/V Moana Wave during TOGA COARE, Gosnell et al. (1995) deduced an average sensible heat flux due to rainfall of between 2.1 W m^{-2} and 2.5 W m^{-2} , which was about one fifth of the average sensible heat flux. Therefore, the effects of rainfall on the heat budget of the upper ocean are certainly important during periods of rainfall and may even be important on longer time scales.

Convective systems can also affect the upper ocean's thermal structure through the local enhancements of the sensible and latent heat fluxes. Gautier (1978) used aircraft radiometer data to show that there were SST depressions of over 1.5 K in the downdraft region of an active convective system during GATE. Gautier hypothesized that the SST depressions were largely caused by enhanced latent and sensible heat fluxes in the downdraft region. The enhancements in the heat fluxes were the result of decreases in the surface air temperature and increases in the surface wind speed in the region of the convective scale downdraft which was observed. Gautier also concluded that the observed SST depressions could not have been caused by effects of rainfall alone and that both the enhancements of the surface heat fluxes and the effects of precipitation needed to be included to account for the observed SST drop.

Atmospheric convective systems can also affect the structure of the upper ocean by altering the surface layer salinity. During heavy rain events, freshwater, which is less dense than salt water, is deposited on the ocean surface resulting in a buoyancy flux

which tends to create a near surface, salt stratified layer (Elliott, 1974; Price, 1979; Tomczak, 1995). Price (1979) studied a heavy rainfall event (approximately 6 cm of rain fell in less than 2 hours) which occurred on the west Florida continental shelf in 1972. He found that after the rainfall ceased, a shallow, rain-formed mixed layer had developed. The rain-formed mixed layer that Price observed was initially about 7 m deep, but wind mixing caused it to immediately start to deepen and after 20 hours the mixed layer had returned to its initial, pre-rainfall depth of 25 m. Elliott (1974) observed similar phenomena during BOMEX, however the post-rainfall deepening was much more rapid in the cases he examined. During TOGA COARE Tomczak (1995) also observed regions of decreased salinity which were attributed to rainfall. In one of the cases Tomczak examined the salinity anomalies were confined to the upper 6 m of the ocean and in another they extended downward to the base of the mixed layer. Tomczak deduced that if the decrease in density due to decreased salinity was smaller than the increase in density due to decreased temperature, oceanic convection occurred within the mixed layer and the salinity anomalies thus reached down to the base of the mixed layer. However, if the opposite occurred, oceanic convection would not occur and the salinity anomalies would be confined to the near surface layer.

Lukas (1990a,b) hypothesized that near surface salt stratification due to precipitation makes the upper ocean much more responsive to surface forcing. Since the upper ocean is stratified, surface fluxes of heat and momentum are confined to the layer above the stratification. Miller (1976) compared mixed layer ocean model simulations which did not include salinity effects to simulations which did include salinity. In one of

his simulations the halocline was 10 m shallower than the thermocline and he found that by including salinity in the model, the rate at which the mixed layer deepens was reduced and the heating characteristics of the mixed layer were altered. Miller concluded that during periods of heavy rainfall the surface fluxes are restricted to the rain-formed surface stable layer.

As stated in Sec. 2.2, the tropical W. Pacific is a region which receives 3 - 5 m of rainfall annually (Taylor, 1973). Evaporation in this region also tends to be limited because the winds are typically very weak (Weare et al., 1981). The combined effects of heavy precipitation and reduced evaporation lead to an estimated freshwater flux into the W. Pacific warm pool of 1 - 2 m yr⁻¹ (Weare et al., 1981; Donguy, 1987). Lukas and Lindstrom (1991) have hypothesized that this large freshwater flux into the W. Pacific warm pool aids in the creation of a halocline that is often shallower than the thermocline. The layer between the bottom of the halocline and the top of the thermocline has been called the barrier layer, because the entrainment of cooler water from below the thermocline is inhibited by the shallower salt stratification except during sustained strong wind events such as westerly wind bursts. This implies that very little heat is transferred through the base of the mixed layer except during periodic strong wind events which effectively mix down through the shallow halocline. This has important implications for the heat budget of the upper ocean.

It is still uncertain what *cumulative* effect convective systems have on the thermal structure and dynamics of the upper ocean. However, Weller and Anderson (1996) have shown that in order to accurately model the upper ocean thermal response during the four

month COARE period, the short time scale variations associated with atmospheric convective systems needed to be considered. One objective of the current study is to provide a dataset by which ocean modelers can examine these issues along with any other effects that convective systems may have on the upper ocean on longer time scales.

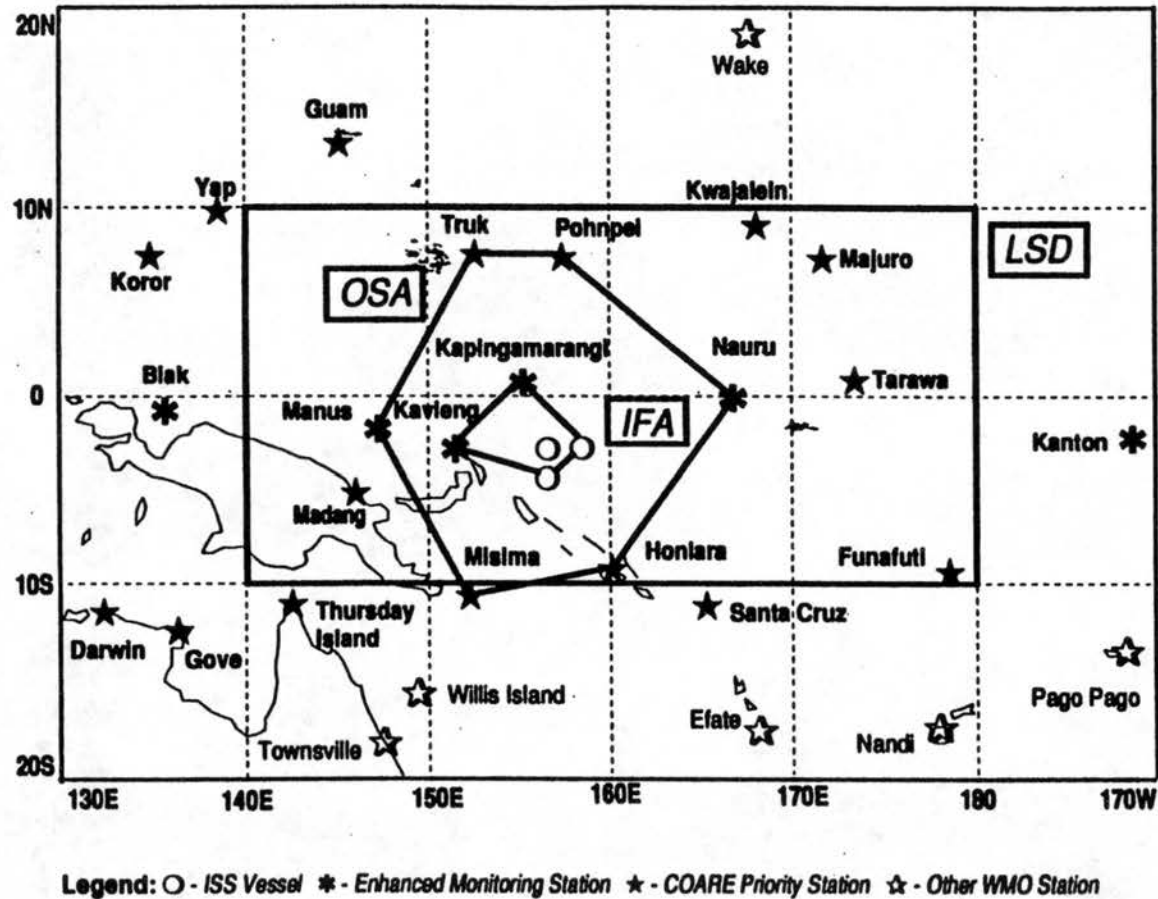


Figure 2.1 Depiction of the COARE observational domains. The Large-Scale Domain (LSD), Outer Sounding Array (OSA), and Intensive Flux Array are shown (Webster and Lukas, 1992).

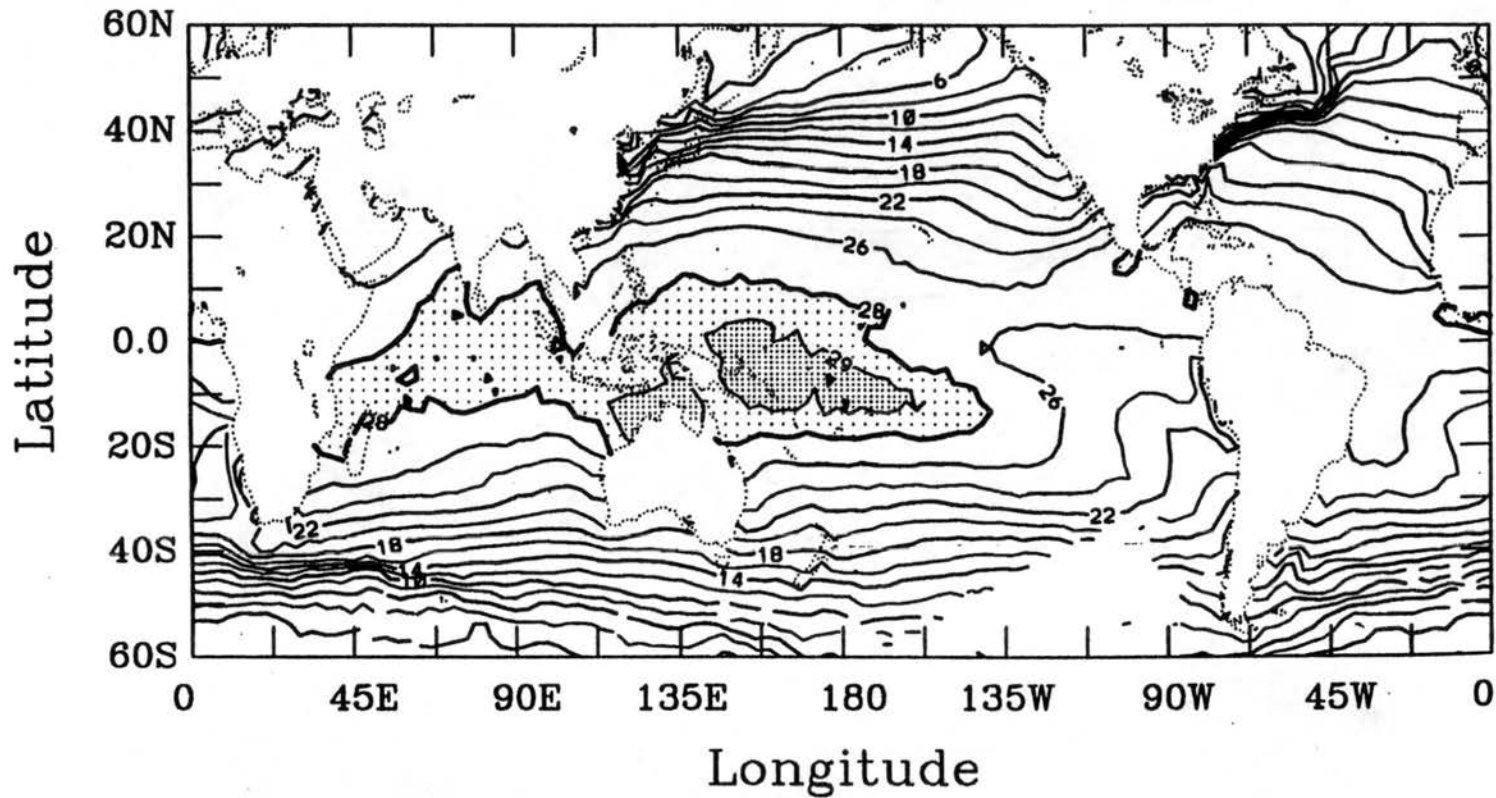


Figure 2.2 Global map of long-term mean (1959-1989) December-February SST ($^{\circ}$ C). Shaded regions indicate temperatures greater than 28° C. Data from COADS and figure from Webster and Lukas (1992).

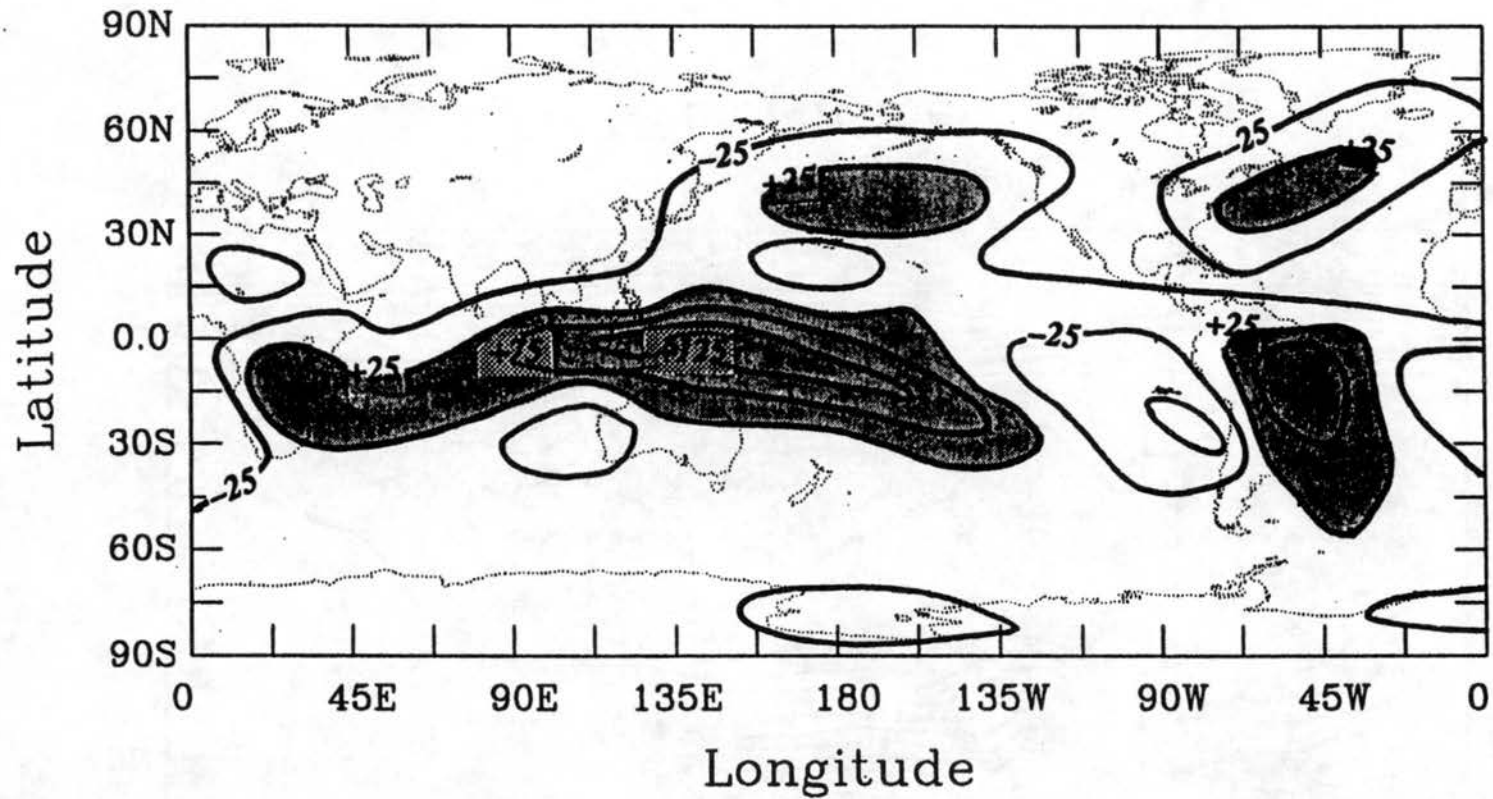


Figure 2.3 Global map of total diabatic heating (W m^{-2}) for December-February (1983-1989) in an atmospheric column between 700 mb and 50 mb (from Hoskins et al., 1989). Contour interval is 50 W m^{-2} and the shaded areas represent regions in excess of 25 W m^{-2} .

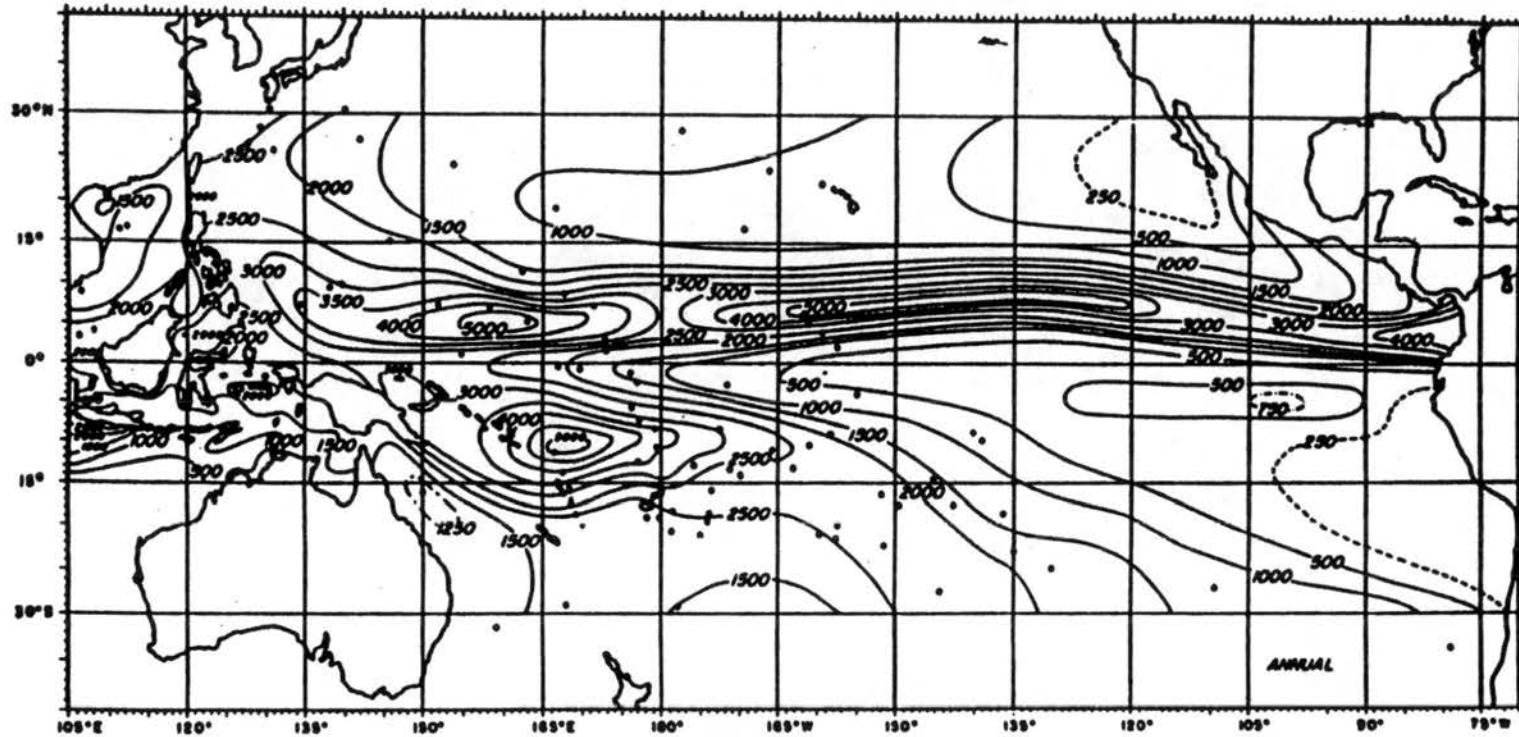


Figure 2.4 Map depicting the mean annual precipitation (mm) in the Pacific. Calculated from long-term time series of tropical island precipitation (Taylor, 1973). Contour interval is 500 mm.

02 DEC 92 Sub-MCS Scale Non-Linear

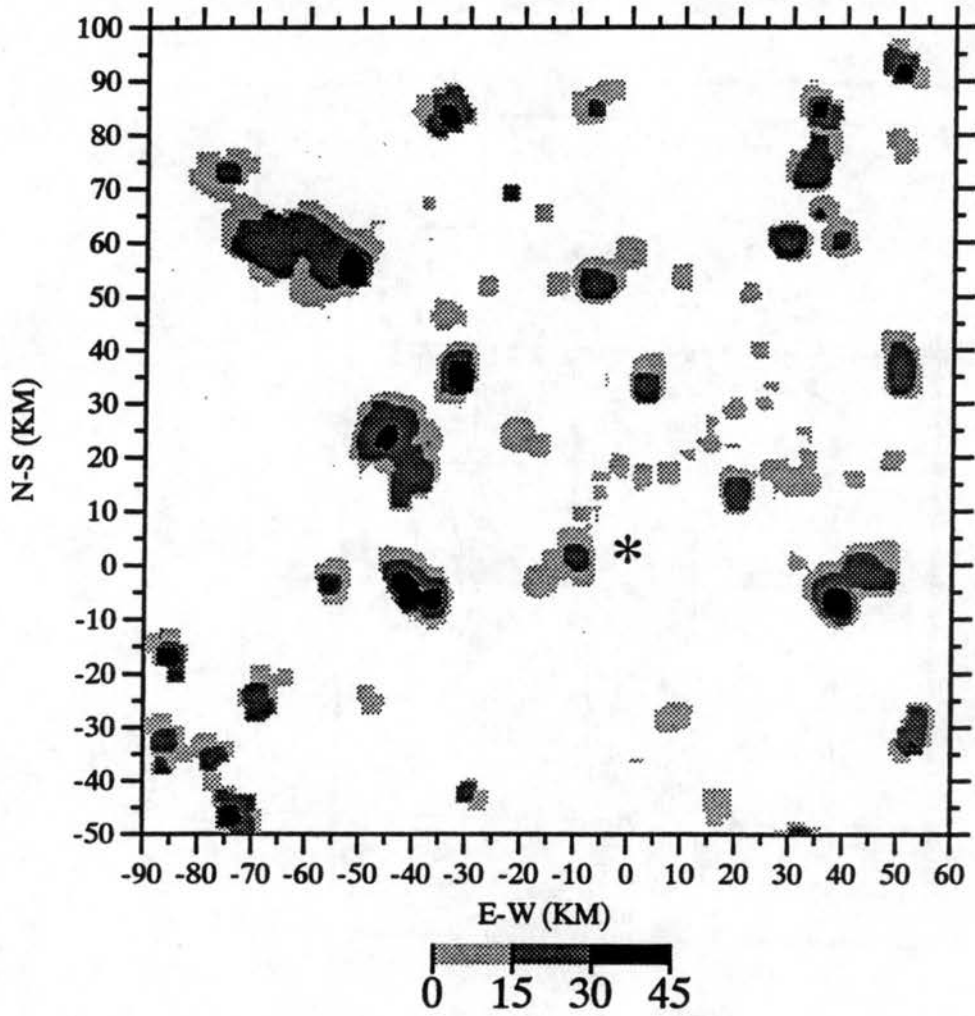


Figure 2.5 Radar image depicting an example of a sub-MCS scale non-linear event from 02 Dec. 1992. The values shown are reflectivity in dBZ. The plot origin is the nominal position of the R/V Vickers.

27 DEC 92 Sub-MCS Scale Linear

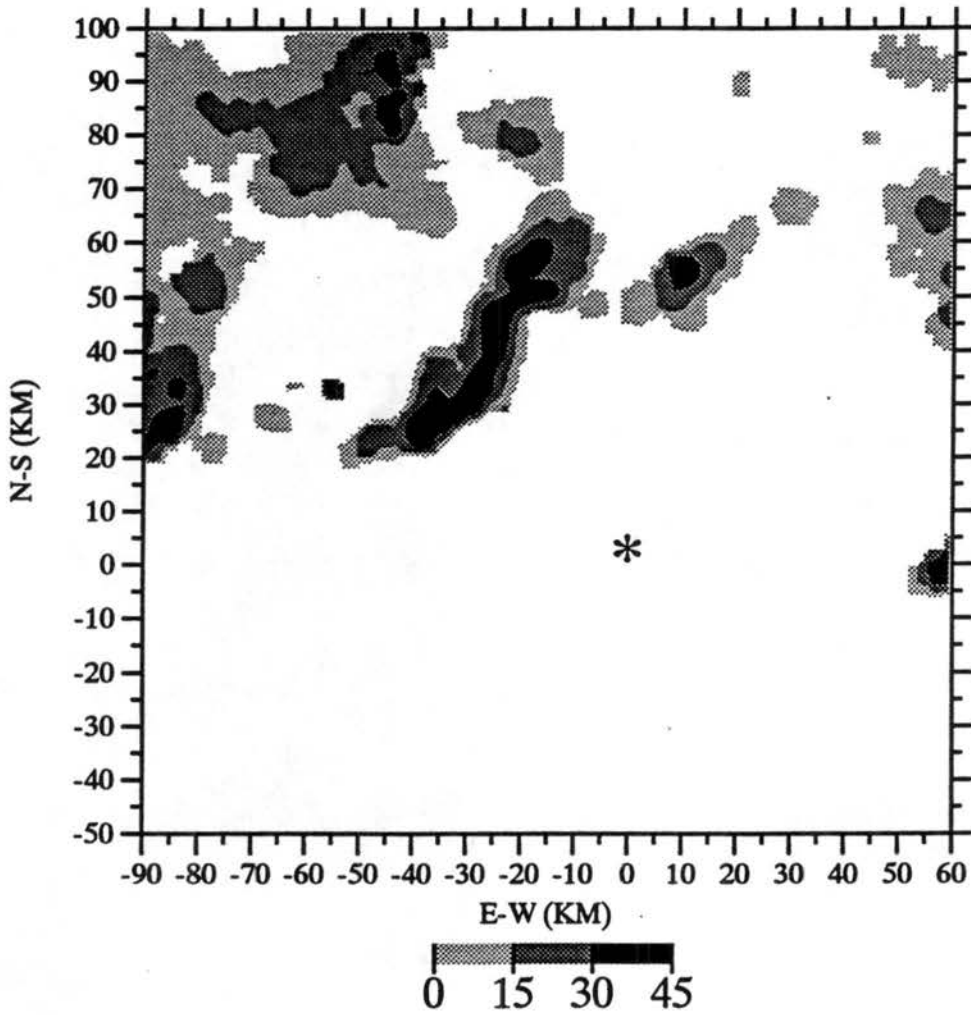


Figure 2.6 Radar image depicting an example of a sub-MCS scale linear event from 27 Dec. 1992. The values shown are reflectivity in dBZ. The plot origin is the nominal position of the R/V Vickers.

17 JAN 93 MCS Scale Non-Linear

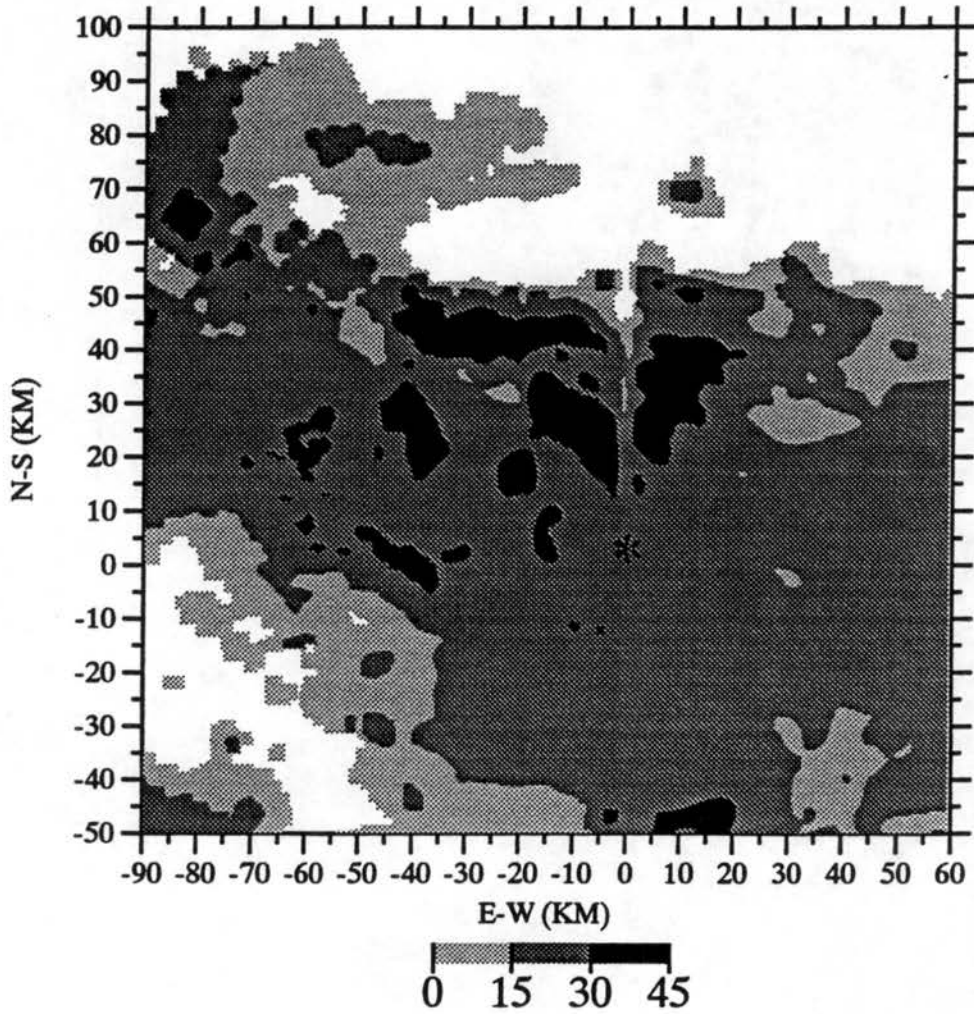


Figure 2.7 Radar image depicting an example of a MCS scale non-linear event from 17 Jan. 1993. The values shown are reflectivity in dBZ. The plot origin is the nominal position of the R/V Vickers.

10 FEB 93 MCS Scale Linear

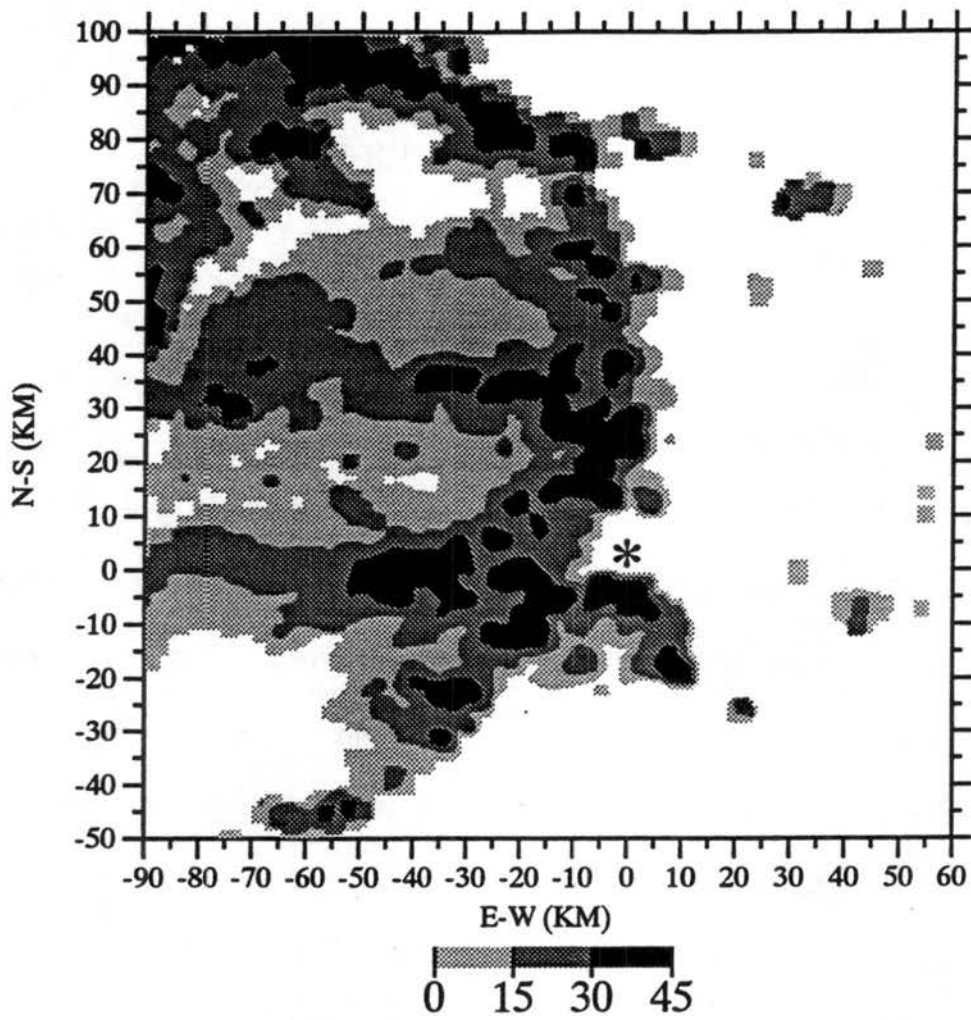


Figure 2.8 Radar image depicting an example of a MCS scale linear event from 10 Feb. 1993. The values shown are reflectivity in dBZ. The plot origin is the nominal position of the R/V Vickers.

CHAPTER 3

PROCEDURES

3.1 Introduction

The overarching goal of the current study is to determine how the four different types of atmospheric convective systems observed during TOGA COARE affect the surface fluxes of heat, moisture, and momentum. Radar reflectivity data from the MIT radar on board the R/V Vickers were used in conjunction with surface meteorological data from the Woods Hole Oceanographic Institute (WHOI) Improved Meteorology (IMET) buoy to produce composites of the surface flux response for each class of convective organization observed during TOGA COARE. The radar reflectivities were mainly used for convective system identification and rainfall estimation in the vicinity of the IMET buoy. The surface meteorological data from the IMET buoy were used to calculate the surface fluxes of heat, moisture, and momentum. Time series of the surface fluxes, which were calculated with an updated version of the COARE Bulk Flux Algorithm (Fairall et al., 1996b), were retrieved as the different types of convective systems passed over the IMET buoy, thereby providing an Eulerian view of the surface response. Composites of the individual time series were then developed for each of the four different types of atmospheric convective systems.

The data collected by the MIT radar and the IMET buoy will be discussed in Sec. 3.2 and the classification of atmospheric convection based on its spatial scale and horizontal morphology will be discussed in Sec. 3.3. A discussion on the radar derived rain rates and the calculation of the surface fluxes will be included in Secs. 3.4 and 3.5 respectively. Lastly, a detailed description of the compositing scheme used in this study will be developed in Sec. 3.6.

3.2 Data

During TOGA COARE an unprecedented amount of data was collected from a number of different platforms in the tropical W. Pacific. For the current study, data from the MIT Doppler radar on board the R/V Vickers (operated by the University of Southern California) and the WHOI IMET buoy located near the center of the IFA was used to monitor atmospheric convection and calculate the surface fluxes of heat, moisture, and momentum.

The MIT Doppler radar is a WSR-74 C-band, magnetron system. This radar underwent a number of upgrades prior to its deployment on board the R/V Vickers for TOGA COARE. The technical specifications of the MIT radar as configured for COARE are shown in Table 3.1. The majority of the upgrades were done to insure that the radar would maintain a high level of reliability during operations in rough sea conditions (see Rutledge et al., 1993 for a complete listing.). A new signal processor was installed which was capable of providing 125 m gate spacing for up to 2048 gates. A new low noise amplifier and mixer were also installed which resulted in the lowering of the minimum detectable signal from -108 dbm to approximately -115 dbm. This

improvement in the sensitivity of the radar was important because it allowed certain non-precipitating targets to be detected.

Since the radar was being operated on board a ship, the stabilization of the radar was obviously vital to the collection of meaningful data. An inertial navigation unit was mounted on the radar's pedestal and monitored roll, pitch, and heading along with the time derivatives of these quantities. This information was instantaneously relayed to the radar control interface which controlled the antenna such that it appeared to be fixed to a horizontal plane on the earth's surface. In this way the motion of the ship did not affect the stored radar images.

The R/V Vickers was at sea for three 30 day time periods separated by 10 days when the ship was in port at Honiara, Solomon Islands. While at sea the nominal position of the R/V Vickers was at $2^{\circ} 05' S$, $156^{\circ} 15' E$ (Fig. 3.1) during which the MIT radar operated continuously (except for small amounts of down time for routine maintenance). The ship repositioned approximately once every 12 hours to compensate for current drift. The general operations consisted of switching between a low pulse repetition frequency (PRF) mode with a range of 300 km and a high PRF mode with a range of 145 km. The low PRF mode, which had a gate spacing of 500 m, consisted of only low level scans and was used mainly for surveillance because of its larger range. In the high PRF mode, full volume scans were generally collected with gate spacing of either 250 m or 375 m. Range height indicator (RHI) cross-sections were also collected as deemed beneficial by the on board scientists. As a general rule, a cycle consisting of one surveillance scan (low PRF mode), one full volume scan (high PRF mode), and any

RHI scans were completed every 10 minutes. For the current study the full volume scans are used with surveillance scans being used only if the full volume scan was missed in the 10 minute cycle.

During the field program, the radar data was saved in Interactive Radar Information System (IRIS) format. During post processing the IRIS data files were converted to Universal Format (UF) in order to use the NCAR REORDER software to interpolate the data to a cartesian grid. The horizontal and vertical grid spacing was set at 0.75 km and 0.5 km respectively. A Cressman weighting function was used to determine the reflectivity value at each grid point with a radius of influence of 1.75 km in the horizontal and 1.5 km in the vertical. These gridded reflectivity fields were used for convective system identification and to calculate rain rates.

Surface meteorological data from the WHOI IMET buoy, which was deployed near 1° 45' S, 156° 00' E, was used with an updated version of the COARE Bulk Flux Algorithm (discussed in Sec. 3.5) to calculate the surface fluxes of heat, moisture, and momentum. The IMET buoy was deployed on 21 October 1992 and was recovered on 4 March 1993. It provided a continuous time series of surface meteorological data between those dates, except for a four day period between 9 - 13 December 1992 during which time the buoy was recovered and new instruments were installed (Weller and Anderson, 1996). The position of the IMET buoy relative to the nominal position of the R/V Vickers and a line drawing of the buoy are shown in Fig. 3.1 and Fig. 3.2 respectively.

Hosom et al. (1995) provided a description of the IMET buoy system and Weller and Anderson (1996) gave a detailed description of the instrumentation and accuracy for the deployment during TOGA COARE. Tables 3.2 and 3.3 provide a summary of the instruments mounted on the IMET buoy and the estimated accuracy of the meteorological observations respectively. The sensor heights in Table 3.2 are measured from the sea surface (i.e positive and negative values denote the distance above and below the sea surface respectively). The accuracy values given in Table 3.3 were based on a number of side by side intercomparisons with ship instruments during COARE.

A number of important additions were included on the IMET buoy system to enhance its performance in the large solar heating and generally weak wind environment of the TOGA COARE region (Weller and Anderson, 1996). First of all, the air temperature and relative humidity sensors were mounted inside multiplate radiation shields in order to minimize the effects of daytime solar heating. The general operation of the IMET buoy system required that the wind align the buoy insuring that all the instruments have good exposure. However, it was anticipated that the weak winds which are often observed in the TOGA COARE region would not be strong enough to align the buoy, so three sets of instruments were mounted on three arms thereby insuring that at least one set would have good exposure at any time.

During the post-deployment data processing, a number of corrections (based on intercomparisons with ship instruments) were implemented (Weller and Anderson, 1996). A daytime solar heating signal was removed from the air temperature and incoming longwave radiation observations along with a bias in the incoming shortwave

radiation values. In addition to these corrections, the wind speed and direction relative to the ocean surface was estimated by differencing the measured vector wind from the shallowest current meter (at a depth of 5 m) velocity.

For the current study, meteorological data from the IMET buoy which was recorded every 7.5 minutes was used. During that time interval, the wind velocity was vector averaged and the incoming shortwave and longwave radiation values were averaged. The air temperature, 0.45 m ocean temperature, relative humidity, and barometric pressure were all sampled once during that time interval for 2.5 seconds (Weller and Anderson, 1996).

3.3 Classification of Atmospheric Convection

The classification of convective organization is based on the work of Rickenbach and Rutledge (1996) which was discussed in Sec. 2.3. This classification scheme distinguishes the systems by both spatial scale (MCS vs. sub-MCS scale) and horizontal morphology (linear vs. randomly organized). The classification scheme was based on low level reflectivity patterns and the following four modes of convective organization were identified:

1. Sub-MCS scale non-linear: Events with spatial scale less than 100 km which exhibit no line-like features.
2. Sub-MCS scale linear: Linear events with spatial scale between 50 km and 100 km.
3. MCS scale linear: Linear events with spatial scale greater than 100 km.

4. MCS scale non-linear: Events with spatial scale greater than 100 km which exhibit no line-like features.

The classification scheme is depicted schematically in Figure 3.3.

The classification scheme employed in the current study does have some subtle differences when compared to the scheme used by Rickenbach and Rutledge. First of all, reflectivity images at a height of 1 km rather than 2 km are used to identify the convective mode. This change had no effect on the classification of convection. The classification scheme used by Rickenbach and Rutledge classified an event by the organization mode of the largest spatial scale that was present (i.e. if a sub-MCS scale non-linear system and a MCS scale linear event were both present, it was classified as a MCS scale linear event). The classification scheme used in the current study is based on the individual event of interest (i.e. if a sub-MCS scale non-linear event passed over the IMET buoy during a period when a MCS scale linear event was also present, the event was classified as a sub-MCS scale event since it was the event of interest). This alteration comes into play in a very limited number of cases and was adopted because the current study is concerned with determining the surface flux response of the different *individual* types of convective organization.

3.4 Calculation of Rain Rates

The rain rates used in the current study were deduced from the MIT radar reflectivity observations. The use of radar derived rain rates has an advantage over in situ point measurements in that it provides a better picture of the precipitation characteristics in the vicinity of the point where the surface meteorological data was

collected. To illustrate this point consider the following scenario. A strong convective cell with large rain rates may be within a few hundred meters of the ship or buoy where the surface meteorological data is being collected. The surface fluxes may be greatly enhanced in response to the outflow from the nearby intense cell, but the rain rates observed at the ship or buoy may be quite small. The use of radar derived rain rates allows for the consideration of the precipitation characteristics in the vicinity of the surface meteorological observations.

Figure 3.4 depicts the procedure used to derive the rain rates used in the current study. First of all, 2.4 dBZ was added to the reflectivity value at each grid point to account for an improved estimate of the antenna gain correction and for a missing bandwidth term in the radar equation. The reflectivity field was then partitioned into convective and non-convective components and the first guess rain rate was calculated with the respective Z-R relations. The rain rate field was then corrected for attenuation and converted back to reflectivity by inverting the same Z-R relations. The reflectivity field, now corrected for attenuation, was then repartitioned into convective and non-convective components. Lastly, the final rain rate was obtained by applying the respective Z-R relations to the newly partitioned reflectivity field. A discussion on the methods used to partition the reflectivity field, the Z-R relations employed, and the correction for attenuation is included in the following paragraphs.

The general approach used to partition the reflectivity field into the convective and non-convective components was based on the methodology of Steiner and Houze (1993) and Steiner et al. (1995). These methods assume that all of the grid points with

valid reflectivity values are non-convective unless one of two criteria are met. First of all, all points with a reflectivity greater than or equal to 40 dBZ are classified as convective. A point could also be classified as convective if its reflectivity value was at least 4.5 dBZ greater than a background reflectivity which was defined as the average reflectivity in a 22 km circle (background area) centered around the point being considered. If the point being considered met one of these criteria, that point and all points within a convective area surrounding the point are classified as convective. The convective area was defined as a circle centered on the grid point being considered whose radius was a function of the mean reflectivity within the background area. The sizes of the background and convective areas defined by Steiner et al. (1995) were based on a horizontal grid resolution of 2 km. The choice of grid spacing in the current study (0.75 km) did not allow the following of the defined sizes of the background and convective areas. Therefore, the background area was adjusted to be a circle with a diameter of 22.5 km and the size of the convective area (a function of the mean background reflectivity) is shown schematically in Fig. 3.5. Figure 3.6 summarizes the convective/non-convective partitioning algorithm used in the current study.

The Z-R relations used in the current study were deduced by Tokay and Short (1996) from surface disdrometer observations on Kapingamarangi Atoll during COARE. They observed two distinct drop size distributions which they attributed to convective and non-convective (stratiform) rainfall. The respective Z-R relations that Tokay and Short deduced for convective and non-convective rainfall were given by:

$$Z = 139R^{1.43} \text{ (convective)} \tag{3.1}$$

$$Z = 367R^{1.30} \text{ (non-convective)}$$

where Z is the equivalent reflectivity in $\text{mm}^6 \text{m}^{-3}$ and R is the rain rate in mm hr^{-1} . Note that for a given reflectivity, the rainfall production of non-convective precipitation is about two times smaller compared to convective rain, thereby pointing out the importance of distinguishing between the two regions when estimating rainfall with radar reflectivity data.

As stated in Sec. 3.2 the MIT radar is a C-band radar and hence can experience significant attenuation due to precipitation along the raypath (Geotis, 1975; Hildebrand, 1978). Therefore, the reflectivity field was corrected for attenuation using the methods described by Patterson et al. (1979). This method was designed to be performed on a gridded rain rate field in dBR (i.e. $10\log(\text{rain rate})$). The following relation was used:

$$dBR_c = dBR_{uc} + (1.6 \times 10^{-3}) \sum_{i=1}^{N_r} \left\{ 10^{1.2(dBR_i)_c / 10} \right\} \Delta r \tag{3.2}$$

where dBR_c and dBR_{uc} are the corrected and uncorrected dBR of the value being considered respectively, N_r is the number of path segments of length Δr between the radar origin and value being corrected and $(dBR_i)_c$ is the corrected dBR for the i^{th} segment from the radar origin. This correction was performed spirally outward from the radar origin by linearly interpolating the intervening dBR values from the two closest grid points along the path being considered. Figure 3.7 depicts this procedure schematically. Point d is the point being corrected and points a , b , and c are dBR values linearly interpolated from the previously corrected points a_1 and a_2 , b_1 and b_2 , and c_1 and

c_2 respectively. Once the entire dBR field was corrected, it was converted back to rain rates which were then converted back to reflectivity by inverting Eqn. 3.1.

3.5 Calculation of Surface Fluxes

The calculation of the surface fluxes is an important part of this study. An updated version (version 2.5a) of the COARE Bulk Flux Algorithm (hereafter CBFA) described by Fairall et al. (1996b) is used in this study. This algorithm is based on the Liu-Katsaros-Businger method (Liu et al., 1979) which makes use of Monin-Obukhov Similarity (MOS) theory. However, a number of modifications to the original Liu-Katsaros-Businger code have been made. A listing of these modifications is given below:

1. The roughness/stress relationship has been modified.
2. A gustiness velocity has been included to account for the additional flux induced by boundary layer scale variability.
3. Profile functions now obey the convective limit.
4. A cool-skin/warm-layer model has been added to provide an improved estimate of the SST.
5. The Webb correction to the heat flux is now computed (not used in this study).
6. Constants have been tuned so that the computed fluxes match the flux measurements made on the R/V Moana Wave during TOGA COARE.

Fairall et al. (1996b) report that these modifications typically changed the Liu-Katsaros-Businger model by about 20%. A brief review of the general theory behind the CBFA

along with a discussion on the above modifications will be included in the following paragraphs.

The turbulent fluxes of sensible heat (Q_{SH}), latent heat (Q_{LH}), and momentum (τ) can be written as:

$$\begin{aligned} Q_{SH} &= -\rho_a c_{pa} u_* T. \\ Q_{LH} &= -\rho_a L_e u_* q. \\ \tau &= \rho_a u_*^2 \end{aligned} \quad (3.3)$$

where ρ_a is the density of air, c_{pa} is the specific heat of air, L_e is the latent heat of evaporation, and T_* , q_* , and u_* are the MOS scaling parameters. These scaling parameters are given by:

$$\begin{aligned} T_* &= -c_T^{1/2} (T_s - \theta) \\ q_* &= -c_q^{1/2} (q_s - q) \\ u_*^2 &= c_d S u \end{aligned} \quad (3.4)$$

where T_s is the interfacial SST, θ is the overlying air potential temperature, q_s is the saturation mixing ratio at T_s , q is the overlying air mixing ratio, S is the average value of the wind speed relative to the surface, u is the magnitude of the mean wind vector relative to the surface, and c_T , c_q , and c_d are transfer coefficients for heat, moisture, and momentum respectively. Note that the u_* defined in Eqn. 3.4 was used only to calculate the wind stress and u_{*c} , which was given by (Sykes et al., 1993):

$$u_{*c}^2 = c_d S^2 \quad (3.5)$$

was used to calculate the latent and sensible heat fluxes. The reason that this was done can be illustrated by the following scenario. Consider a time period during which the wind blows from the east at $X \text{ m s}^{-1}$ for half of the time and then from the west at $X \text{ m s}^{-1}$ for the other half of the time. The magnitude of the mean wind vector (u) is zero and the net wind stress acting on the surface is therefore also zero. However, the average wind speed (S) is $X \text{ m s}^{-1}$ and the latent and sensible heat fluxes are greater than zero. It should also be noted that u_* will also be used to compute the Obukov length (L), the roughness Reynolds numbers, and the roughness lengths.

The average wind speed (S) in Eqn. 3.4 and Eqn. 3.5 has been defined as follows (Schumann, 1988):

$$S^2 = u^2 + w_g^2 \quad (3.6)$$

where w_g is a gustiness velocity which accounts for convective effects in the surface layer. The gustiness velocity is related to the convective scaling velocity (W_c) as follows:

$$w_g = \beta W_c \quad (3.7)$$

where β is an empirical constant ($= 1.2$). The convective scaling velocity is computed as follows:

$$W_c^3 = \frac{g}{T} \left[\frac{Q_{SH}}{\rho_a c_{pa}} + 0.61T \frac{Q_{LH}}{\rho_a L_e} \right] z_i \quad (3.8)$$

where z_i is the depth of the atmospheric boundary layer (600 m). If the buoyancy flux is greater than zero, an instability is signified and convection occurs. If it is less than or equal to zero, stable conditions are indicated and w_g is effectively zero.

The transfer coefficients in Eqn. 3.4, which are functions of the atmospheric stability, are given by:

$$\begin{aligned}
 c_r^{0.5} &= c_{Tn}^{0.5} / \left[1 - \frac{c_{Tn}^{0.5}}{a\kappa} \psi_h(\xi) \right] \\
 c_q^{0.5} &= c_{qn}^{0.5} / \left[1 - \frac{c_{qn}^{0.5}}{a\kappa} \psi_h(\xi) \right] \\
 c_d^{0.5} &= c_{dn}^{0.5} / \left[1 - \frac{c_{dn}^{0.5}}{a\kappa} \psi_u(\xi) \right]
 \end{aligned} \tag{3.9}$$

where κ is the von Kármán constant ($= 0.4$), ψ_h and ψ_u are scalar profile functions, c_{Tn} , c_{qn} , and c_{dn} are the neutral transfer coefficients for heat, moisture, and momentum respectively. ξ is defined as z_r/L where z_r is the reference height and L (the Obukov length) is given by:

$$L^{-1} = \frac{g\kappa}{T} (T_s + 0.61T_s q_s) / u_*^2 \tag{3.10}$$

The neutral transfer coefficients, which are a function of the sea surface conditions, are defined as follows:

$$\begin{aligned}
 c_{Tn}^{0.5} &= \frac{a\kappa}{\log(z_r / z_{oT})} \\
 c_{qn}^{0.5} &= \frac{a\kappa}{\log(z_r / z_{oq})} \\
 c_{dn}^{0.5} &= \frac{\kappa}{\log(z_r / z_o)}
 \end{aligned} \tag{3.11}$$

where a accounts for the difference in scalar and velocity von Kármán constants, and z_{oT} , z_{oq} , and z_o are the roughness lengths for temperature, humidity, and velocity respectively.

The roughness lengths are defined as the height at which the extrapolation of the respective profile intersects the surface value. In the CBFA, the roughness length for velocity is defined as the combination of the formulas of Liu et al. (1979) and Charnock (1955) which are for smooth and rough flow respectively:

$$z_0 = \alpha \frac{u^2}{g} + 0.11 \frac{\nu}{u} \quad (3.12)$$

where α is the Charnock constant and ν is the kinematic viscosity of air. The roughness length for velocity is related to the roughness Reynolds number (R_r) in the following manner:

$$R_r = \frac{u z_0}{\nu} \quad (3.13)$$

Similar expressions relating the roughness Reynolds number for temperature and humidity to their roughness length counterparts can be written as follows:

$$R_r = \frac{u z_{0T}}{\nu} \quad (3.14)$$

$$R_q = \frac{u z_{0q}}{\nu}$$

Liu et al. (1979) deduced relationships between the roughness Reynolds number and the roughness lengths for temperature and humidity. These relationships are given in Table 3.4.

Atmospheric stability influences enter into the surface flux formulations through the scalar profile functions in Eqn. 3.9. In these relations it is assumed that the profile

functions are the same for temperature and humidity (ψ_h). In stable conditions (i.e. $\xi > 0$) the profile functions are given by (Garratt, 1992):

$$\psi_h = \psi_u = -4.7\xi \quad (3.15)$$

whereas during unstable conditions (i.e. $\xi < 0$) they are given by (Fairall et al., 1996b):

$$\psi_h = \frac{1}{1+\xi^2}\psi_{hK} + \frac{\xi^2}{1+\xi^2}\psi_c \quad (3.16)$$

$$\psi_u = \frac{1}{1+\xi^2}\psi_{uK} + \frac{\xi^2}{1+\xi^2}\psi_c$$

The profile functions in Eqn. 3.16 are blended forms of the standard Kansas-type profile functions (Garratt, 1992)

$$\psi_{hK} = 2 \ln \left[\frac{1+x^2}{2} \right] \quad (3.17)$$

$$\psi_{uK} = 2 \ln \left[\frac{x+1}{2} \right] + \ln \left[\frac{x^2+1}{2} \right] - 2 \tan^{-1}(x) + \frac{\pi}{2}$$

where

$$x = (1-16\xi)^{1/4}$$

and profile functions which obey the $\xi^{-1/3}$ asymptotic convective limit dependence on stability

$$\psi_c = 15 \ln \left[\frac{y^2+y+1}{3} \right] - \sqrt{3} \tan^{-1} \left[\frac{2y+1}{\sqrt{3}} \right] + \frac{\pi}{\sqrt{3}} \quad (3.18)$$

where

$$y = \sqrt[3]{1-\xi\gamma}$$

and γ is an empirical constant (= 12.87).

Fairall et al. (1996b) have deduced that in order to estimate the heat balance to within 10 W m^{-2} , the SST needs to be known to an accuracy of $\pm 0.2 \text{ K}$. The above described model requires the interfacial SST as one of the inputs in Eqn. 3.4. Since the majority of the observational platforms measured the bulk (i.e. below surface) SST, a cool skin and warm layer model has been added to adjust the bulk SST measurement to the interfacial value. Fairall et al. (1996a) provide a complete description of these models and only a brief overview will be given here.

A cool skin is observed at the ocean interface because the latent, sensible, and longwave radiative fluxes are felt within the upper fractions of a millimeter of the surface (Saunders, 1967). The interface temperature is typically about 0.2 K to 0.5 K cooler than the water just a millimeter below the surface. The cool skin model employed by the CBFA is based on the work of Saunders (1967). Fairall et al. (1996a), using data collected on the R/V Moana Wave during COARE, found that the inclusion of the cool skin decreases the heat flux out of the ocean by about 11 W m^{-2} with the largest effect occurring at night.

A near surface warm layer (generally on the order of a few meters) is known to develop during periods of light winds and strong solar heating (Bruce and Firing, 1974; Price et al., 1986; Lukas, 1991). The warm skin model employed by the CBFA is based on the mixed layer model of Price et al. (1986). Fairall et al. (1996a) found that inclusion of the warm layer leads to an average increase in the heat flux out of the ocean of about 4 W m^{-2} , but enhancements as large as 50 W m^{-2} were observed near midday.

Surface meteorological data from the IMET buoy was used as inputs for the CBFA. Figure 3.8 shows a flow chart depicting the implementation of the algorithm. Note that the CBFA is also able to calculate the sensible heat flux associated with rainfall but this option was not explicitly used since we did not have a complete time series of rain rates and the rain rates that we calculated had a different time resolution than the surface meteorological data. The sensible heat flux associated with rainfall (Q_{RF}) was calculated separately following the method described in Gosnell et al. (1995):

$$Q_{RF} = R\Delta T c_w \rho_w \varepsilon (1+B)^{-1} 2.78E-7 \quad (3.19)$$

where R is the rain rate in mm hr^{-1} , ΔT is the air/sea temperature difference, c_w is the specific heat of water ($= 4186 \text{ J kg}^{-1} \text{ K}^{-1}$), ρ_w is the density of water ($= 1022 \text{ kg m}^{-3}$), ε is a wet-bulb factor, and B is the bulk Bowen ratio. B and ε are given by:

$$B = \frac{c_p \Delta T}{L \Delta q} \quad (3.20)$$

and

$$\varepsilon = \left(1 + \frac{L d_v}{d_h c_p} \frac{dq_s}{dT} \right)^{-1} \quad (3.21)$$

where Δq is the difference between the ambient specific humidity and the saturation specific humidity at the SST, d_v and d_h are the diffusivities of water vapor and heat respectively, and dq_s/dT accounts for the change in saturation specific humidity with temperature. In the COARE region, B and ε have values typically around 0.1 and 0.2 respectively (Gosnell et al., 1995). Substitution of these values along with the known constants lead to the following expression for Q_{RF} :

$$Q_{RF} = 2.6 R \Delta T \quad (3.22)$$

The current study uses this relation to calculate the heat flux associated with rainfall. The rain rate that was used is the radar derived average rain rate in a 4.5 km by 4.5 km box centered on the nominal position of the IMET buoy. A box of this size was chosen to account for uncertainties in the position of both the R/V Vickers and the IMET buoy. The uncertainties in the location of the R/V Vickers were on the order of one km (Walt Petersen, personal communication) and the IMET buoy had a watch radius of 1.276 km (Mark Baumgartner, personal communication). Therefore, the actual location of the IMET buoy would have been somewhere within this 4.5 km by 4.5 km box.

The rain rate calculations described in Sec. 3.4, along with the above described surface flux calculations were used to construct 32 time series of rain rates, surface fluxes, and the related surface meteorological variables for the four different types of convective organization described in Sec. 3.3. The time series for each type of convective organization were then used to create composite analyses describing the surface flux response and boundary layer recovery which resulted from the different types of convective organization.

3.6 Compositing Scheme

Convective systems are known to drastically affect the surface layer. The outflows created by active convection have been associated with significant decreases in air temperature and increases in wind speeds (Addis et al., 1984). In the wake of the convective event, the air temperature generally increases, approaching its undisturbed environmental value. The current study attempts to separate the convectively active period from the recovery period in the compositing process. In this way, distinct

processes occurring in the two periods will not be mixed in the final composites, thereby leading to a more accurate representation of the response to the convective system.

The compositing scheme employed consists of four sections which represent the pre-convective (one bin), convectively active (three bins), recovery (five bins), and post-recovery (one bin) time periods. This approach leads to composite time series with 10 total bins. The start of the convectively active bin was indicated when the air temperature started to decrease in response to convective activity (a temperature drop of at least 1° C was required). The end of the convectively active and start of the recovery period was indicated once the minimum air temperature and maximum wind speed were both observed. This indicated that convective scale downdrafts were no longer directly affecting the area and the recovery had begun. Because three bins were used in the convectively active period and rain rates were sampled every 10 minutes, the convectively active period was required to last at least 30 minutes. The end of the recovery period was indicated when the two hour running mean air temperature started to decrease and continued to decrease for eight consecutive 7.5 minute time periods (i.e. one hour). This warming reversal criteria, which was similar to the approach employed by Young et al. (1995), indicated that other processes are playing significant roles in determining the boundary layer air temperature. The convectively active and recovery time periods were then separated into three and five equally spaced bins respectively. Pre-convective and post-recovery bins were included prior to the convectively active period and after the recovery period respectively. These bins were defined to be one hour in length for each class of convective organization. The pre-convective bin

describes the pre-convective conditions and helps illustrate the changes induced by the convective system. The post-recovery bin is useful in checking the accuracy of the recovery termination criteria.

The separation of the time series into the convectively active and recovery time periods was also beneficial in that convective and recovery processes work on different time scales. Within convectively active regions, the environment changes very rapidly whereas in recovery regions, the environment changes much more slowly. The separation of the two regimes allowed for different bin lengths which would better represent the physical processes which were occurring. In the current study, the convective bins were typically around 20 minutes in length whereas the length of the recovery bins ranged from about 30 minutes to two hours.

Table 3.1 Technical Specifications of MIT C-band Doppler Radar (Rutledge et al., 1993).

Operating Frequency	5590 MHz
Minimum Detectable Signal	-115 dbm
Peak Power	155 kw
Pulse Width	1.0 μ s
Antenna Gain	40.5 db
Beamwidth	1.6 degrees (3 db)
Antenna Scan Rates	30 deg s ⁻¹ (Az. and Elev.)
Antenna Accelerations	Greater than 40 deg s ⁻²
Elevation Upper Limit	50 degrees
Elevation Lower Limit	-18 degrees
Pulse Repetition Frequency	Variable or Dual (250-1500 Hz)

Table 3.2 IMET Buoy Instrumentation (Weller and Anderson, 1996).

PARAMETER	INSTRUMENT	SENSOR HEIGHT
Air Temperature	Thermistor with Gill Shield	2.78 m
SST	Thermistor	-0.45 m
Wind Speed and Direction	R. M. Young Cup/Vane	3.54 m
Barometric Pressure	Paroscientific Digiquartz	3.00 m
Relative Humidity	Vaisala Humicap, with Gill Shield	2.74 m
Incoming Shortwave Radiation	Eppley Precision Spectral Pyranometer (PSP)	3.54 m
Incoming Longwave Radiation	Eppley Precision Infrared Radiometer (PIR)	3.54 m

Table 3.3 Estimated accuracy of meteorological observations from the WHOI IMET buoy during TOGA COARE (Weller and Anderson, 1996).

<u>Variable</u>	<u>Instantaneous Accuracy</u>
Wind Speed	5 %
Wind Direction	10°
Barometric Pressure	0.5 mb
Air Temperature	0.2° C
Sea Surface Temperature	0.1° C
Incoming Shortwave Radiation	3 %
Incoming Longwave Radiation	10 W m ⁻²
Specific Humidity	0.2 g kg ⁻¹

Table 3.4 The lower boundary values of the logarithmic profiles $z_{or}u/v = a_1R_r^{b_1}$ and $z_{oq}u/v = a_2R_r^{b_2}$

R_r	a_1	b_1	a_2	b_2
0.0 - 0.11	0.177	0	0.292	0
0.11 - 0.825	1.376	0.929	1.808	0.826
0.825 - 3.0	1.026	-0.599	1.393	-0.528
3.0 - 10.0	1.625	-1.018	1.956	-0.870
10.0 - 30.0	4.661	-1.475	4.994	-1.297
30.0 - 100.	34.904	-2.067	30.790	-1.845
100. - 300.	1667.19	-2.907	1448.68	-2.682
300. - 1000.	5.88E5	-3.935	2.98E5	-3.616

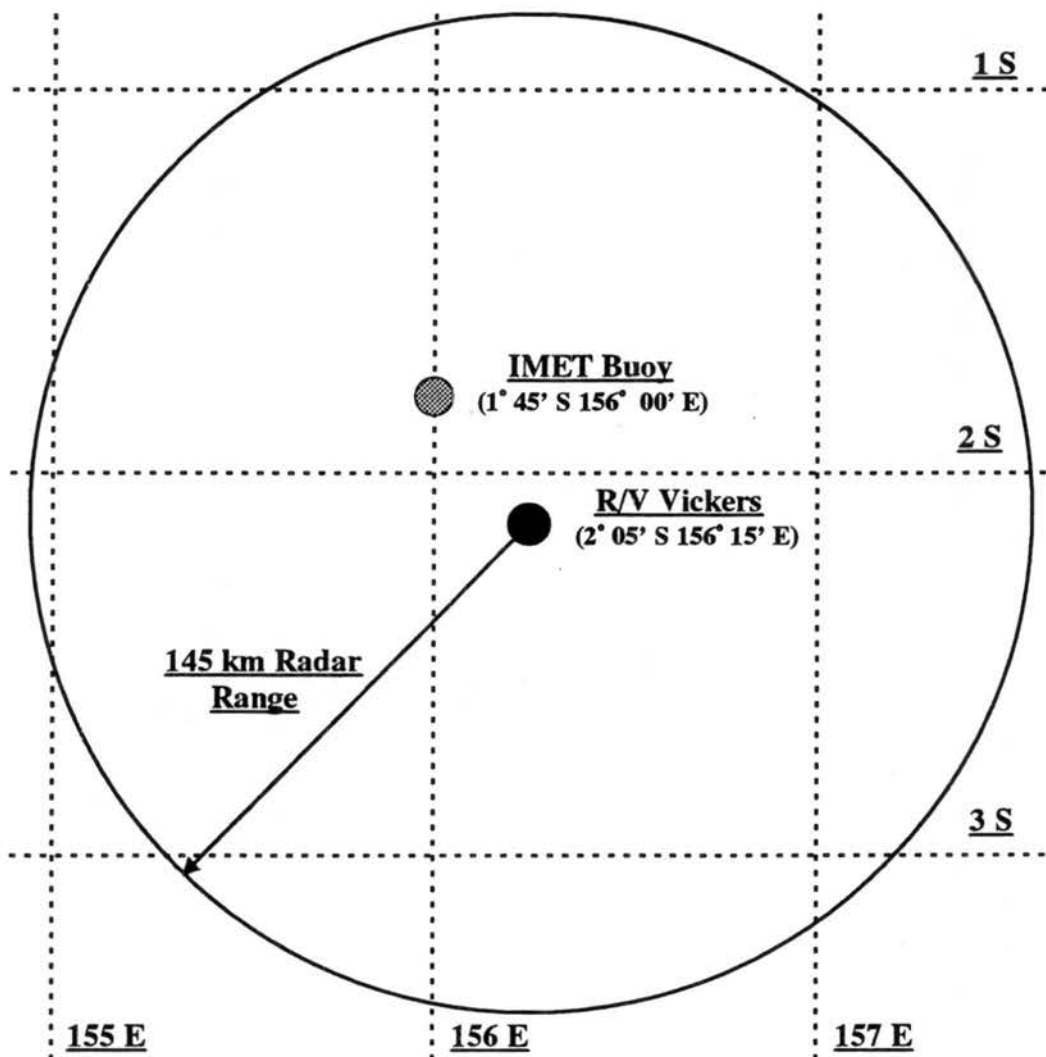


Figure 3.1 Nominal positions of observational platforms with 145 km radar range ring.

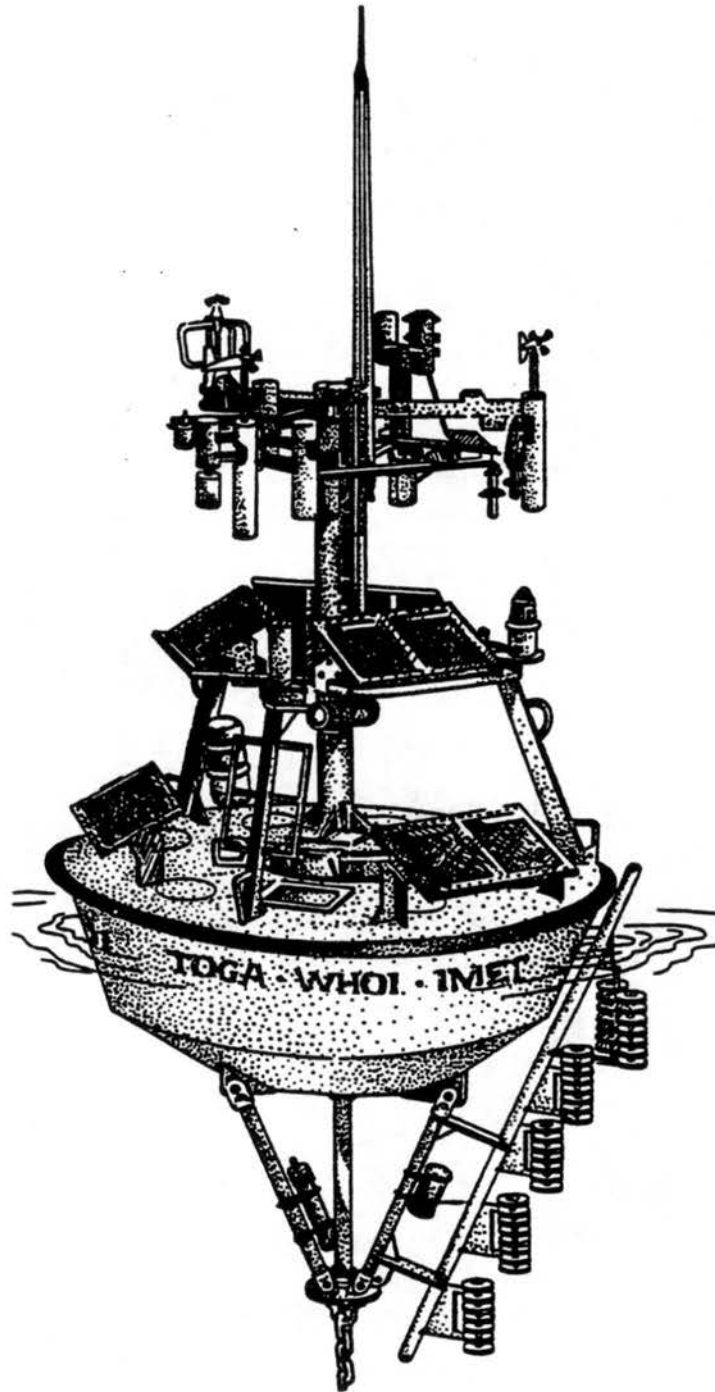


Figure 3.2 Line drawing depicting the WHOI IMET surface buoy deployed in TOGA COARE (Weller and Anderson, 1996).

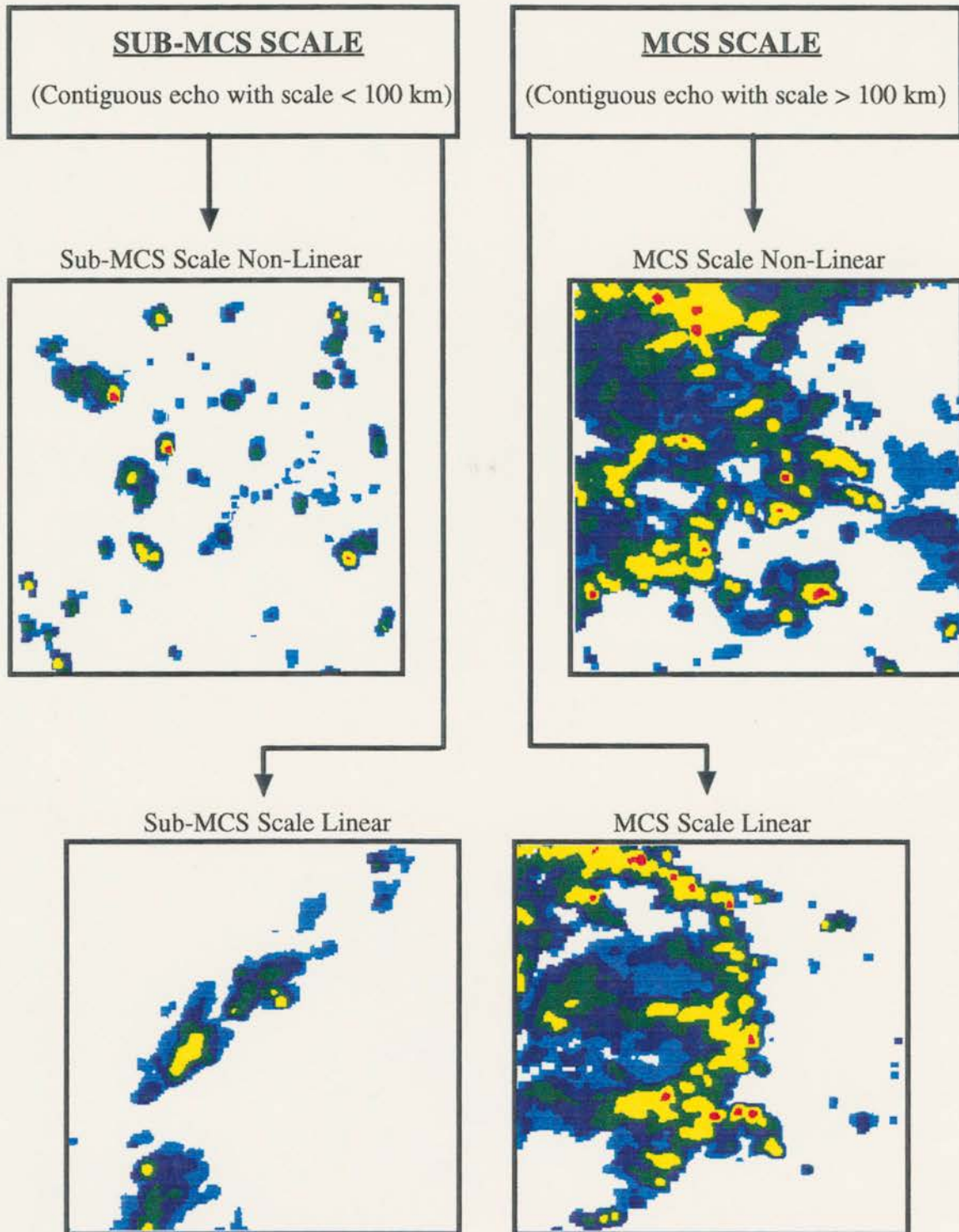


Figure 3.3 Schematic depicting the classification of atmospheric convective systems. Radar images are 150 km x 150 km with the light blue shading being 0 - 10 dBZ, dark blue being 10 - 20 dBZ, green being 20 - 30 dBZ, yellow being 30 - 40 dBZ, and red being 40 - 50 dBZ.

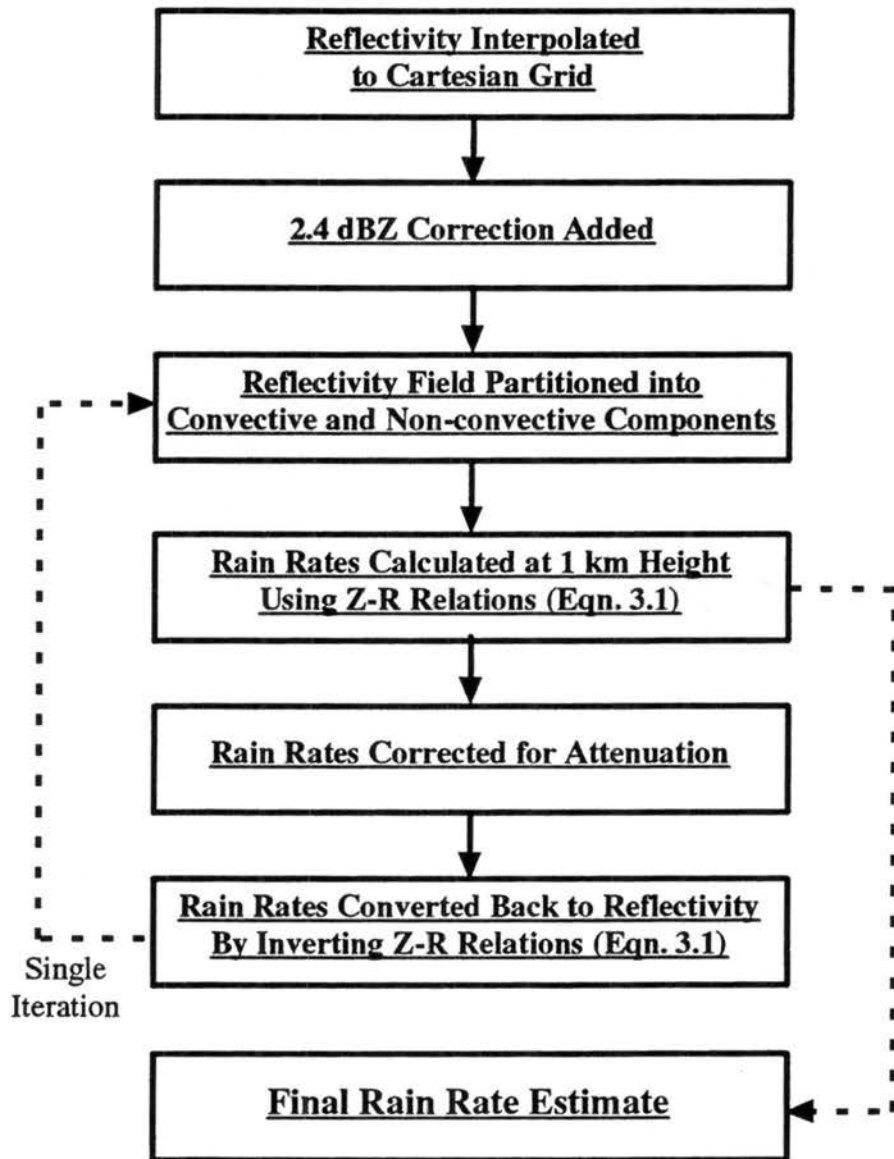


Figure 3.4 Summary of method employed to obtain rain rate estimates. Based on methodology of Rickenbach and Rutledge (1996).

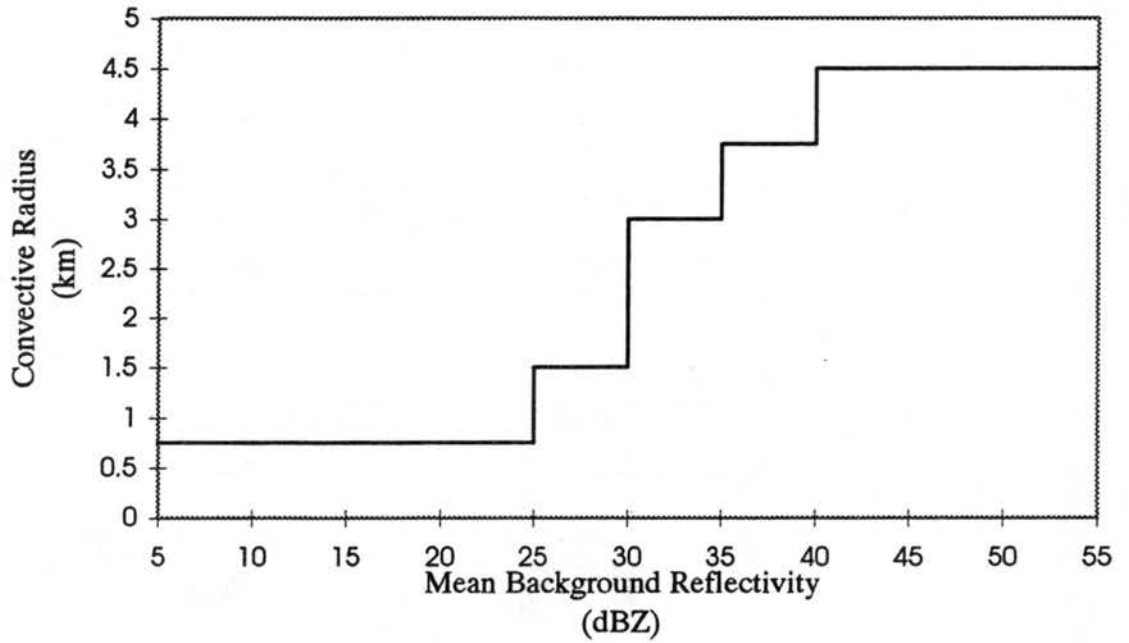


Figure 3.5 Radius of convective circle as a function of the mean reflectivity within the background area. Methods of Steiner et al. (1995) were adjusted to be compatible with the grid size used in the current study.

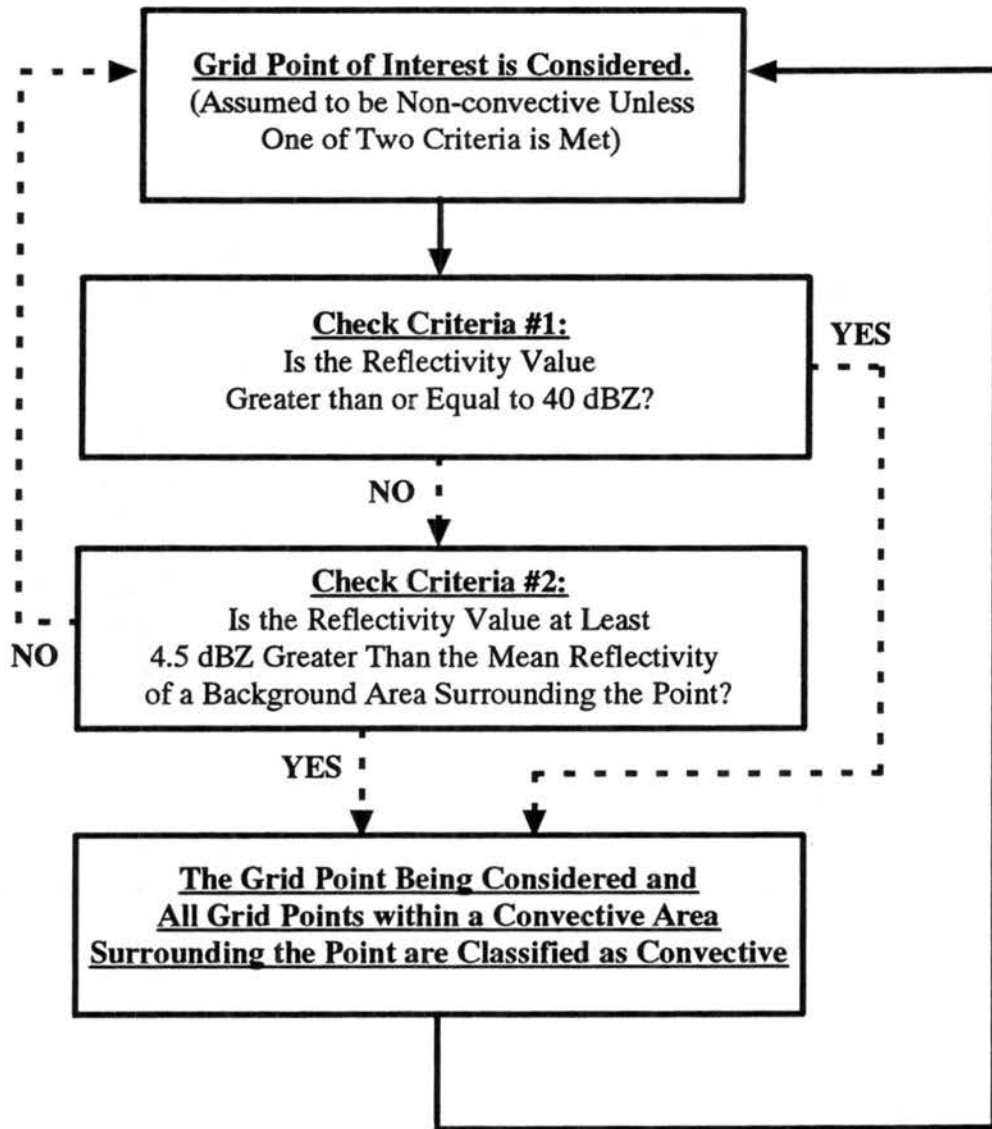


Figure 3.6 Flow chart describing partitioning of reflectivity field into convective and non-convective components. The background area is a circle with a radius of 11.25 km. The convective area is a circle whose radius is a function of the mean reflectivity within the background area (See Fig. 3.5). Based on methodology of Steiner and Houze (1993) and Steiner et al. (1995).

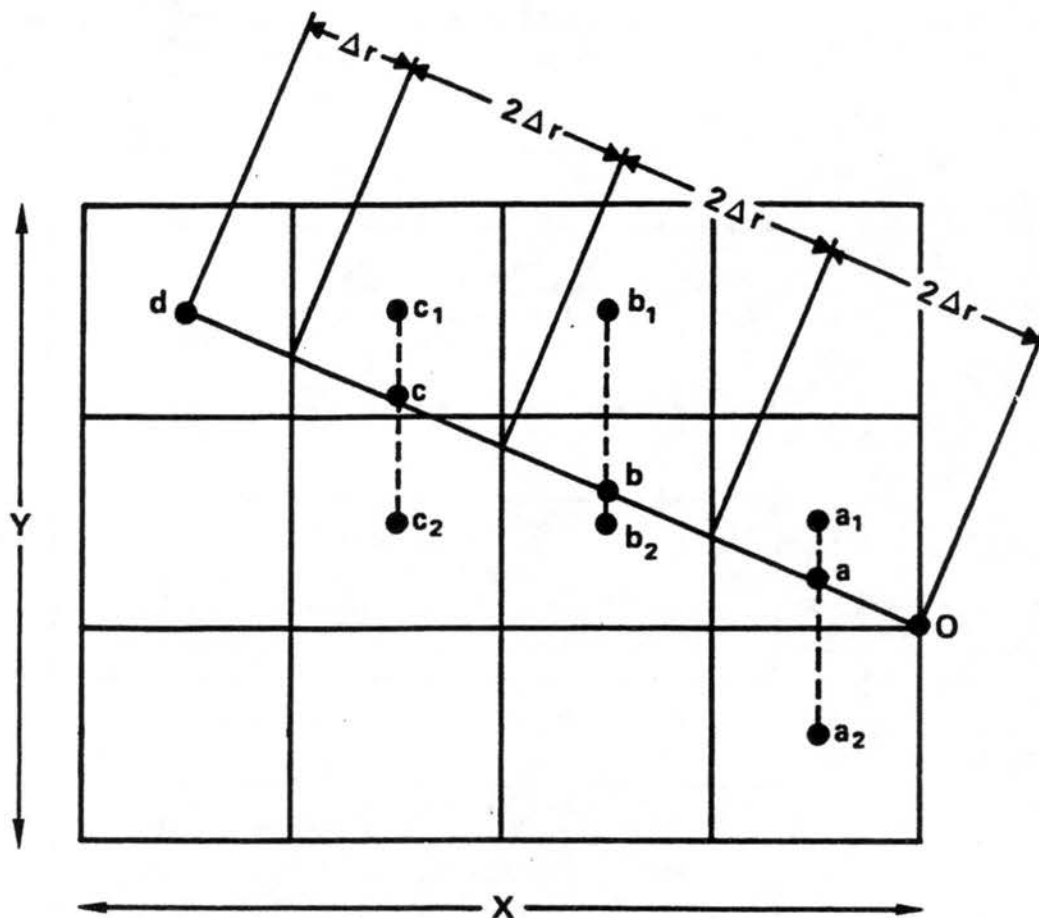


Figure 3.7 Schematic depicting the method employed when interpolating the dBR values along a path from the radar origin (point O) to point d. The intervening dBR values were then used in Eqn. 3.2 to correct the dBR value at point d for attenuation due to precipitation along the path (Patterson et al., 1979).

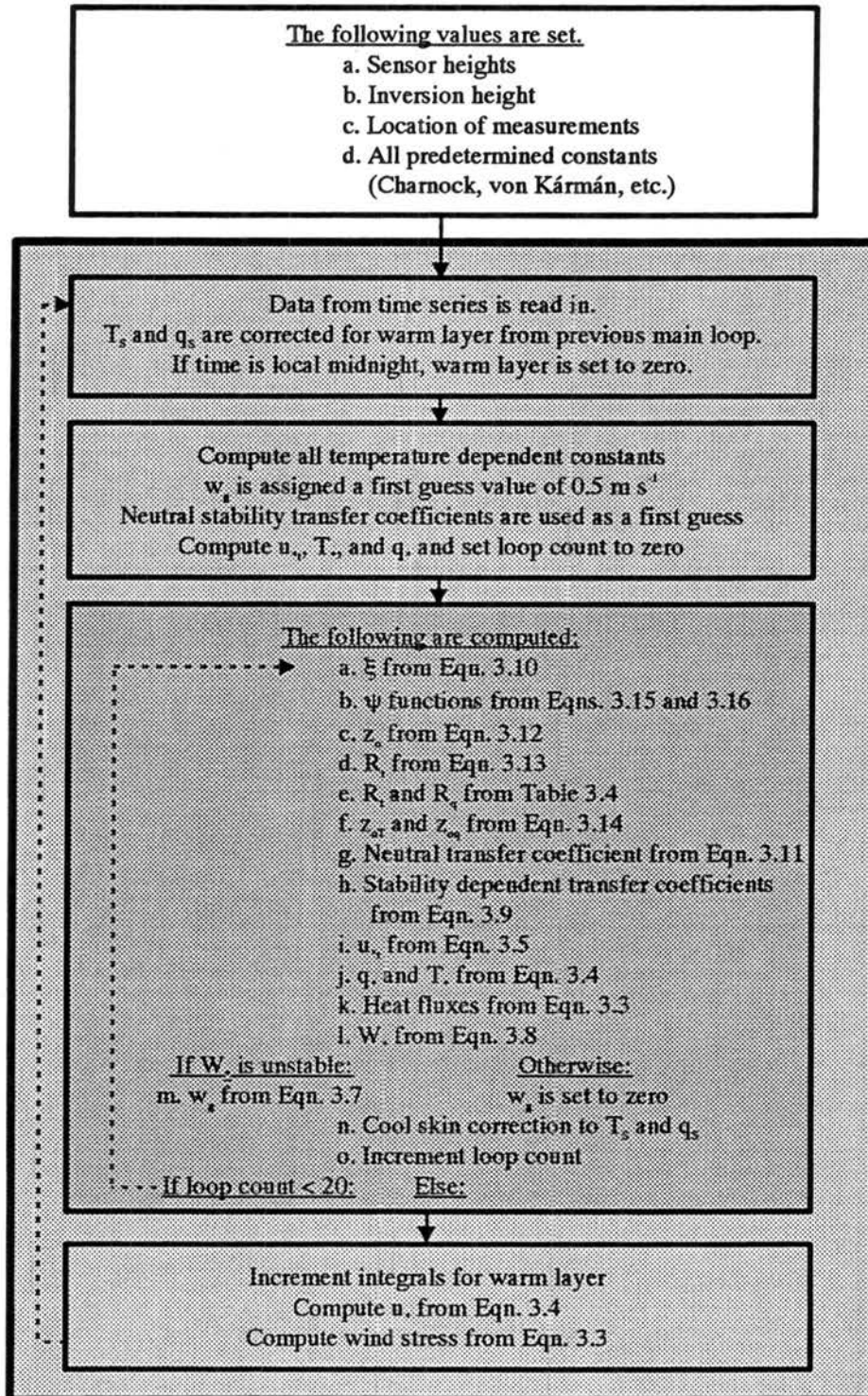


Figure 3.8 Flow chart depicting the implementation of the COARE Bulk Flux Algorithm. Loops are shown with dashed lines with the light shaded region containing the main loop while the darker shading contains the stability iteration loop.

CHAPTER 4

RESULTS

4.1 Introduction

A number of previous studies have explored the effects that atmospheric convective systems have on the boundary layer over the tropical oceans (Gaynor and Ropelewski, 1979; Johnson and Nicholls, 1983; Young et al., 1995; Jabouille et al., 1996). However, these studies either analyzed the response to an individual event, typically squall lines; or they described the average response to convective systems without differentiating between different classes of convective organization. Rickenbach and Rutledge (1996) identified four different types of convective organization with shipboard radar during TOGA COARE which tended to develop in different environmental conditions. The environmental conditions play an important role in determining the degree of organization and the intensity of the developing convective systems. Therefore, one would expect that the different types of convective organization would affect the atmospheric boundary layer differently. The goal of the current study is to systematically determine how these four classes of convective organization affect the boundary layer and alter the surface fluxes of heat, moisture, and momentum.

For the current study, 32 individual time series have been used to produce composite time series of wind stress, along with the surface heat fluxes (latent heat flux,

sensible heat flux, and sensible heat flux associated with rainfall) for each class of convective organization. Composites of the pertinent bulk atmospheric and oceanic variables were also produced to illustrate the conditions responsible for the surface flux enhancements. Of the 32 individual convective events (as identified by radar) that were used to produce the composites; nine were sub-MCS scale non-linear events, eight were sub-MCS scale linear events, six were MCS scale non-linear events, and nine were MCS scale linear events. The surface flux time series (wind stress, sensible heat flux, latent heat flux, and rainfall heat flux) of all 32 individual events are provided in the appendices. Appendix A and B contain the sub-MCS scale non-linear and linear events respectively, while the MCS scale non-linear and linear events are given in Appendix C and D respectively.

Since the different types of convective organization discussed in Chapter 2 have different spatial and temporal scales, the bins representing the convectively active and recovery periods had different lengths in the composites. Figure 4.1 summarizes the average bin lengths for the pre-convective, convectively active, recovery, and post-recovery bins for the four different types of convective organization. The pre-convective and post-recovery bins were defined to be one hour in length for all four types of convective organization. For the sub-MCS scale events the average length of each convectively active bin was 12.5 and 17.2 minutes for the linear and non-linear events respectively, while for the MCS scale events they were significantly longer at 21.9 and 39.2 minutes respectively. The average length of the convectively active bins for the non-linear events were slightly longer than for the linear events because the linear events

typically had significant motion associated with them whereas the non-linear events typically exhibited very little motion. Therefore, the active convection influenced the region for a longer period of time for the non-linear events than for the linear events.

The recovery bins were significantly longer than the convectively active bins for each of the respective types of convective organization. For the sub-MCS scale events, the average recovery bin length was 33.8 and 40.3 minutes for the linear and non-linear events respectively, while for the MCS scale events, the average recovery bin length were nearly twice as long, at 73.8 and 117 minutes respectively. The main reason the recovery time for the MCS scale events was much longer than for the sub-MCS scale events was that the MCS scale events typically induced larger temperature depressions and had significant stratiform precipitation components. The sub-MCS scale events produced smaller temperature depressions and produced almost no stratiform precipitation.

The composite analyses of the rainfall, wind stress, latent heat flux, sensible heat flux, and the heat flux associated with rainfall will be discussed in Secs. 4.2, 4.3, 4.4, 4.5, and 4.6 respectively. In each of these sections the pertinent bulk variables describing the respective surface flux will also be discussed. Finally, an evaluation of how well the composites represent the individual time series used to construct the composites will be discussed in Sec. 4.7, along with a comparison of these results to previous studies.

4.2 Rainfall

Figure 4.2 depicts the composite time series of rain rates for each of the four types of convective organization identified in this study. Maximum rain rates observed within a 4.5 km box surrounding the IMET buoy were used to produce these composites. The maximum rain rate was used to give a better indication of the rainfall intensity in the vicinity of the IMET buoy. For all types of convective organization the peak rain rates were observed during the convectively active period. The MCS scale events produced the largest peak rain rates (over 12 mm hr⁻¹ and 14 mm hr⁻¹ for the non-linear and linear events respectively) while the sub-MCS scale peak rain rates were slightly less (about 11 mm hr⁻¹ and 9 mm hr⁻¹). This implies that the MCS scale convective features were typically more intense than the sub-MCS scale convective features, which is consistent with the study of Rickenbach and Rutledge (1996). For the MCS scale events, the first one or two recovery bins also showed significant rain rates (1 - 2 mm hr⁻¹), since these events typically had significant stratiform components associated with them. The sub-MCS scale non-linear events exhibited a similar behavior, caused primarily by the fact that these events typically had very little motion associated with them and a portion of the precipitating cell was still within the 4.5 km box when the boundary layer recovery began. The separation into convectively active and recovery time periods was based solely on air temperature and wind speed arguments. The fact that the rain rates typically decreased significantly between the two periods supports the rationale employed to separate the two periods.

4.3 Wind Stress

The surface wind stress is thought to be approximately proportional to the square of the wind speed and the drag coefficient (ref. Eqn. 3.3). The drag coefficient is a function of the surface layer stability and the surface roughness (which is related to the wind speed). Therefore, the surface wind stress is extremely sensitive to changes in wind speed, but much less sensitive to the surface layer stability. Outflows from active convection are known to have enhanced wind speeds, which can greatly enhance the wind stress.

Figure 4.3 shows the composite surface wind speed response (relative to the five meter current) to the four different types of convective organization. All four types of convective organization exhibit significant enhancements in the surface wind speed during the convectively active periods, owing to the presence of convective scale downdrafts directly affecting the surface layer. For the sub-MCS scale non-linear events, the peak wind speed during the convectively active period was approximately 4.5 m s^{-1} , an increase of slightly over 2 m s^{-1} from the pre-convective environment. The sub-MCS scale linear events also exhibited an increase of slightly over 2 m s^{-1} from the pre-convective conditions with a peak wind speed of about 5.5 m s^{-1} . The MCS scale events exhibited peak winds (about 8.5 m s^{-1} and 9.5 m s^{-1} for the linear and non-linear events respectively) during the convectively active periods which are almost twice those observed for the sub-MCS scale events. This may be attributed to overall more intense convective features and stronger downdrafts being associated with the MCS scale events. Wind speeds decreased significantly during the recovery phase and were approximately

equal to or slightly greater than the pre-environmental conditions. This implies that the convective scale downdrafts were no longer directly affecting the surface layer during the recovery periods.

Young et al. (1995) hypothesized that the wind speed enhancements due to active convection are independent of the pre-convective environment. The results of the current study do not necessarily discount that hypothesis, but they do indicate that the wind speed enhancements are sensitive to the organizational mode of the active convection causing the enhancement, something which was not considered in the Young et al. study.

Figure 4.4 shows the composite drag coefficient response to the four different types of convective organization. The changes in the drag coefficient were much less than the wind speed changes; however, the changes were much more sensitive to the type of convective organization. During the convectively active period the drag coefficient decreased by about 10% from the pre-convective (environmental) value for the sub-MCS scale non-linear events whereas it increased by roughly 20% for both the linear and non-linear MCS scale events and remained approximately constant for the sub-MCS scale linear events. The reason for this behavior was that for the MCS scale events the enhanced wind speeds in the convectively active periods were large enough to cause the surface to become rough. This causes the drag coefficient to increase since now the pressure force of the wind acting on the surface (i.e. on the waves) becomes significant. Fairall et al. (1996b) report that rough flow occurs for wind speeds greater than about 8 m s^{-1} . For the sub-MCS scale non-linear events, the winds generally did not get strong enough to cause the surface to be characterized as rough and the drag coefficient

decreased. The reason the drag coefficient for the sub-MCS scale linear events showed almost no change was that some of the events used to create the composite contained winds that were strong enough to cause the surface to be characterized as rough whereas other events did not.

The composite surface wind stress response to the four different types of convective organization is shown in Fig. 4.5. The shape of the wind stress composite is very similar to the wind speed composite due to the wind speed squared dependence on the wind stress. The largest enhancements for all types of convective organization occurred during the convectively active period when the convective scale downdrafts were directly affecting the surface layer. The MCS scale events showed the greatest enhancements (increasing from about 0.05 N m^{-2} to slightly over 0.2 N m^{-2}) due to the higher wind speeds that were observed (both a wind speed squared effect and to a lesser extent, a surface roughness effect). The wind stress enhancements for the sub-MCS scale events were much more limited (increasing from about 0.02 N m^{-2} to 0.06 N m^{-2}). During the recovery periods the wind stress decreased virtually to the pre-environmental conditions.

4.4 Sensible Heat Flux

The surface sensible heat flux is controlled largely by the wind speed and the air-sea temperature difference (ref. Eqn. 3.3). Convective scale downdrafts typically bring cold, dry air down from the mid to upper troposphere (Zipser, 1977). Therefore, under the convectively active regions of precipitating systems, the sensible heat flux is greatly enhanced due to the combined effects of increased wind speed and decreased air

temperature. The sensible heat flux also remains enhanced during the boundary layer recovery as a finite amount of time is required for the air temperature to recover to its pre-convective environmental value. Any precipitation during the recovery will lead to a longer period of enhanced sensible heat flux because the surface air temperature will tend to remain depressed due to evaporational cooling below cloud base.

The composite air temperature response to the four different types of convective organization is shown in Fig. 4.6. All types of convective organization produced distinct decreases in the surface air temperature during the convectively active period. The sub-MCS scale events produced temperature decreases of about 1.5°C and 2°C for the linear and non-linear events respectively, while the MCS scale events produced temperature depressions about twice that (slightly more than 3°C). This result, as with the wind speed, may be attributed to more intense convective features and organized, more intense downdrafts associated with the MCS scale events. On both the sub-MCS and MCS scale, the non-linear events exhibited slightly larger temperature decreases than the linear events. This may have been associated with the fact that the non-linear events typically had very little motion associated with them (relative to the linear events) which allowed the boundary layer to be affected by the active convection over a relatively longer period of time compared to the linear events. After the convectively active period, the air temperature increased to nearly the pre-convective environment value. During the recovery period for each type of convective organization, the rate of temperature change was initially about $1^{\circ}\text{C hr}^{-1}$ (see Fig. 4.7) and gradually decreased with time to about $0.5^{\circ}\text{C hr}^{-1}$ near the end of the recovery. This is primarily due to the fact that the air-sea

temperature difference, which primarily controls the sensible heat flux during the recovery, decreases as the boundary layer recovers. The temperature drop shown in the post-recovery period signifies the end of the boundary layer recovery and can typically be attributed to the effects of a new precipitation event affecting the region.

The composite SST (at a depth of 0.45 m) response to the four different types of convective organization is shown in Fig. 4.8. The decreases in the SST are much smaller than the changes in the air temperature for all four types of convective organization and thus have only a limited effect on the sensible heat flux. The SST decreased less than 0.15°C for the sub-MCS scale linear and the MCS scale events. For the sub-MCS scale non-linear events, the pre-convective SST was about 1°C warmer than for the other types of convective organization and the composite SST decrease was slightly more than 0.25°C . It should be noted that some of the individual cases produced a SST drop of greater than 0.5°C . The reason for this is that the sub-MCS scale non-linear events tend to develop during periods of weak winds and very little cloud cover (Rickenbach and Rutledge, 1996). In response to the large incoming solar radiation and limited wind mixing, a near surface diurnal warm layer which is typically on the order of meters deep develops (Bruce and Firing, 1974; Price et al., 1986; Lukas, 1991). During periods when this warm layer is present, the ocean is much more responsive to atmospheric forcing than during periods when the oceanic mixed layer is much deeper. This allows the weak forcing associated with the sub-MCS scale non-linear events to cause much larger SST changes than the stronger forcing associated with the other types of convective organization. The cause of the SST decrease associated with the sub-MCS scale non-

linear events is probably due to enhanced mixing associated with the increased wind speeds (i.e. the warmer water near the surface is being mixed with the cooler water below). This process would initially cause a warming at the 0.45 m depth as indicated by the first convective bin.

The composite air-sea temperature difference response to the four different types of convective organization is shown in Fig. 4.9. The SST changes were very small compared to the air temperature changes, and therefore the air-sea temperature difference response were dominated by changes in the surface air temperature. Since the MCS scale events produced the greatest air temperature depressions, they also exhibited the greatest increase in the air-sea temperature difference. The air-sea temperature difference increased by about 3° C for these events. On the other hand, the air-sea temperature difference increased by only about 2° C and 1.5° C for the sub-MCS scale non-linear and linear events respectively. During the recovery period the air-sea temperature difference decreased to approximately the pre-convective environmental value. The rate at which the air-sea temperature decreased was approximately the same for the sub-MCS scale events. The air-sea temperature difference decreased at a slower rate for the MCS scale non-linear events, most likely due to the presence of stratiform precipitation and extensive cloud cover reducing the incoming solar radiation.

The composite response of the transfer coefficient for heat to the four different types of convective organization is shown in Fig. 4.10. The transfer coefficient for heat, which is a function of the atmospheric surface layer stability, changed very little in response to convective activity. As a general rule the transfer coefficient for heat

decreases slightly during the convectively active period. The sub-MCS scale non-linear events exhibited the largest change (a reduction of slightly more than 10%). These small changes in the transfer coefficient for heat will have almost no effect on the resultant sensible heat fluxes.

The composite surface sensible heat flux response to the four different types of convective organization is shown in Fig. 4.11. The pre-convective sensible heat flux values were approximately the same for all types of convective organization (between 5 W m^{-2} and 10 W m^{-2}). During the convectively active period the sensible heat flux increased significantly for all types of convective organization. However, the magnitude of the enhancement was very dependent on the type of convective organization. The sub-MCS scale events showed the smallest enhancement, increasing from about 5 W m^{-2} to nearly 20 W m^{-2} during the convectively active period. The enhancements for the MCS scale events were much greater, increasing from about 5 W m^{-2} to over 45 W m^{-2} for the linear events and from about 10 W m^{-2} to over 60 W m^{-2} for the non-linear events. The reason the MCS scale events enhanced the sensible heat flux much more than the sub-MCS scale events was that the MCS scale events were associated with greater wind speed enhancements and air temperature depressions than the sub-MCS scale events. This was most likely a result of stronger convection and downdrafts associated with the more organized convective systems developing in a favorable environment (Rotunno et al., 1988). During the early recover periods the sensible heat flux decreased significantly due largely to decreased wind speeds, but the sensible heat flux remained enhanced due to enhanced air-sea temperature differences. The rate at which the sensible

heat flux decreases during the recovery is primarily controlled by the rate at which the surface air temperature recovers to the pre-convective environmental value. The relatively weak variations in the transfer coefficient for heat played practically no role in the sensible heat flux response to the different types of convective organization.

4.5 Latent Heat Flux

The surface latent heat flux is thought to be primarily controlled by the wind speed and the difference between the saturation specific humidity at the SST and the specific humidity of the air (ref. Eqn. 3.3). In the convectively active regions of precipitating systems, the combined effect of increased wind speed and decreased specific humidity lead to an enhanced latent heat flux.

Figure 4.12 shows the composite specific humidity response to the four different types of convective organization. During the convectively active period the specific humidity decreased for each type of convective organization. The specific humidity decrease for the MCS scale events (about 1.5 g kg^{-1}) was larger than the typical decrease for the sub-MCS scale events (slightly more than 0.5 g kg^{-1}). This again can be attributed to the MCS scale convection with attendant better defined, stronger downdrafts compared to the sub-MCS scale events. During the recovery period, the specific humidity increased fairly rapidly to the pre-convective environmental value for all types of convective organization with the exception of the MCS scale non-linear events, which exhibited nearly constant depressed values for more than half of the recovery period. This response may be linked to the presence of relatively dry mesoscale downdrafts below the associated stratiform precipitation and/or to other convective elements which

may have been embedded within the stratiform precipitation. It should be noted that the presence of mesoscale downdrafts below the stratiform precipitation has not been explicitly demonstrated in this study, however, their presence would be expected based on previous studies (Houze, 1977; Zipser, 1977; Gamache and Houze, 1982). The MCS scale linear events, which typically also have significant trailing stratiform regions, did not exhibit the same behavior. This may have been due to the absence of embedded convective elements within the stratiform precipitation in the MCS scale linear events and/or to the mesoscale downdrafts associated with the two MCS scale convective classifications having different kinematic structures. Future wind field retrieval studies using the Doppler wind data will presumably provide some additional information on the structure of the mesoscale downdrafts associated with these two classes of convective organization.

Figure 4.13 shows the composite response of the saturation specific humidity at the SST to the four different types of convective organization. The changes in the saturation specific humidity are very small since they are controlled by the SST, which changes very little itself. For the sub-MCS scale linear and MCS scale events the saturation specific humidity remains nearly constant near 25 g kg^{-1} (varies by less than 1%). For the sub-MCS scale non-linear events, the pre-convective environmental values are nearly 27 g kg^{-1} due to the higher SSTs. By the end of the recovery period, the values decrease to about 26 g kg^{-1} (a decrease of about 3% from the pre-convective environment). These changes were very small and will have a very limited affect on the surface latent heat flux.

Figure 4.14 shows the composite air-sea humidity difference response to the four different types of convective organization. For the sub-MCS scale non-linear events, the changes in the saturation specific humidity at the SST are primarily responsible for the observed air-sea humidity difference, which decreases throughout the composite time series. For all other types of convective organization, the changes in the specific humidity are largely responsible for the observed air-sea humidity changes. For the sub-MCS scale linear events, the air-sea humidity difference increased by only about 0.5 g kg^{-1} during the last part of the convectively active period and at the very beginning of the recovery period. For the MCS scale events, the air-sea humidity difference increased by slightly more than 1 g kg^{-1} during the convectively active period and remained enhanced for about half of the recovery period.

Figure 4.15 shows the composite response of the transfer coefficient for moisture to the four different types of convective organization. As with the transfer coefficient for heat, the changes in the transfer coefficient for moisture were very small. During the convectively active period the transfer coefficient for moisture typically decreased. The small changes in the transfer coefficient for heat will have only a very limited effect on the surface latent heat flux.

The composite latent heat flux response to the four different types of convective organization is shown in Fig. 4.16. For all types of convective organization the latent heat flux approximately doubled during the convectively active period. During this period, the enhanced wind speed was primarily responsible (decreased specific humidity plays a limited role) for the observed latent heat flux enhancement. During the recovery

period, the latent heat flux decreased significantly as the wind speeds subsided. However, the latent heat flux remains slightly enhanced (by between 25% and 50% from the pre-convective environment) during the first few recovery bins for the MCS scale events. These enhancements can be partly explained by enhanced air-sea surface humidity differences (wind speeds were also slightly enhanced during this period) observed during these time periods. This enhanced air-sea humidity difference can be attributed to the boundary layer still recovering from the initial changes caused by the convective scale downdrafts, as well as to the mesoscale downdraft accompanying the stratiform precipitation. The latent heat flux enhancements during the recovery period are much weaker than the enhancements during the convectively active period, however, the duration of the enhancements during the recovery period was roughly three times the duration of the convectively active period.

4.6 Rainfall Heat Flux

When precipitation occurs at the ocean's surface, it has a sensible heat flux associated with it because the temperature of the precipitation is generally different from that of the ocean's surface. The magnitude of this heat flux is controlled by the rain rate, ocean temperature, and the temperature of the precipitation. Gosnell et al. (1995) developed a relation which states that the sensible heat flux associated with rainfall is proportional to the rain rate and the air-sea temperature difference (ref. Eqn. 3.22).

Figure 4.17 shows the composite sensible heat flux associated with rainfall response to the four different types of convective organization. The heat flux associated with rainfall peaks during the convectively active period for each type of convective

organization due to the peak rain rates and air-sea temperature differences both being observed during this period. The MCS scale non-linear event composite produced a peak rainfall heat flux (about 100 W m^{-2}) which was nearly double the peak sensible heat flux. For these events the rainfall heat flux was substantially higher than the other types of convective organization. This is because for the MCS scale non-linear events the largest rain rates and air-sea temperature differences occurred concurrently, and late in the convectively period. For the other event types, the peak rain rates occurred early in the convectively active period, before the air-sea temperature difference had reached its peak value. Note however, that these smaller rainfall heat fluxes were still approximately equal to the corresponding sensible heat flux. During the recovery periods the rainfall heat flux values were greatly reduced due mainly to reduced rain rates.

4.7 Evaluation of Composites

In order to evaluate how well the composite time series represent the individual cases, a correlation analysis was performed. The average correlation coefficient between the individual cases and the respective composite time series was calculated for each type of convective event. This was done for each variable that was discussed in previous sections. The results of this analysis are summarized in Table 4.1. The correlation coefficients for the composites produced by Young et al. (1995) are also shown. The correlation coefficients obtained for the current study are higher for nearly every category, thereby implying that the composites produced in the current study provide an improved representation of the surface flux response to atmospheric convection. These improvements can be attributed to the use of a classification scheme which differentiated

between the different types of convective organization and to the use of a more sophisticated compositing scheme, differentiating between the convectively active and recovery phases of the individual time series. The use of this compositing scheme allowed for the use of two separate temporal scales (i.e. the convectively active bins had a finer temporal resolution than the recovery bins), hence the response to convective and recovery processes could both be well represented in the final composite analysis.

Previous studies have primarily focused on the boundary layer response to MCS scale systems. The results of the current study are generally consistent with these studies (see Table 4.2). The Johnson and Nicholls (1983) study was a composite analysis of an intense squall line observed during GATE, Addis et al. (1984) analyzed 49 GATE gust-fronts, Young et al. (1995) produced a composite study similar to the current study from TOGA COARE, and Jabouille et al. (1996) analyzed a modeling study based on TOGA COARE observations. The results of the current study are basically in line with all of these previous studies which is encouraging since other composite analyses, an individual event from GATE, and model results are all represented in Table 4.2. The analysis of Young et al. (1995) was done to document the evolution of convective wakes during TOGA COARE and in doing so they used hourly-averaged data in equally spaced bins. This practice effectively smoothed the response during the convectively active period, thereby leading to the current study showing larger magnitude changes in response to convective activity. The results of this study represent fairly well the individual squall lines reported by Johnson and Nicholls (1983) and Jabouille et al. (1996). Since sub-MCS scale events have not systematically been studied in this manner prior to this, no

real comparisons with previous studies can be made. The current study is the first of its kind that systematically describes the effects that specific convective structures have on the atmospheric boundary layer. It is evident from these results that the surface flux response is dependent on the type of convective event producing the response.

Table 4.1 Summary of mean correlation coefficients between the individual cases and the composite time series. Values given are the mean correlation coefficients (r) for the sub-MCS scale non-linear (SM-NL), sub-MCS scale linear (SM-L), MCS scale non-linear (M-NL), and MCS scale linear (M-L) events. Also provided are the values obtained by Young et al. (1995) for their composites from a COARE pilot cruise (Y95 PC) and the COARE IOP (Y95 IOP).

VARIABLE	SM-NL	SM-L	M-NL	M-L	Y95 PC	Y95 IOP
Relative Wind Speed	0.51	0.65	0.70	0.54	0.50	0.23
Drag Coefficient	0.38	0.10	0.63	0.53	-	-
Wind Stress	0.45	0.62	0.71	0.54	0.49	0.37
Sensible Heat Flux	0.80	0.72	0.89	0.80	0.52	0.63
Air Temperature	0.90	0.79	0.91	0.86	0.71	0.81
Sea Surface Temperature	0.74	0.40	0.56	0.42	0.25	0.31
Transfer Coefficient for Heat	0.34	0.40	0.50	0.34	-	-
Latent Heat Flux	0.62	0.62	0.71	0.54	0.59	0.41
Specific Humidity	0.50	0.48	0.73	0.63	0.23	0.11
Surface Saturation Specific Humidity	0.70	0.32	0.54	0.46	0.26	0.38
Transfer Coefficient for Moisture	0.34	0.42	0.49	0.36	-	-
Rate of Air Temperature Change	0.81	0.81	0.83	0.81	-	-
Air-Sea Humidity Difference	0.52	0.46	0.63	0.62	0.15	0.23
Air-Sea Temperature Difference	0.86	0.78	0.90	0.86	0.68	0.82
Maximum Rain Rate	0.44	0.75	0.65	0.71	0.40	0.85
Rainfall Heat Flux	0.81	0.61	0.62	0.60	-	-

Table 4.2 Comparison of results for the MCS scale linear events (M-L) to previous studies which examined similar cases. Values given are maximum or minimum values during the convectively active period and the numbers in parentheses are the maximum change from the pre-convective environment. The studies shown are Johnson and Nicholls (1983) (JN83), Addis et al. (1984) (A84), Young et al. (1995) (Y95), and Jabouille et al. (1996) (J96).

VARIABLE	M-L	JN83	A84	Y95	J96
Max. Wind Speed (m s^{-1})	9 (4)	15 (10)	7.7 (2.6)	6 (1)	11 (8)
Max. Wind Stress (N m^{-2})	02 (0.15)	-	-	0.08 (0.02)	-
Min. Air Temperature ($^{\circ}\text{C}$)	25 (-3)	22 (-4)	24.2 (-1.9)	26 (-1.5)	24 (-3)
Max. Air-Sea Temp. Difference ($^{\circ}\text{C}$)	4 (3)	-	-	3 (1.5)	-
Max. Sensible Heat Flux (W m^{-2})	55 (40)	100 (80)	78 (63)	35 (20)	70 (60)
Min. Specific Humidity (g kg^{-1})	18.0 (-1.5)	13.5 (-2.5)	16.7 (-0.1)	18.5 (-0.5)	18.2 (-1)
Max. Air-Sea Humidity Difference (g kg^{-1})	7 (1.5)	-	-	6 (0.2)	-
Max. Latent Heat Flux (W m^{-2})	225 (100)	400 (300)	356 (175)	155 (50)	275 (175)
Max. Rain Rate (mm hr^{-1})	14	-	-	7.5	-
Max. Rainfall Heat Flux (W m^{-2})	40	-	-	40	-
Description of Study	TOGA COARE Composite	Intense GATE Squall Line	Average of 49 GATE Gust-Fronts	TOGA COARE Composite	TOGA COARE Modeling Study

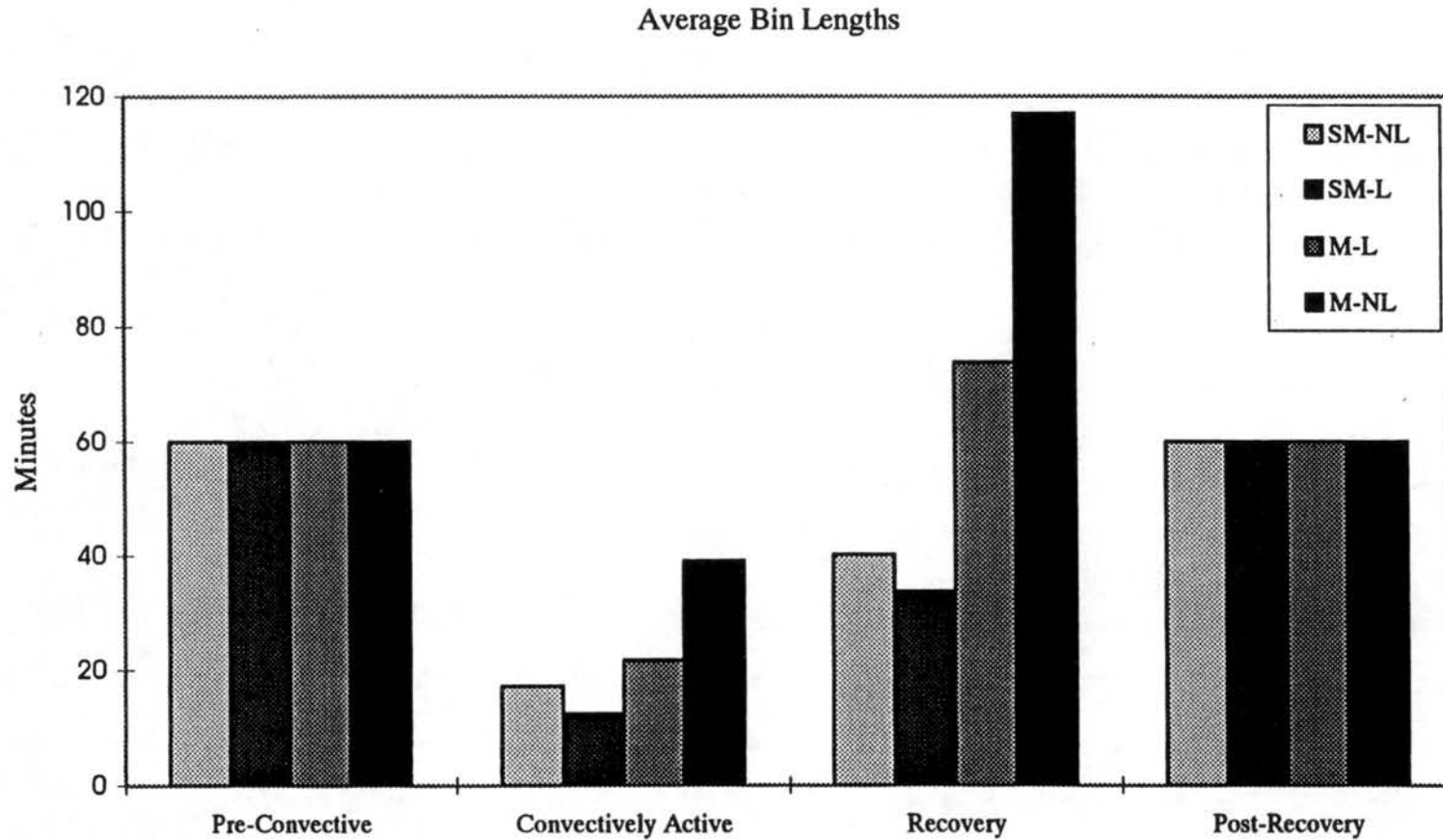


Figure 4.1 Average length of each bin for the pre-convective, convectively active, recovery, and post-recovery periods. The four classifications of convective organization are sub-MCS scale non-linear (SM-NL), sub-MCS scale linear (SM-L), MCS scale non-linear (M-NL), and MCS scale linear (M-L) events.

Maximum Rain Rate in 4.5 km Box
Surrounding the IMET Buoy

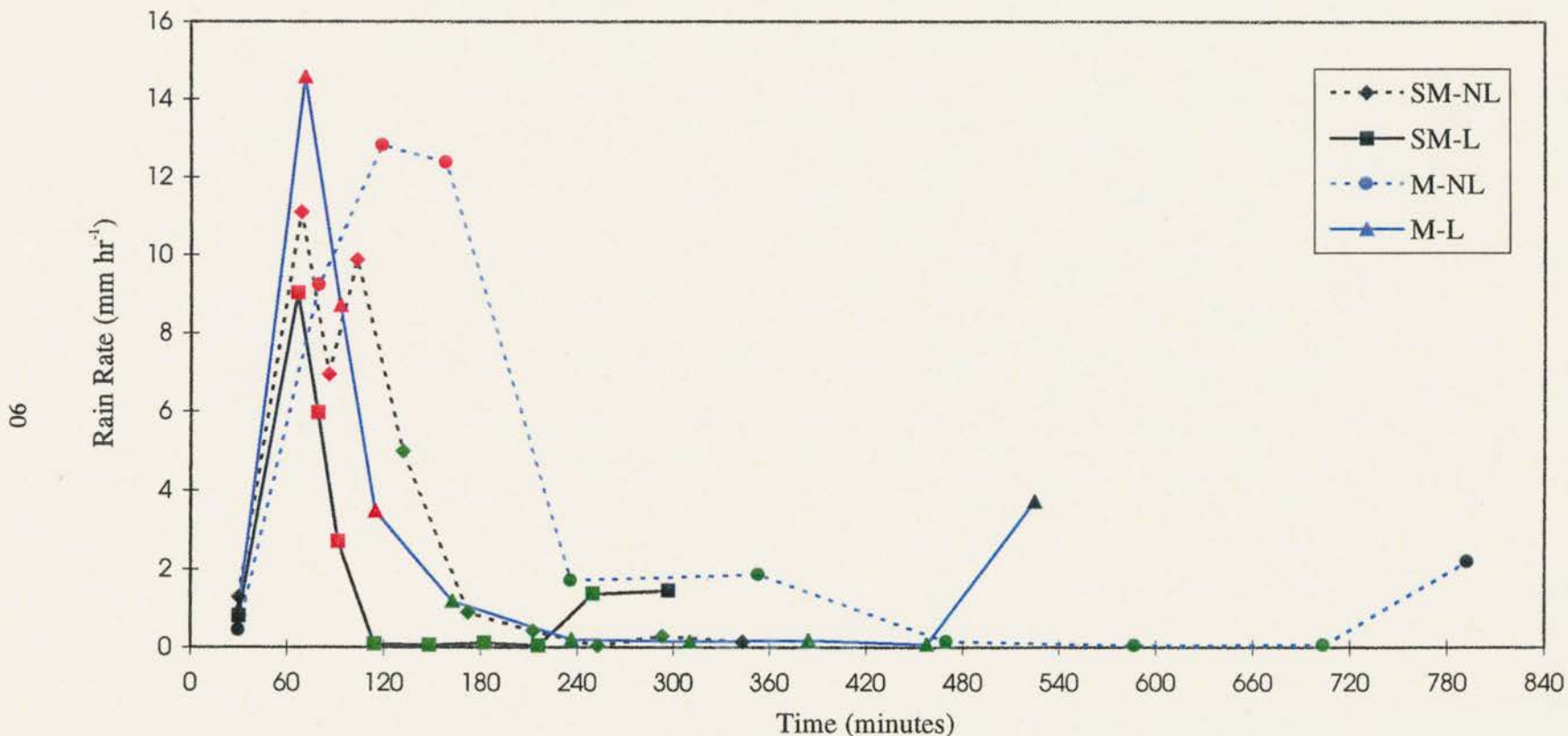


Figure 4.2 Composite time series of the maximum radar derived rain rate within a 4.5 km box surrounding the nominal location of the IMET buoy for the sub-MCS scale non-linear (SM-NL), sub-MCS scale linear (SM-L), MCS scale non-linear (M-NL), and MCS scale linear (M-L) classifications of convective organization. The red markers represent the convectively active periods and the green markers represent the recovery periods for each respective class of convective organization. The black markers represent the pre-convective and post-recovery periods.

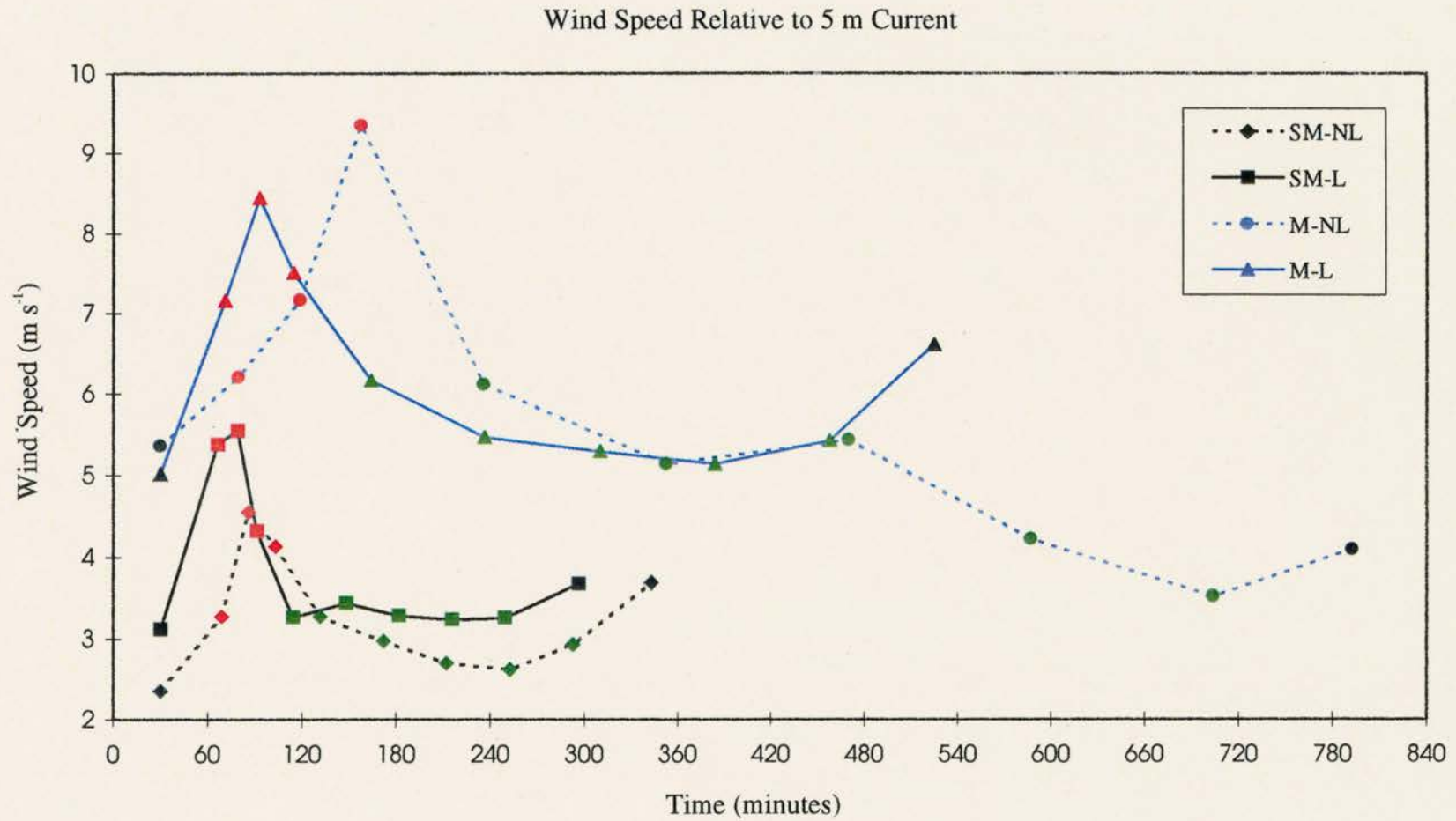


Figure 4.3 Same as Fig. 4.2 except for the wind speed relative to the 5 m current.

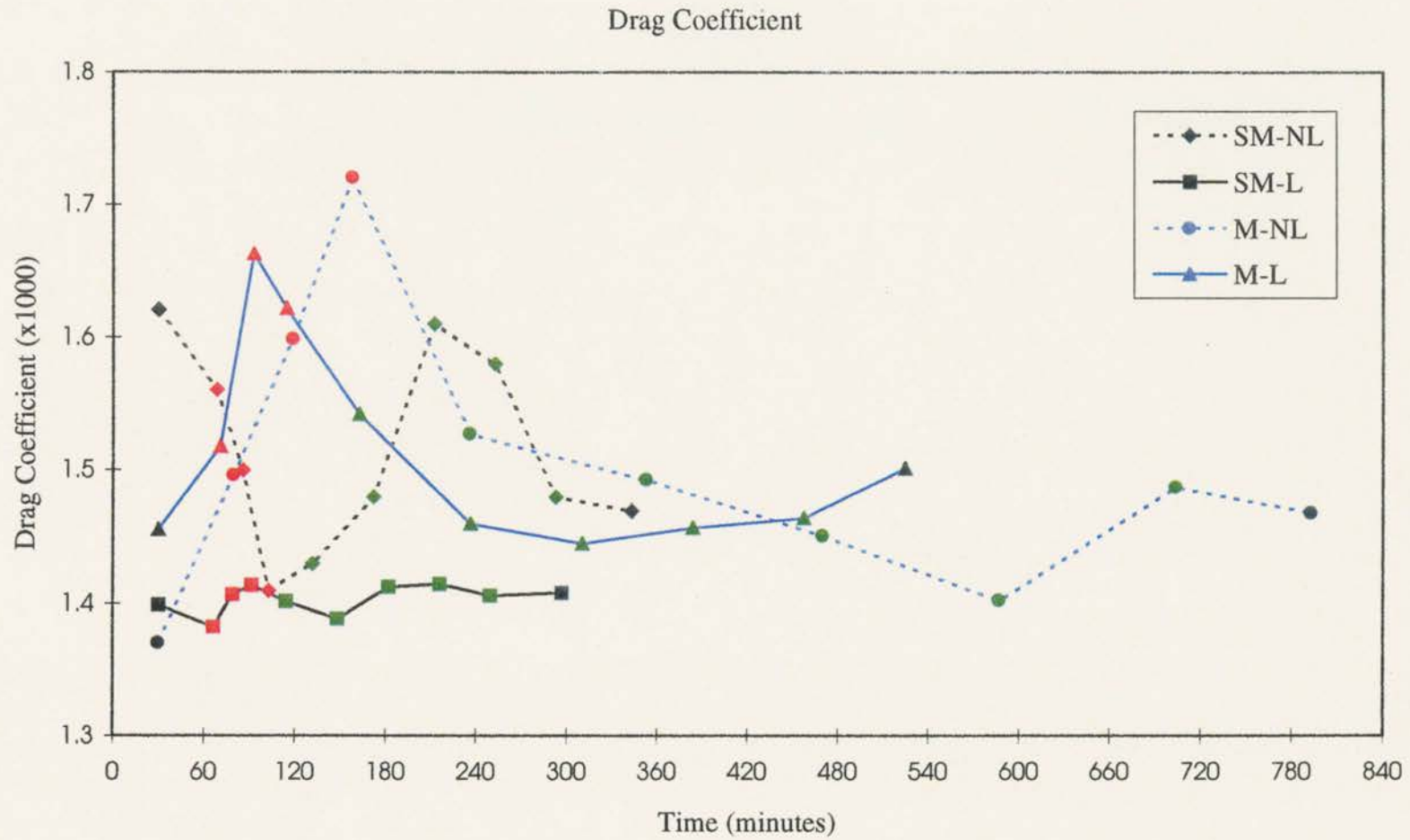
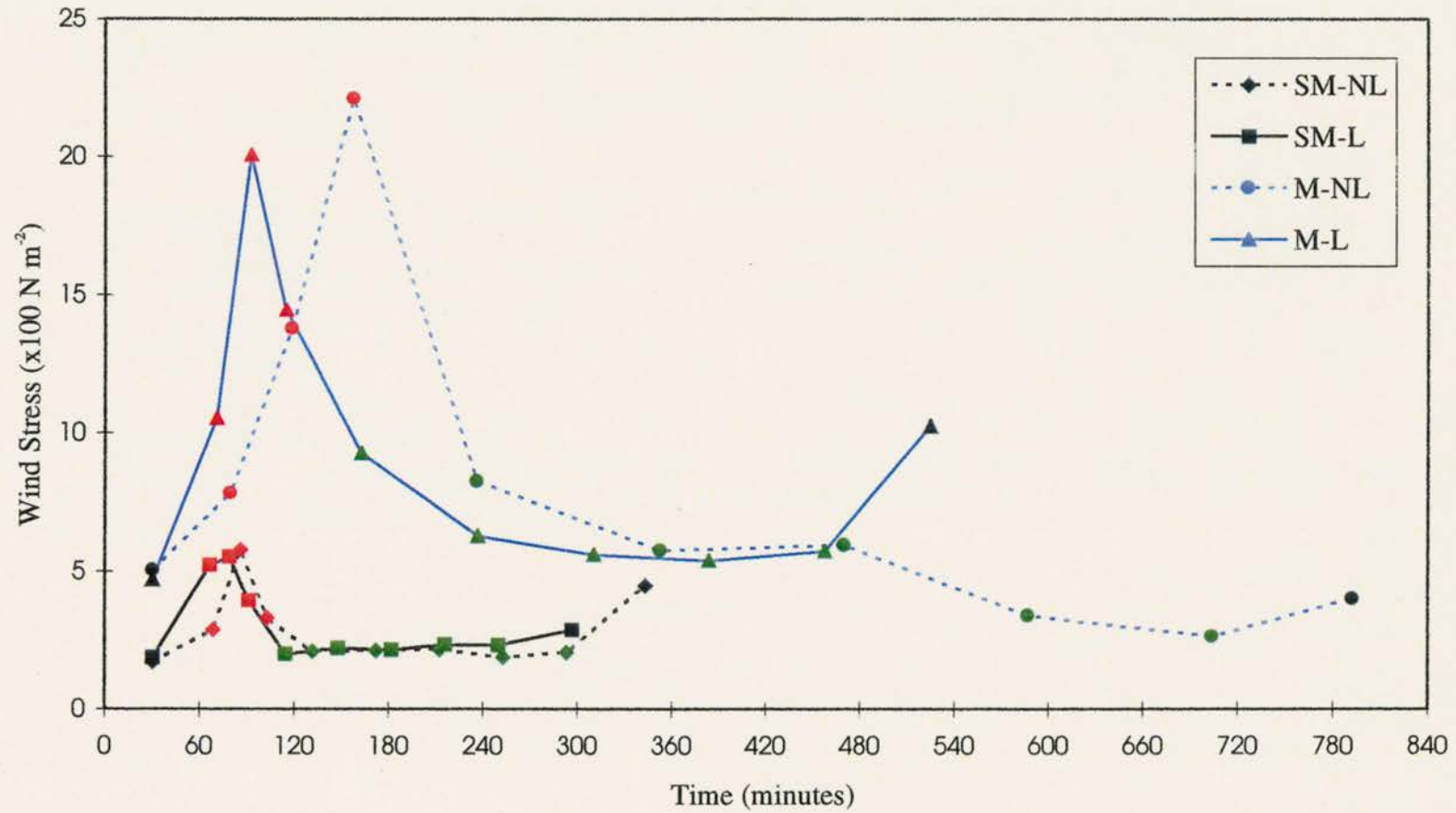


Figure 4.4 Same as Fig. 4.2 except for drag coefficient.

Wind Stress



93

Figure 4.5 Same as Fig. 4.2 except for wind stress.

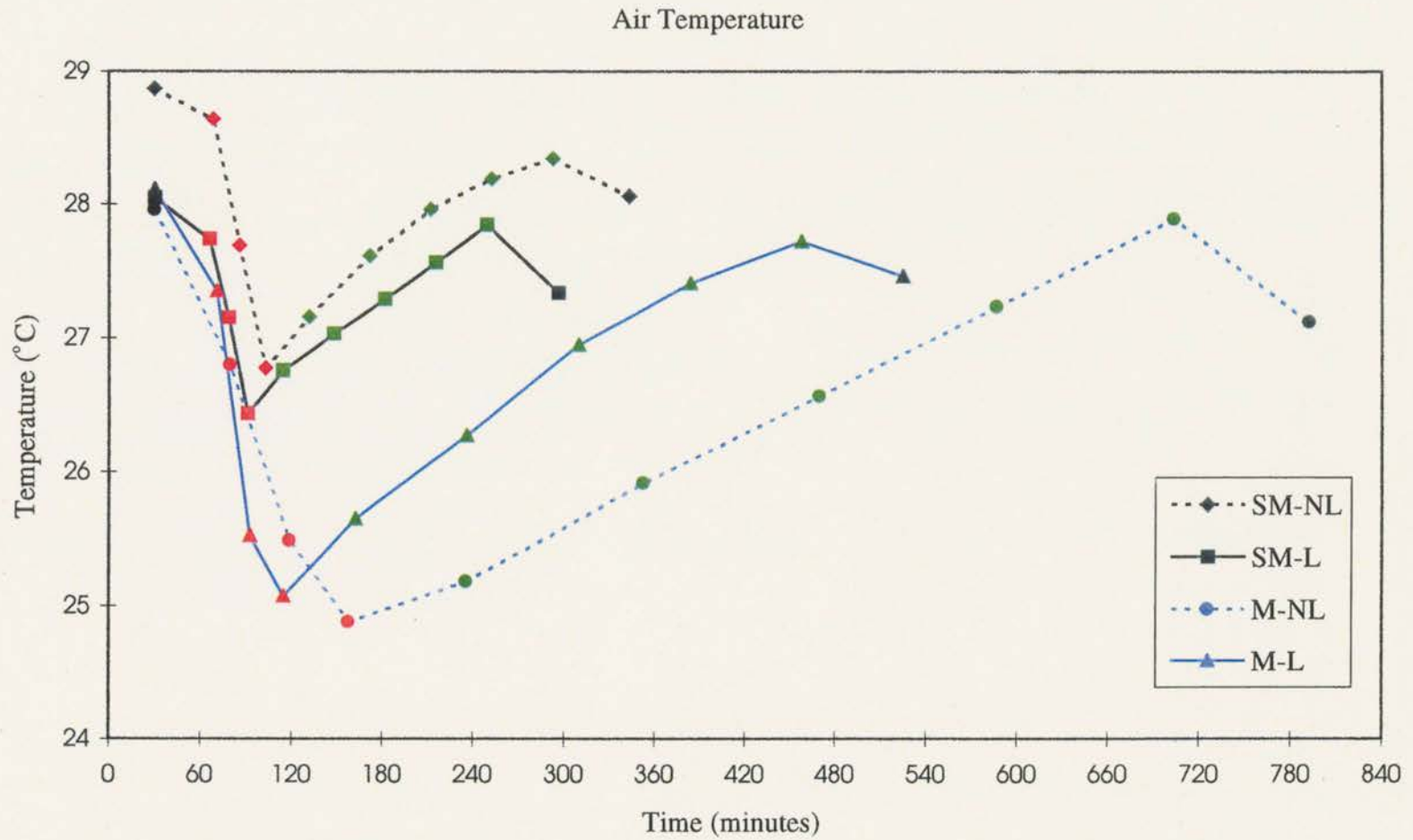


Figure 4.6 Same as Fig. 4.2 except for air temperature.

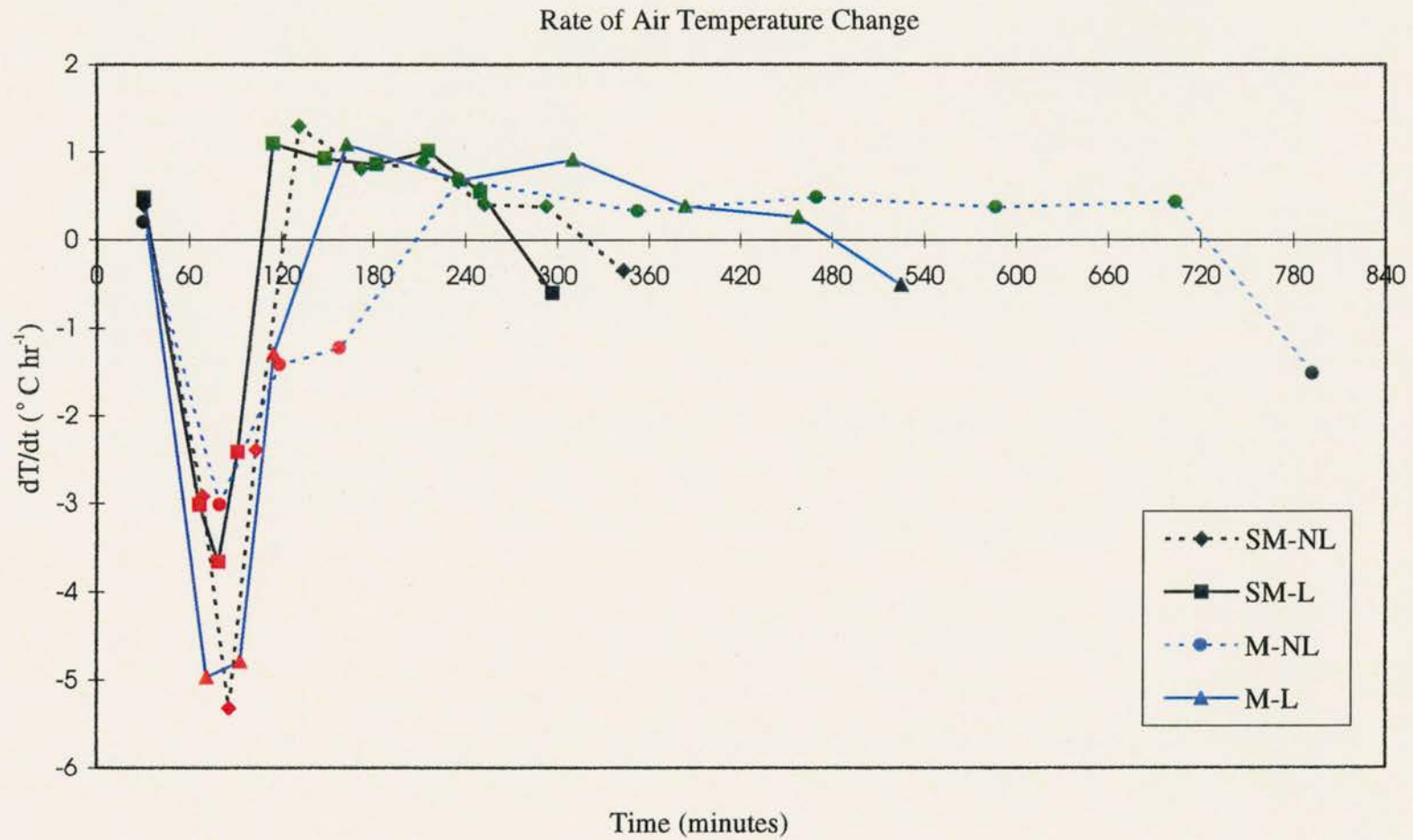


Figure 4.7 Same as Fig. 4.2 except for rate of air temperature change.

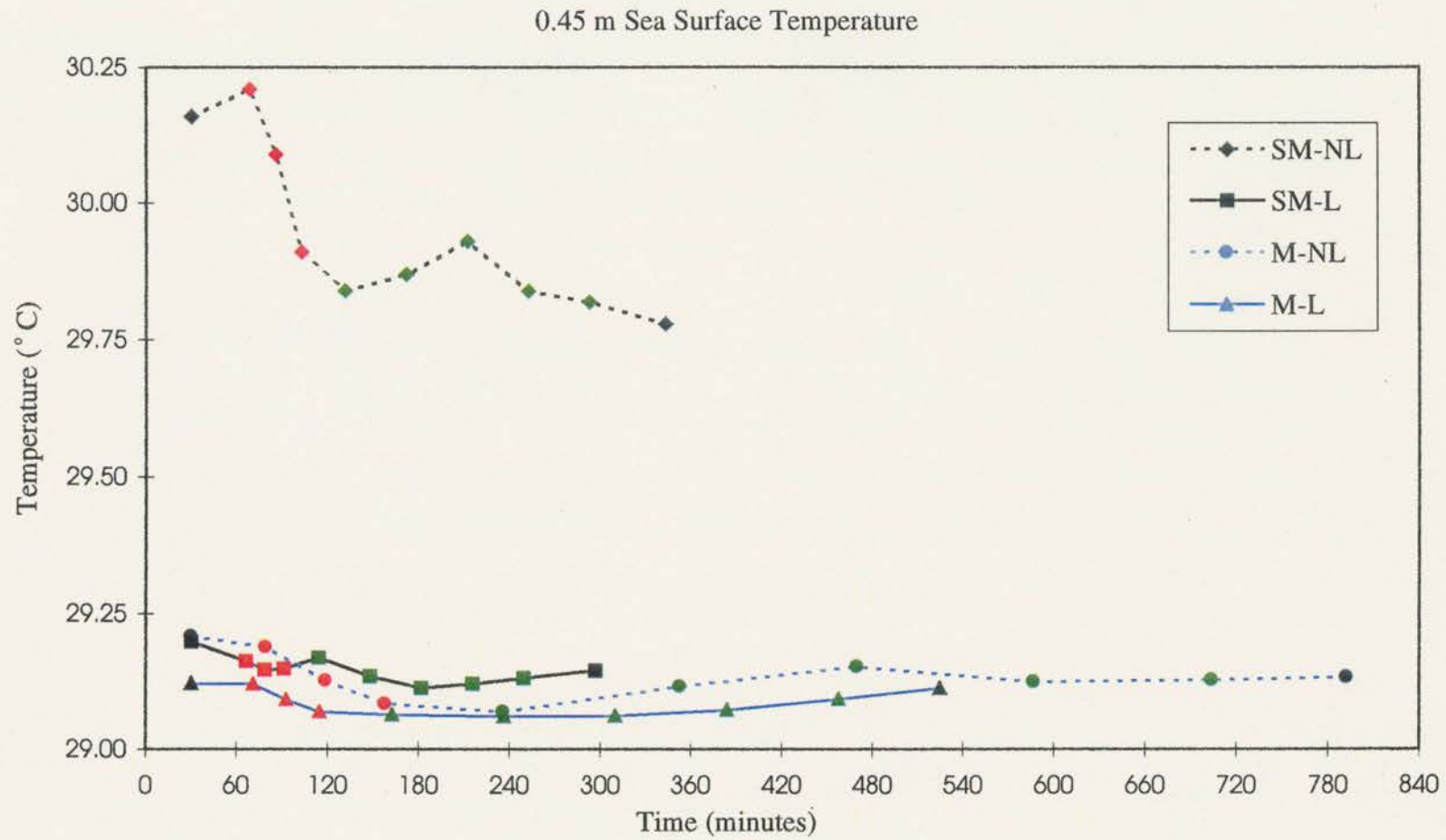


Figure 4.8 Same as Fig. 4.2 except for sea surface temperature (at a depth of 0.45 m).

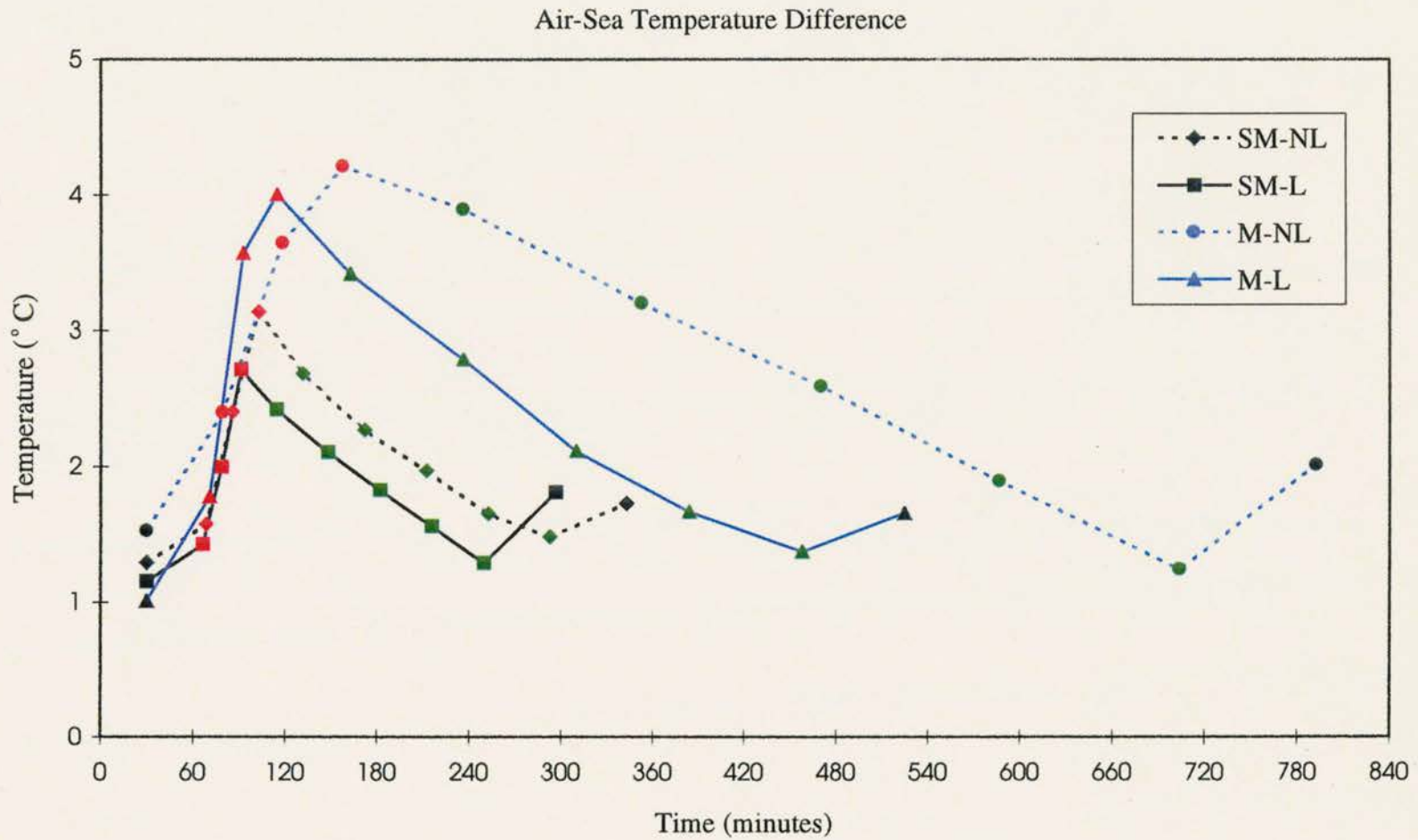
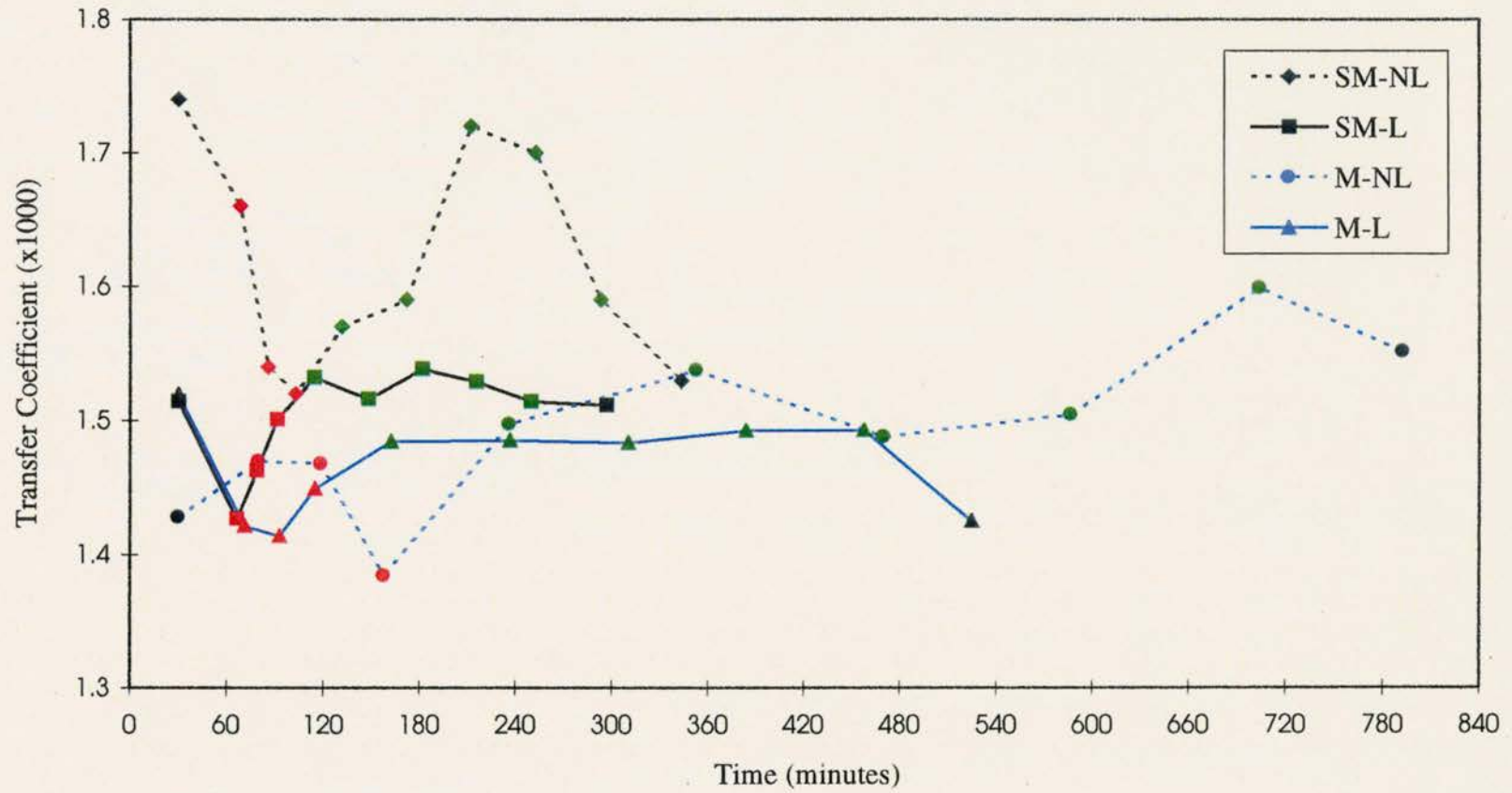


Figure 4.9 Same as Fig. 4.2 except for air-sea temperature difference.

Transfer Coefficient for Heat



86

Figure 4.10 Same as Fig. 4.2 except for transfer coefficient for heat.

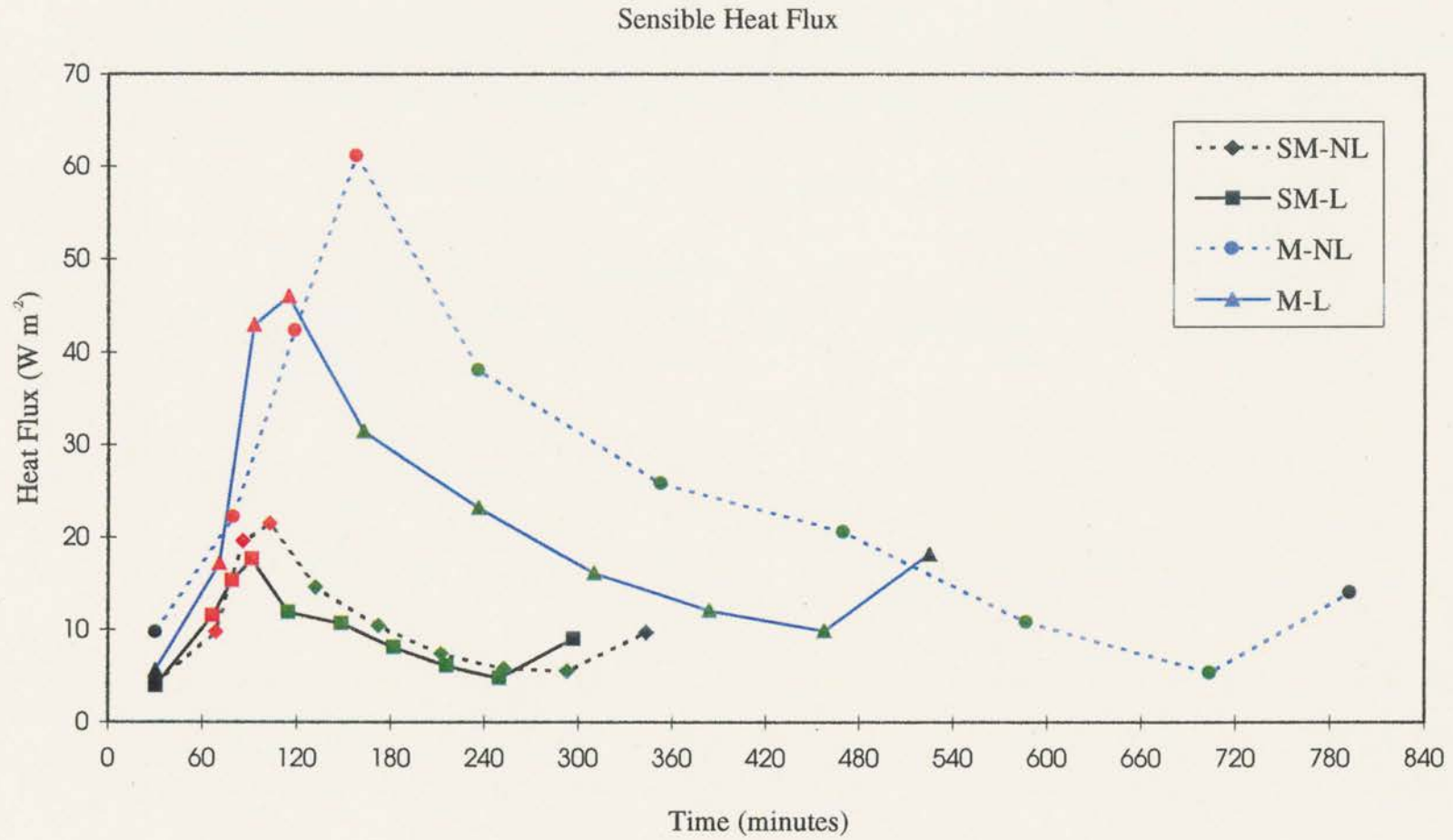


Figure 4.11 Same as Fig. 4.2 except for sensible heat flux.

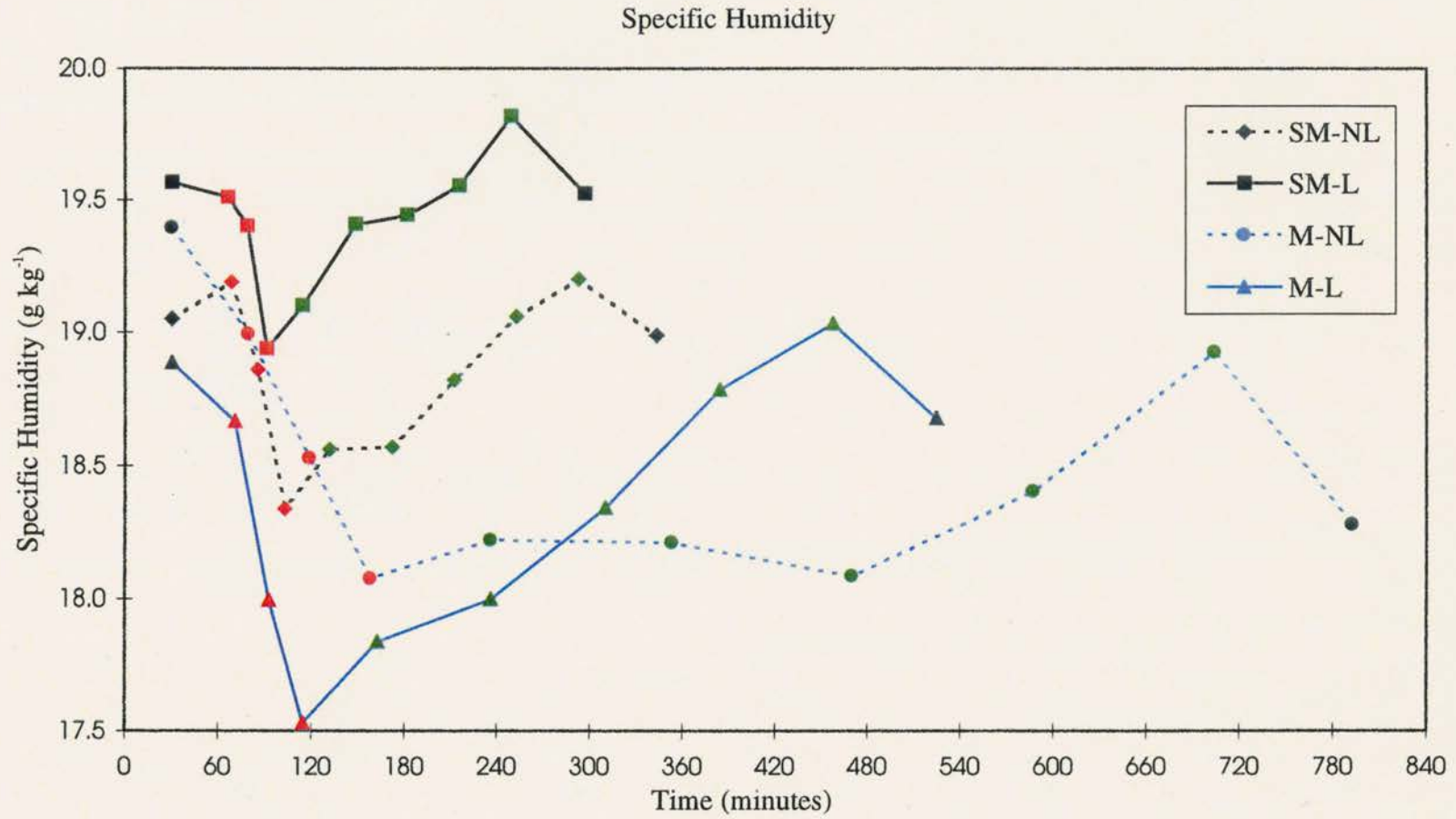


Figure 4.12 Same as Fig. 4.2 except for specific humidity.

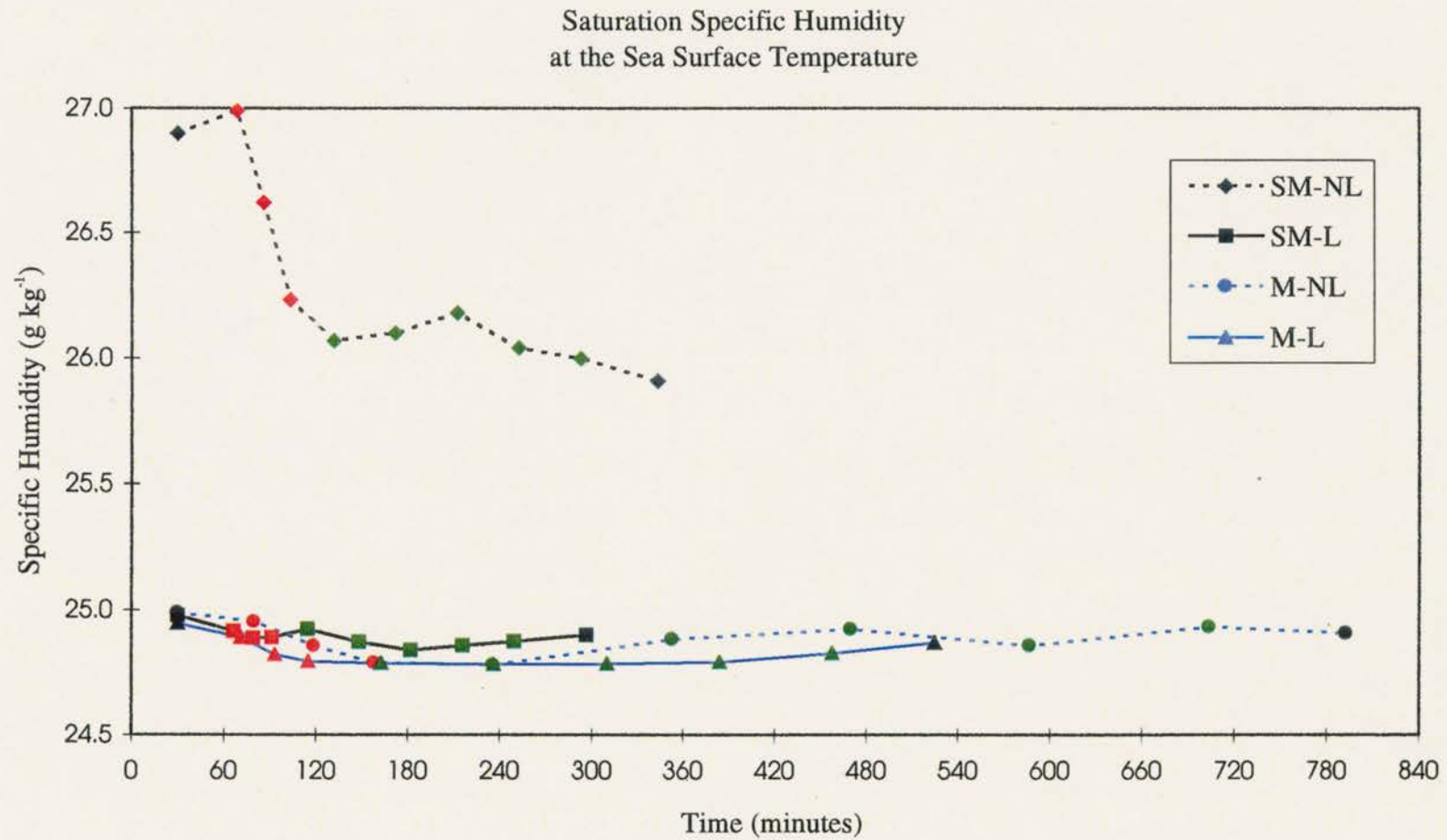


Figure 4.13 Same as Fig. 4.2 except for saturation specific humidity at the sea surface temperature.

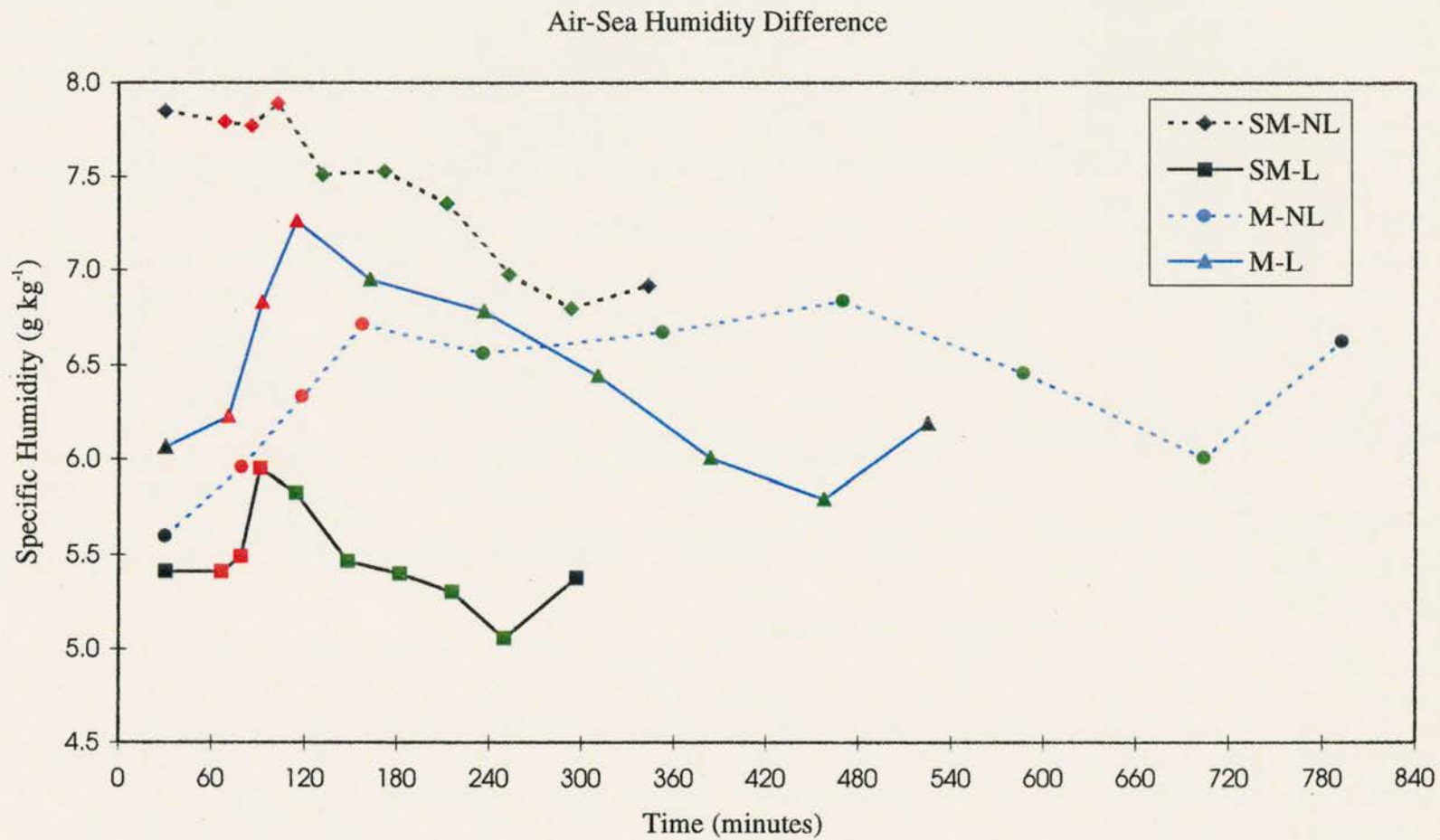


Figure 4.14 Same as Fig. 4.2 except for air-sea humidity difference.

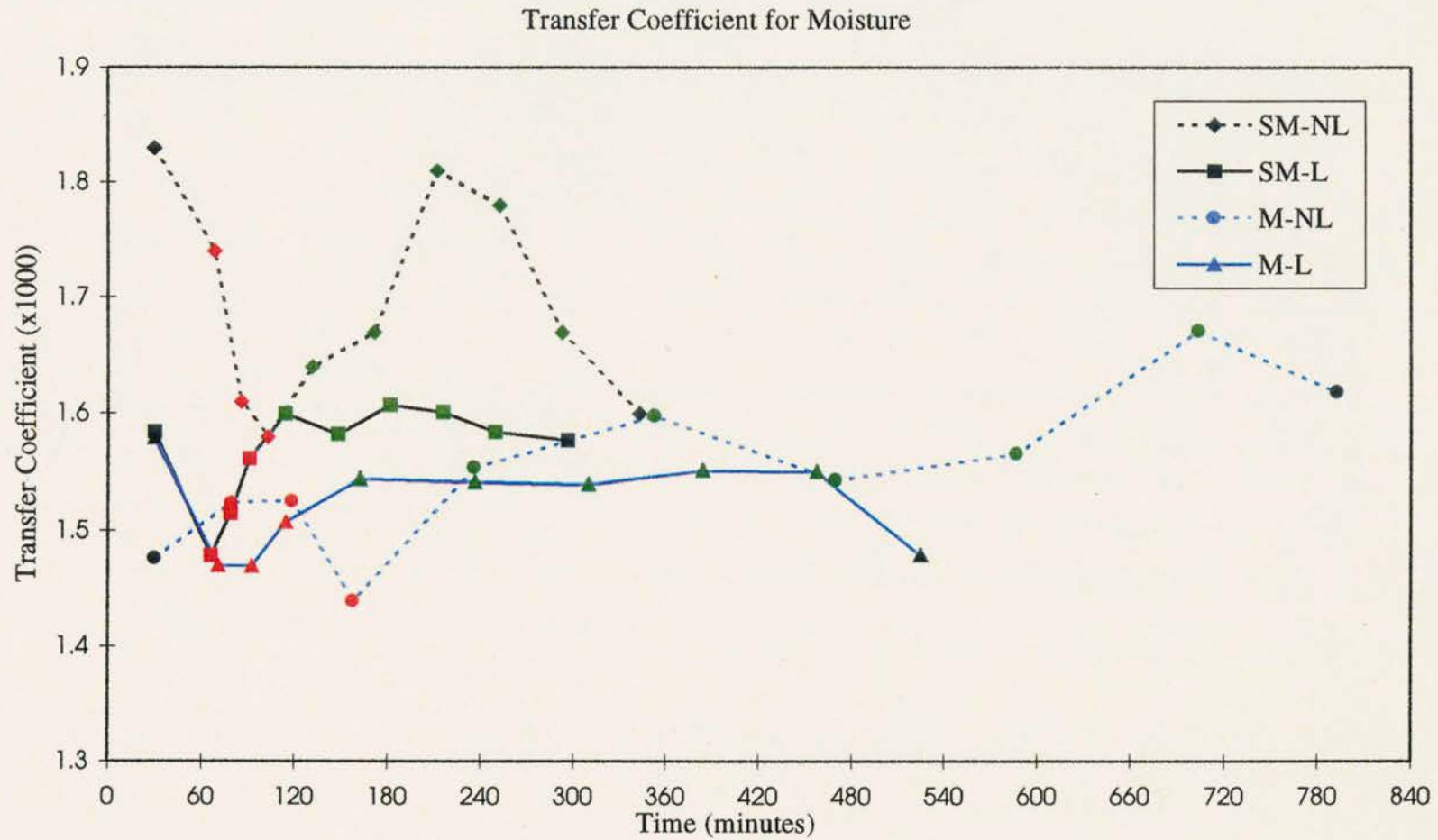


Figure 4.15 Same as Fig. 4.2 except for transfer coefficient for moisture.

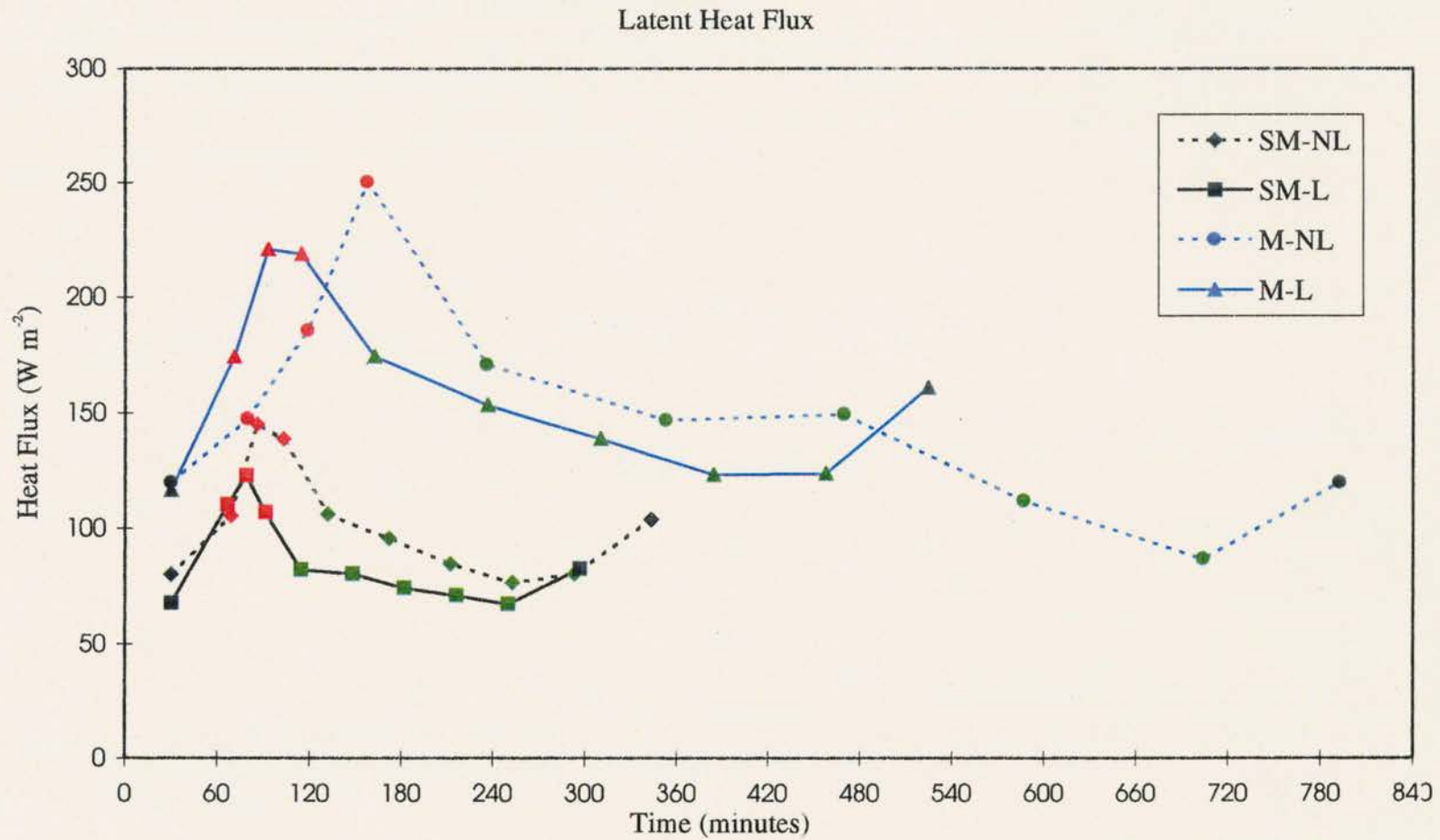


Figure 4.16 Same as Fig. 4.2 except for latent heat flux.

Sensible Heat Flux Associated with Rainfall

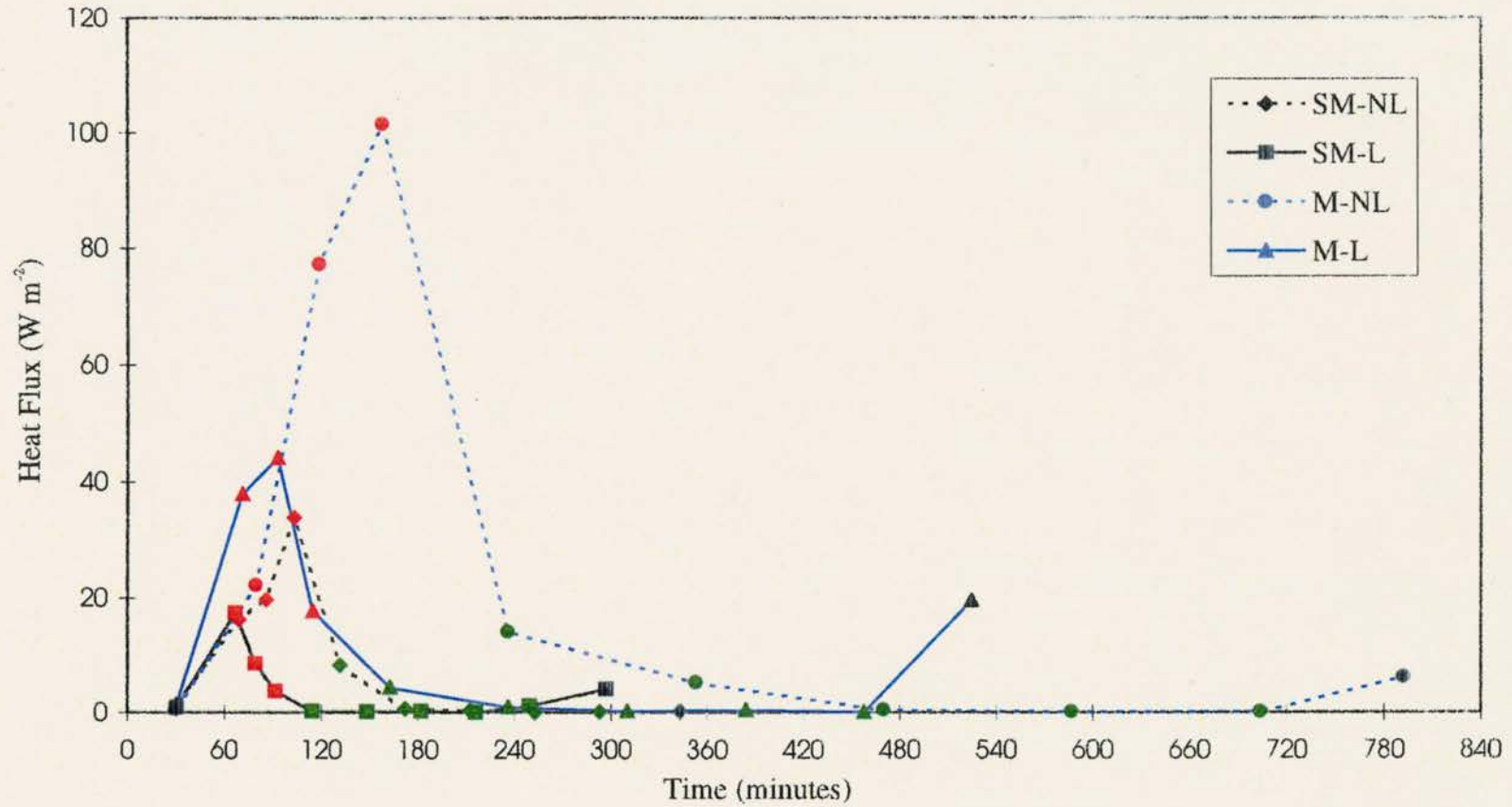


Figure 4.17 Same as Fig. 4.2 except for sensible heat flux associated with rainfall.

CHAPTER 5

CONCLUSIONS

The primary goal of the current study is to provide a detailed description of how four different classes of convective organization observed during TOGA COARE affect the surface fluxes of heat, moisture, and momentum during both the convectively active and recovery periods. Previous studies have explored the effects of convective systems on the boundary layer, however, none have systematically quantified the boundary layer's response to different organizational modes of convection. In order to achieve this goal, composite analyses of the surface fluxes and the pertinent bulk variables were constructed. These composite analyses showed that the different types of convective organization effected the atmospheric boundary layer in a similar manner. However, the magnitude and duration of the response was highly dependent on the mode of convective organization, with the larger, more organized systems (which were typically the more intense Mesoscale Convective Systems) producing the greatest boundary layer response.

The sub-MCS scale non-linear and linear events both produced a relatively small response at the surface, largely attributable to the fact that these systems tend to develop in environment conditions which inhibit their vertical development, namely the presence of dry mid level air (Rickenbach and Rutledge, 1996). These events typically had short

lifetimes, further limiting their impact on the surface fluxes. The sub-MCS scale linear events also tended to develop during periods of strong shear, leading Rickenbach and Rutledge (1996) to hypothesize that the shear may have been overly strong, thereby inhibiting the upscale development of these events.

The sub-MCS scale non-linear and linear event composites both showed that the wind stress increased from approximately 0.02 N m^{-2} (pre-convective value) to nearly 0.06 N m^{-2} during the convectively active period. During this same period, the latent heat flux increased from approximately 80 W m^{-2} to 145 W m^{-2} for the non-linear event types and from approximately 70 W m^{-2} to 120 W m^{-2} for the linear event types. Both the wind stress and latent heat flux enhancements were primarily in response to enhanced wind speeds, which nearly doubled during the convectively active period. The sensible heat flux increased from approximately 5 W m^{-2} to roughly 20 W m^{-2} for both the non-linear and linear sub-MCS scale classifications. These enhancements were in response to the enhanced wind speed and air-sea temperature difference, which peaked near 3° C during the convectively active period. The sensible heat flux associated with rainfall also peaked near 35 W m^{-2} and 20 W m^{-2} for the non-linear and linear events respectively.

During the recovery phase for the sub-MCS scale events, the boundary layer quickly recovered to a condition similar to the pre-convective environment. During this phase the convective scale downdrafts were presumably no longer directly affecting the boundary layer and therefore the wind stress and latent heat flux decreased rapidly in response to the decreasing wind speed. The sensible heat flux also initially decreased

significantly, however, it decreased more slowly as the boundary layer air temperature recovered to nearly its pre-convective value.

Despite the relatively short duration and limited enhancements in the surface fluxes, the sub-MCS scale non-linear events produced the greatest changes in SST. This can also be related to the typical environment within which this convective classification develops, namely weak winds and little cloud cover. As a result, a shallow diurnal warm layer was often present which made the upper ocean much more responsive to atmospheric forcing. The enhanced wind stress would have caused enhanced wind mixing, which mixed the warm near surface water with the cooler water below, leading to a decrease in SST.

Whereas the sub-MCS scale events produced a relatively small response at the surface, the MCS scale events produced a very large response, largely because the MCS scale events developed in an environment which was favorable for their vertical development and relatively long lifetime. This allowed the systems to organize on a larger scale and become more intense than the sub-MCS scale systems (Rickenbach and Rutledge, 1996). Both the non-linear and linear MCS scale events tended to develop during periods of relatively strong ascent throughout the troposphere. The troposphere was also much moister during the periods when the MCS scale events developed compared to the sub-MCS scale events.

During the convectively active phase, both the non-linear and linear MCS scale event composites showed that the wind stress increased from approximately 0.05 N m^{-2} to

0.2 N m^{-2} , due mainly to enhanced wind speeds during this period. The latent heat flux also increased from roughly 120 W m^{-2} to 250 W m^{-2} for the non-linear event types and from about 115 W m^{-2} to 220 W m^{-2} for the linear events during this same period. This response was also caused primarily by the enhanced wind speeds, but the air-sea humidity difference was also enhanced (to a lesser extent) during the convectively active phase. The sensible heat flux increased from about 10 W m^{-2} to 60 W m^{-2} and from roughly 5 W m^{-2} to 45 W m^{-2} for the non-linear and linear MCS scale events respectively, due to the combined effects of enhanced air-sea temperature differences and to enhanced wind speeds. The sensible heat flux associated with rainfall also peaked around 100 W m^{-2} for the non-linear events and 45 W m^{-2} for the linear events during the convectively active period. The non-linear events produced a much larger rainfall heat flux because the rainfall peaked coincided with the air-sea temperature difference peak, whereas for the linear events, the rainfall peaked prior to the air-sea temperature difference peak.

During the recovery phase, the MCS scale composites showed that the boundary layer recovered to nearly its pre-convective environmental state. For both the non-linear and linear MCS scale events, the wind stress decreased markedly at the beginning of the recovery phase in response to decreased wind speeds. The decreased wind speed also caused the latent and sensible heat fluxes to decrease significantly at the beginning of the recovery phase. However, the sensible heat flux remained enhanced during the majority of the recovery phase. The magnitude of the enhancement decreased with time as the boundary layer air temperature (and hence air-sea temperature difference) recovered to

pre-convective values. The latent heat flux also remained enhanced during the early part of the recovery phase. For the MCS scale non-linear events, the latent heat flux remained enhanced for a longer period of time than the linear events. This was due to the specific humidity remaining depressed for the first three recovery bins for the non-linear events, whereas for the linear events the specific humidity started to recover immediately following the convectively active phase. This response may have been due to the presence of other convective cells embedded within the stratiform region of the non-linear events injecting dry air into the boundary layer. The presence of embedded convective cells within the stratiform region of the MCS scale linear events was not generally observed. The mesoscale flow features associated with the stratiform region of the two MCS scale classes may have also had different structures, thereby producing different surface responses. Evidence from forthcoming wind field retrievals using the Doppler radar wind data will hopefully help answer this question.

The perturbations of the atmospheric boundary layer, which subsequently act to enhance the surface fluxes, were similar for all four types of convective organization since all of the convective systems contained convective scale downdrafts. The convective scale downdrafts caused increased wind speeds, decreased air temperatures, and to a lesser extent decreased specific humidities. However, the larger, more organized systems typically contained downdrafts which produced greater perturbations of the atmospheric boundary layer than the smaller, less organized systems. These greater perturbations of the boundary layer, in conjunction with the presence of significant

stratiform precipitation for the MCS scale events, caused the boundary layer recovery time to be much longer for the MCS scale events compared to the sub-MCS scale events.

These results lay the groundwork for further research. The composite analyses of surface fluxes of heat, moisture, and momentum could be used to drive a 1-D oceanic mixed layer model. In this way the individual and cumulative effects that the different classifications of convective organization have on upper ocean processes could be explored. These results could also be used to help determine the relative importance the different types of convective organization have on the overall heat budget of the tropical W. Pacific, which may aid in improving the air-sea flux parameterizations used in coupled ocean-atmosphere models.

REFERENCES

- Addis, R. P., M. Garstang, and G. D. Emmitt, 1984: Downdrafts from tropical oceanic cumuli. *Bound.-Layer Meteor.*, **28**, 23-49.
- Anderson, S. P., R. A. Weller, and R. B. Lukas, 1996: Surface buoyancy forcing and the mixed layer of the western Pacific warm pool: Observations and 1-D model results. *J. Climate*, submitted.
- Barnes, G., and M. Garstang, 1992: Subcloud layer energies of precipitating convection. *Mon. Wea. Rev.*, **110**, 102-117.
- Bruce, J. G., and E. Firing, 1974: Temperature measurements in the upper 10 m with modified expendable bathythermograph probes. *J. Geophys. Res.*, **79**, 4110-4111.
- Charnock, H., 1955: Wind stress on a water surface. *Quart. J. Roy. meteor. Soc.*, **81**, 639.
- Chen, S. S., R. A. Houze, and B. E. Mapes, 1996: Multiscale variability of deep convection in relation to large-scale circulation in TOGA COARE. *J. Atmos. Sci.*, **53**, 1380-1409.
- Elliott, G. W., 1974: Precipitation signatures in sea-surface-layer conditions during BOMEX. *J. Phys. Oceanogr.*, **4**, 498-501.
- Esbensen, S. K., and Y. Kushnir, 1981: The heat budget of the global oceans: An atlas based on estimates from surface marine observations. Climate Research Inst. Rep. No. 29. Oregon State University, 27 pp.
- Fairall, C. W., E. F. Bradley, J. S. Godfrey, G. A. Wick, J. B. Edson, and G. S. Young, 1996a. Cool-skin and warm-layer effects on sea surface temperature. *J. Geophys. Res.*, **101**, 1295-1308.
- , E. F. Bradley, D. P. Rogers, J. B. Edson, and G. S. Young, 1996b: Bulk parameterization of air-sea fluxes for Tropical Ocean-Global Atmosphere Coupled Ocean Atmosphere Response Experiment. *J. Geophys. Res.*, **101**, 3747-3764.

- Flament, P., and M. Sawyer, 1995: Observations of the effect of rain temperature on the surface heat flux in the intertropical convergence zone. *J. Phys. Oceanogr.*, **25**, 413-419.
- Gamache, J. F., and R. A. Houze, Jr., 1982: Mesoscale air motions associated with a tropical squall line. *Mon. Wea. Rev.*, **110**, 118-135.
- Garratt, J. R., 1992: *The Atmospheric Boundary Layer*, Cambridge Univ. Press, New York, 316 pp.
- Gautier, C., 1978: Some evidence of cool surface water pools associated with mesoscale downdrafts during GATE. *J. Phys. Oceanogr.*, **8**, 162-166.
- Gaynor, J. E., and C. F. Ropelewski, 1979: Analysis of the convectively modified GATE boundary layer using in situ and acoustic sounder data. *Mon. Wea. Rev.*, **107**, 985-993.
- Gent, P. R., 1991: The heat budget of the TOGA-COARE domain in an ocean model. *J. Geophys. Res.*, **96**, 3323-3330.
- Geotis, S. G., 1975: Some measurements of the attenuation of 5-cm radiation in rain. Preprints, *16th Conference on Radar Meteorology*, Houston, TX, Amer. Met. Soc., 63-66.
- Godfrey, J. S., and E. J. Lindstrom, 1989: On the heat budget of the equatorial west Pacific surface mixed layer. *J. Geophys. Res.*, **94**, 8007-8017.
- Gosnell, R., C. W. Fairall, and P. J. Webster, 1995: The sensible heat of rainfall in the tropical ocean. *J. Geophys. Res.*, **100**, 18 437-18 442.
- Hartmann, D. L., and M. L. Michelsen, 1993: Large-scale effects on the regulation of tropical sea surface temperature. *J. Climate*, **6**, 2049-2062.
- Hildebrand, P. H., 1978: Iterative correction for attenuation of 5 cm radar in rain. *J. Appl. Met.*, **17**, 508-514.
- Horel, J. D., and J. M. Wallace, 1981: Planetary scale atmospheric phenomena associated with the Southern Oscillation. *Mon. Wea. Rev.*, **109**, 813-829.
- Hoskins, B. M., H. H. Hsu, I. N. James, M. Masutani, P. D. Sardeshmukh, and G. H. White, 1989: Diagnostics of the Global Atmospheric Circulation Based on ECMWF Analyses, 1979-1989. WCRP-27, WMO/TD-No. 326, World Meteorological Organization, 217 pp.
- Hosom, D. S., R. A. Weller, R. E. Payne, and K. E. Prada, 1995: The IMET (Improved Meteorology) ship and buoy systems. *J. Atmos. Oceanic Tech.*, **12**, 527-540.

- Houze, R. A., Jr., 1977: Structure and dynamics of a tropical squall-line system. *Mon. Wea. Rev.*, **105**, 1540-1567.
- Jabouille, P., J. L. Redelsperger, and J. P. Lafore, 1996: Modification of surface fluxes by atmospheric convection in the TOGA COARE region. *Mon. Wea. Rev.*, **124**, 816-837.
- Johnson, R. H., and M. E. Nicholls, 1983: A composite analysis of the boundary layer accompanying a tropical squall line. *Mon. Wea. Rev.*, **111**, 308-319.
- Liu, W. T., K. B. Katsaros, and J. A. Businger, 1979: Bulk parameterization of air-sea exchanges of heat and water vapor including the molecular constraints at the interface. *J. Atmos. Sci.*, **36**, 1722-1735.
- Lukas, R., 1990a: Freshwater input to the western equatorial Pacific Ocean and air-sea interaction. *Air-Sea Interaction in the Tropical Western Pacific, Proc. Beijing, China, US-PRC Int. TOGA Symp.* China Ocean Press, 305-328.
- , 1990b: The role of salinity in the dynamics and thermodynamics of the western Pacific warm pool. Proceedings of the International TOGA Scientific Conference, 16-20 July 1990, Honolulu, Hawaii, WCRP-43, WMO/TD No. 379, pp. 73-81.
- , 1991: The diurnal cycle of sea surface temperature in the western equatorial Pacific. *TOGA Notes*, **2**, 1-5.
- , and E. Lindstrom, 1991: The mixed layer of the western equatorial Pacific Ocean. *J. Geophys. Res.*, **96**, 3343-3357.
- McPhaden, M. J., S. P. Hayes, L. J. Mangum, and J. Toole, 1990: Variability in the western equatorial Pacific during the 1986-87 El Niño/Southern Oscillation event. *J. Phys. Oceanogr.*, **20**, 190-208.
- , and S. P. Hayes, 1991: On the variability of winds, sea surface temperature, and surface layer heat content in the western equatorial Pacific. *J. Geophys. Res.*, **96**, 3331-3342.
- Miller, J. R., 1976: The salinity effect in a mixed layer ocean model. *J. Phys. Oceanogr.*, **6**, 29-35.
- Patterson, V. L., M. D. Hudlow, P. J. Pytlowany, F. P. Richards, and J. D. Hoff, 1979: Gate radar rainfall processing system. NOAA Technical Memorandum EDIS 26, Washington, D.C.

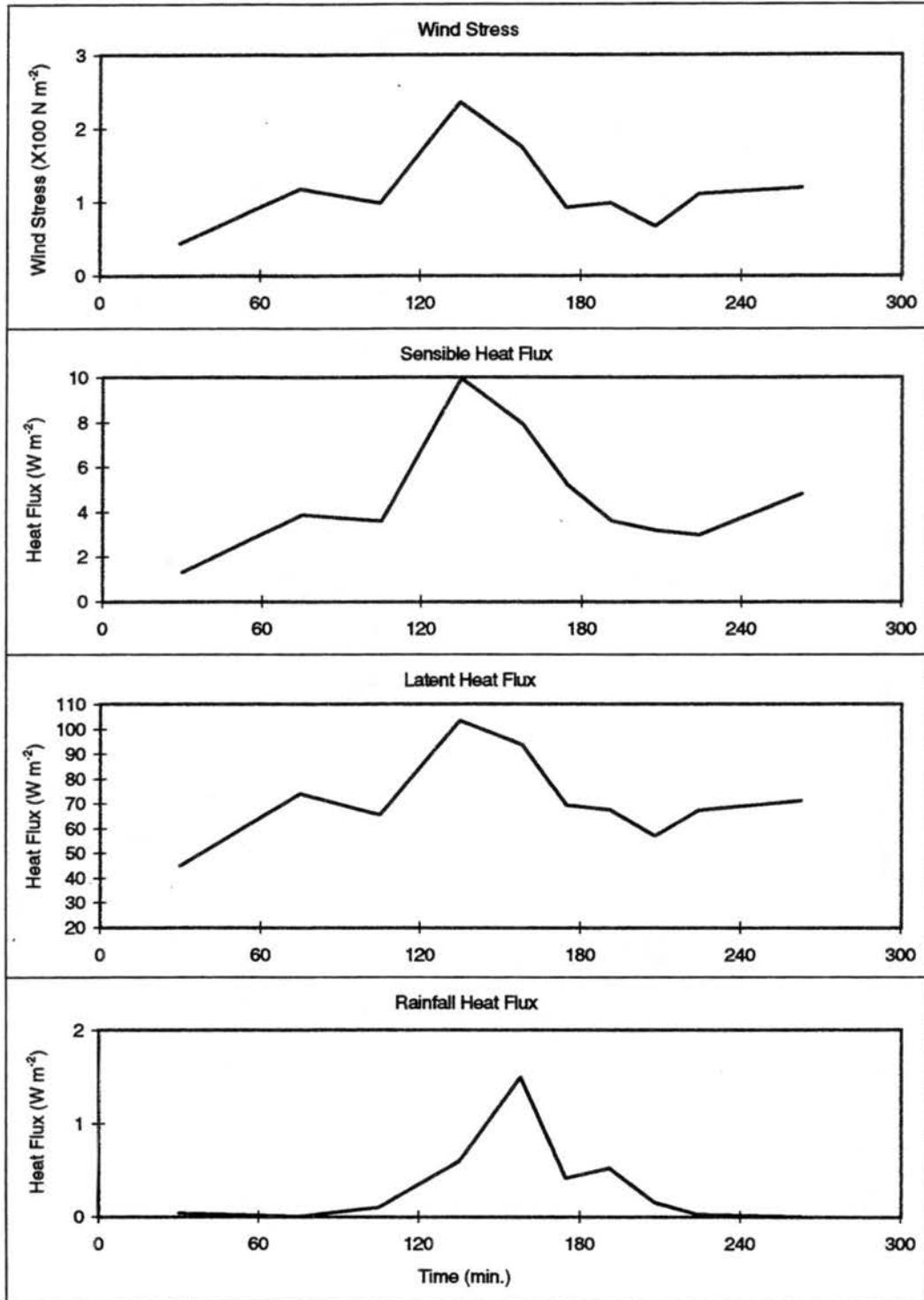
- Philander, S. G., 1990: *El Niño, La Niña, and the Southern Oscillation.*, Academic Press, 293 pp.
- Price, J., F., 1979: Observations of a rain-formed mixed layer. *J. Phys. Oceanogr.*, **9**, 643-649.
- , R. A. Weller, and R. Pinkel, 1986: Diurnal cycling: Observations and models of the upper ocean response to diurnal heating, cooling, and wind mixing. *J. Geophys. Res.*, **91**, 8411-8427.
- Rasmusson, E. M., and J. M. Wallace, 1983: Meteorological aspects of the El Niño/Southern Oscillation. *Science*, **222**, 1195-1202.
- Reed, R. K., 1985: An estimate of the climatological heat fluxes over the tropical Pacific Ocean. *J. Climate Appl. Meteor.*, **24**, 833-840.
- Rickenbach, T. M., and S. A. Rutledge, 1996: Convection in TOGA COARE: Horizontal scale, morphology, and rainfall production. *J. Atmos. Sci.*, submitted.
- Rotunno, R., J. B. Klemp, and M. L. Weismann, 1988: A theory for strong, long-lived squall lines. *J. Atmos. Sci.*, **45**, 463-484.
- Rutledge, S. A., R. Cifelli, C. DeMott, W. Peterson, T. Rickenbach, J. Lutz, R. Bowie, M. Strong, and E. Williams, 1993: The shipboard deployment of the MIT C-band radar during TOGA COARE. Preprints, *26th AMS International Conference on Radar Meteorology*, Norman, OK, Amer. Meteor. Soc., 371-373.
- Saunders, P. M., 1967: The temperature at the ocean-air interface. *J. Atmos. Sci.*, **24**, 269-273.
- Schumann, U., 1988: Minimum friction velocity and heat transfer in the rough surface layer of a convective boundary layer. *Bound.-Layer Meteor.*, **44**, 311-326.
- Steiner, M., and R. A. Houze, 1993: Three-dimensional validation at TRMM ground truth sites: Some early results from Darwin, Australia. Preprints, *26th International Conference on Radar Meteorology*, Norman, OK, Amer. Meteor. Soc., 417-420.
- , R. A. Houze, and S. E. Yuter, 1995: Climatological characteristics of three-dimensional storm structure from operational radar and raingauge data. *J. Appl. Meteor.*, **34**, 1978-2007.
- Sui, C. H., and K. M. Lau, 1992: Multiscale phenomena in the tropical atmosphere over the western Pacific. *Mon. Wea. Rev.*, **120**, 407-430.

- Sykes, R. I., D. S. Henn, and W. S. Lewellen, 1993: Surface-layer description under free convective conditions. *Quart. J. Roy. Meteor. Soc.*, **118**, 363-374.
- Taylor, R., 1973: *An Atlas of Pacific Rainfall*. Hawaii Institute of Geophysics Rep. HIG-73-9, 7 pp.
- Tokay, A., and D. A. Short, 1996: Evidence from tropical raindrop spectra of the origin of rain from stratiform versus convective clouds. *J. Appl. Meteor.*, **35**, 355-371.
- Tomczak, M., 1995: Salinity variability in the surface layer of the tropical western Pacific Ocean. *J. Geophys. Res.*, **100**, 20 499-20 515.
- Weare, B. C., P. T. Strub, and M. D. Samuel, 1981: Annual mean surface heat fluxes in the tropical Pacific Ocean. *Mon. Wea. Rev.*, **115**, 2687-2698.
- Webster, P. J., and R. Lukas, 1992: TOGA COARE: The Coupled Ocean-Atmosphere Response Experiment. *Bull. Amer. Meteor. Soc.*, **73**, 1377-1416.
- Weller, R. A., and S. P. Anderson, 1996: Surface meteorology and air-sea fluxes in the western equatorial Pacific warm pool during the TOGA Coupled Ocean-Atmosphere Response Experiment. *J. Climate*, **9**, 1959-1990.
- World Climate Research Program, 1990: Scientific plan for the TOGA Coupled Ocean-Atmosphere Response Experiment. *World Clim. Res. Program Publ. Ser.*, WMO/TD-64, 3, addendum, World Meteorol. Organ., Geneva, 105 pp.
- Young, G. S., S. M. Perugini, and C. W. Fairall, 1995: Convective wakes in the equatorial western Pacific during TOGA. *Mon. Wea. Rev.*, **123**, 110-123.
- Zipser, E. J., 1969: The role of organized unsaturated convective downdrafts in the structure and rapid decay of an equatorial disturbance. *J. Appl. Meteor.*, **8**, 799-814.
- , 1977: Mesoscale and convective-scale downdrafts as distinct components of squall line structure. *Mon. Wea. Rev.*, **105**, 1568-1589.

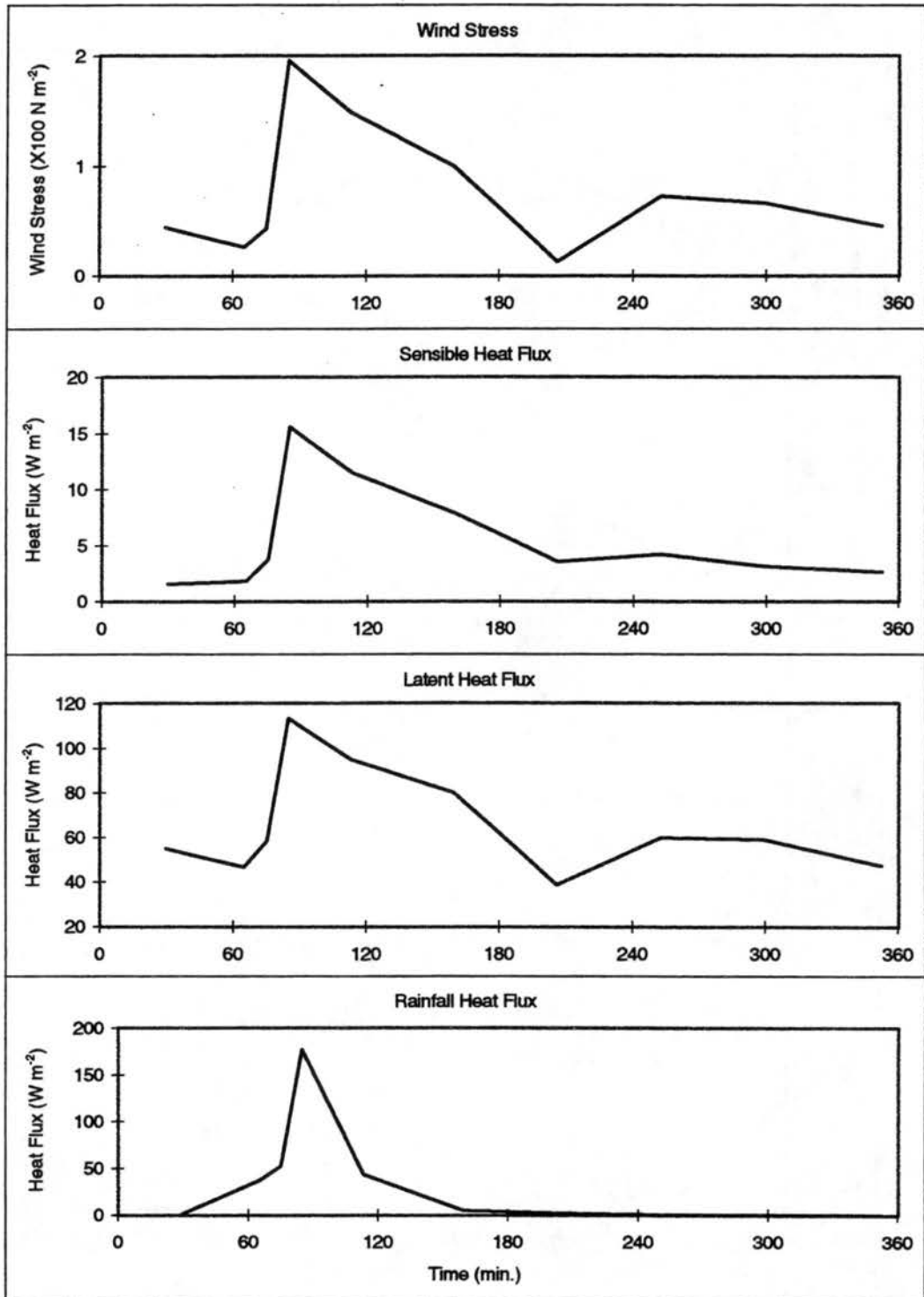
APPENDIX A

INDIVIDUAL SUB-MCS SCALE NON-LINEAR EVENTS

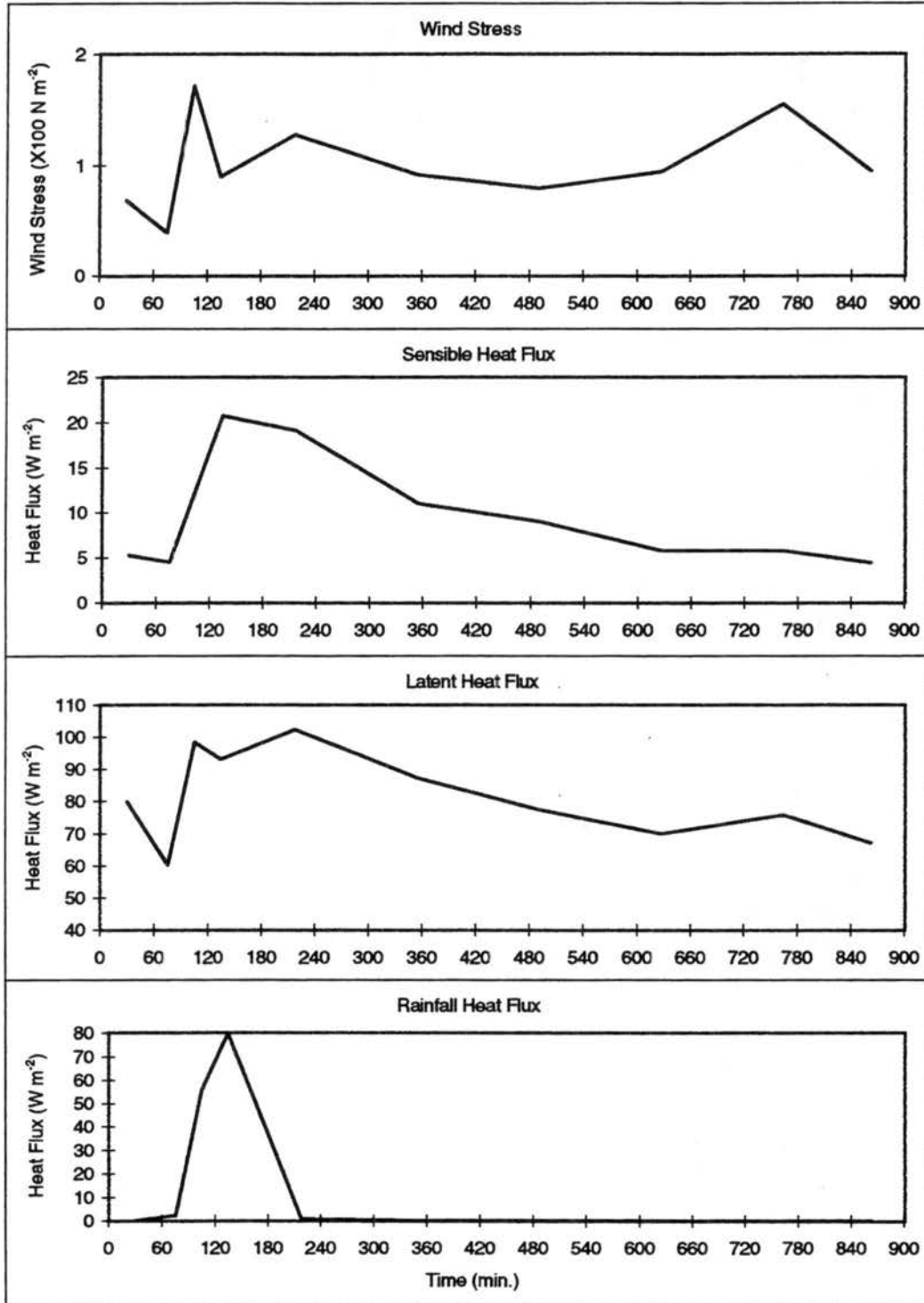
19 November 1992



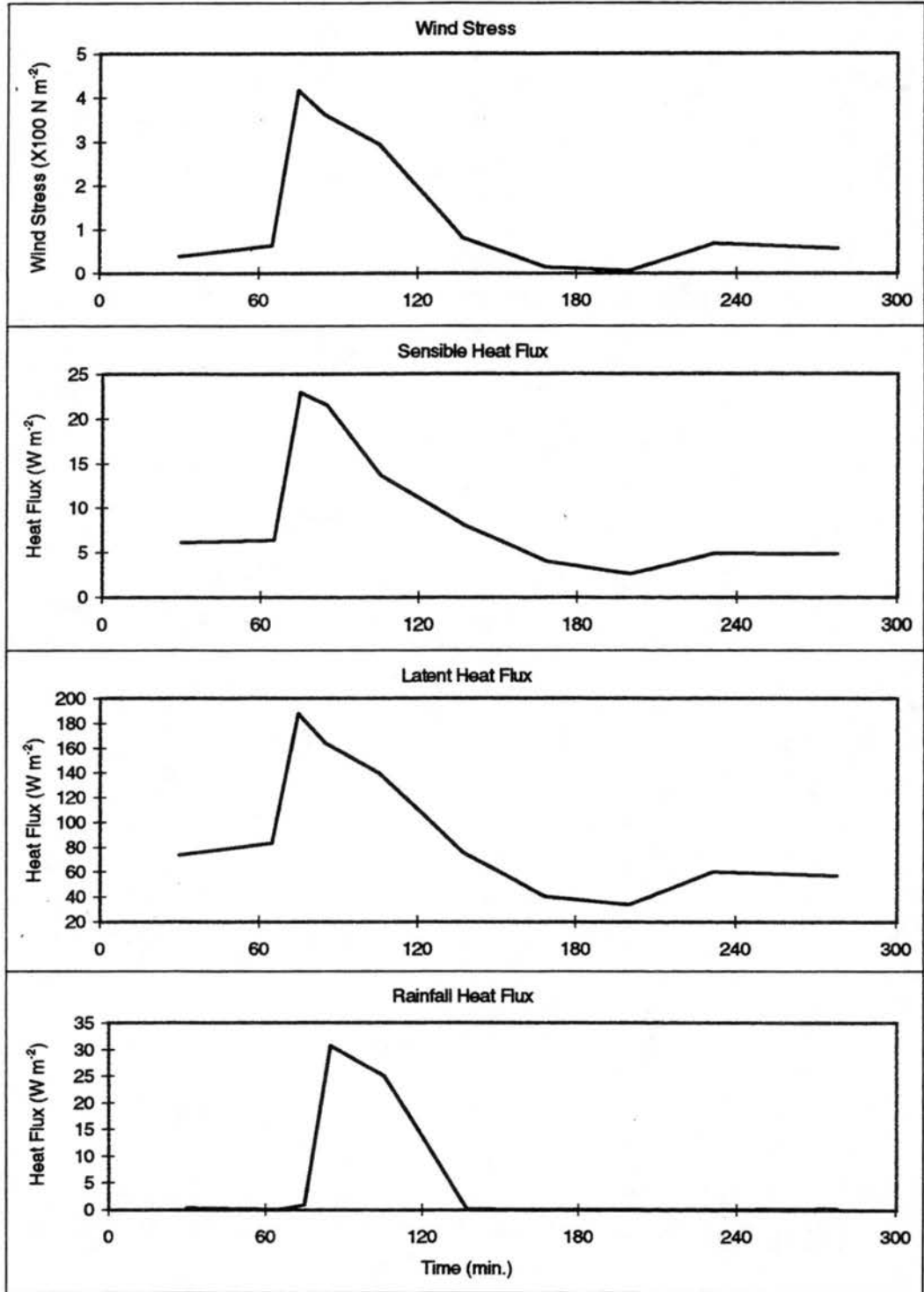
21 November 1992



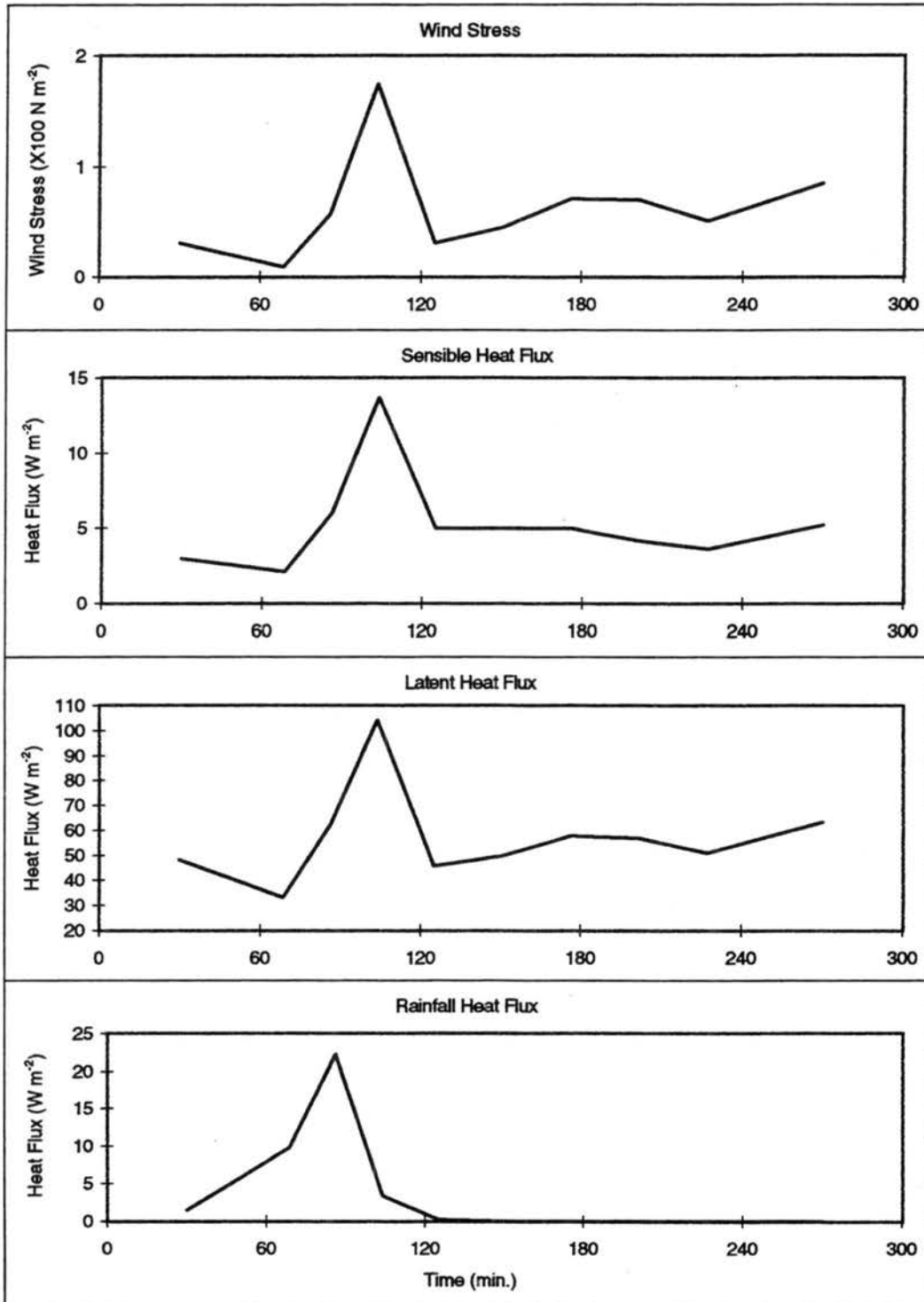
29 November 1992



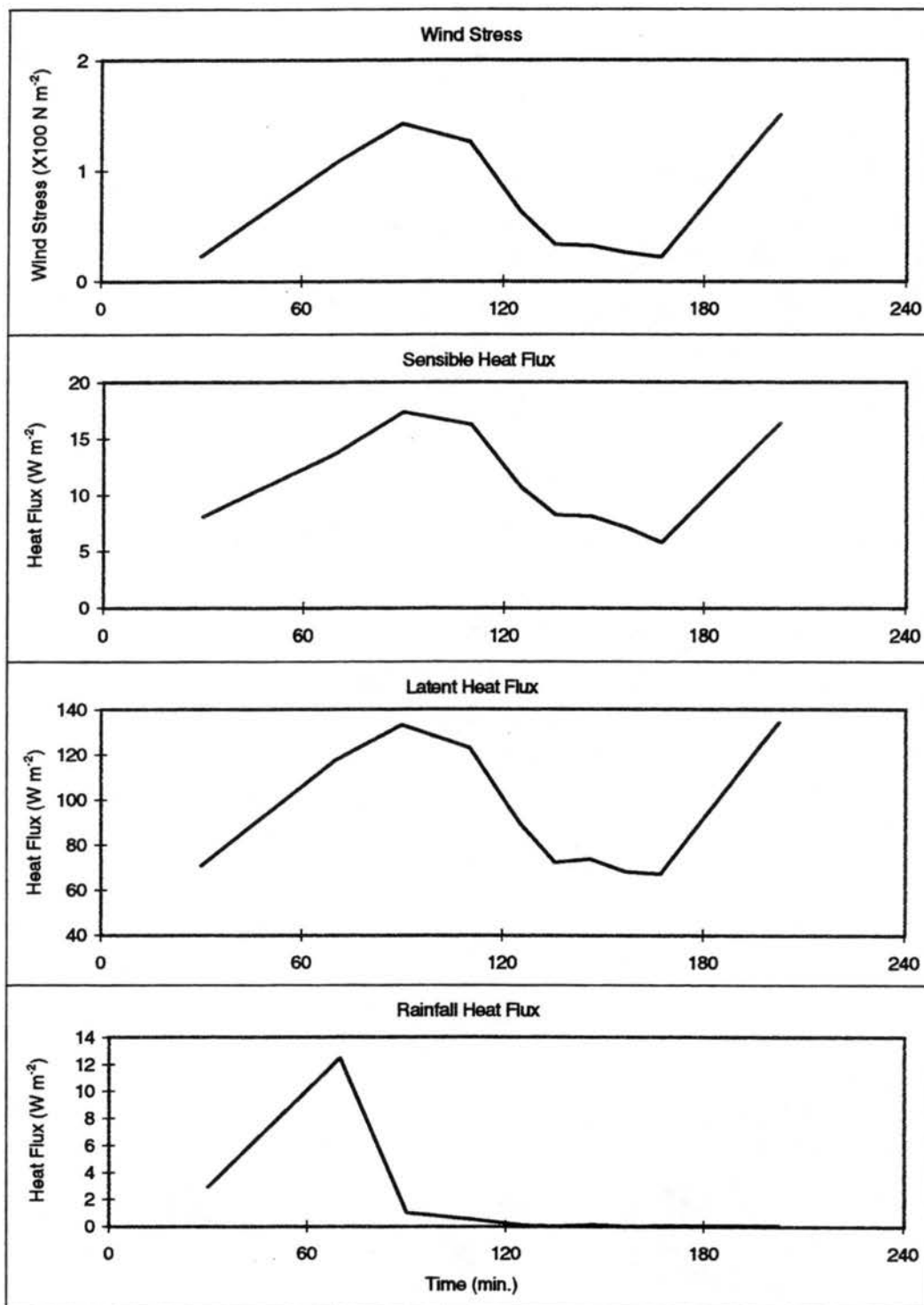
02 December 1992



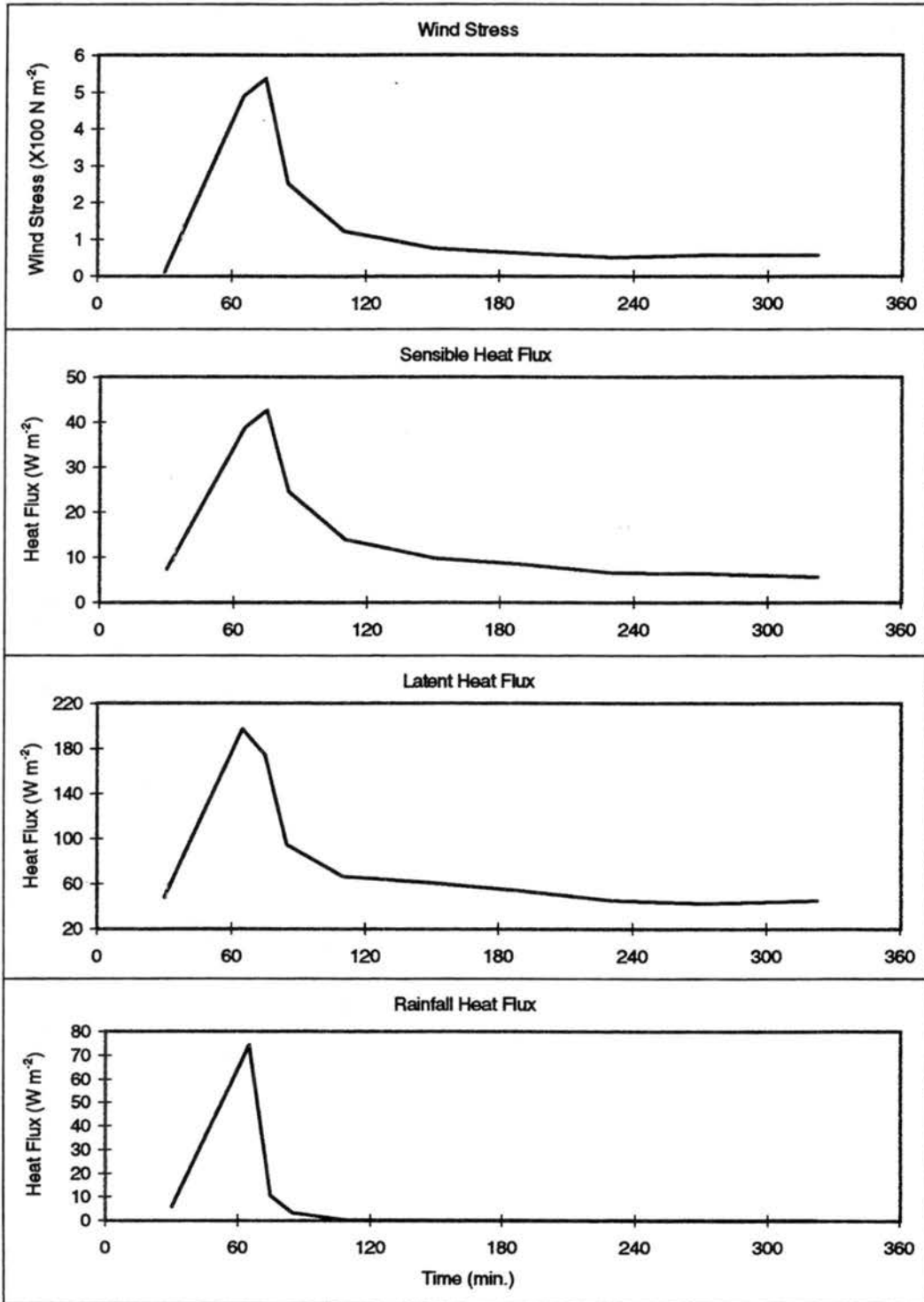
03 December 1992



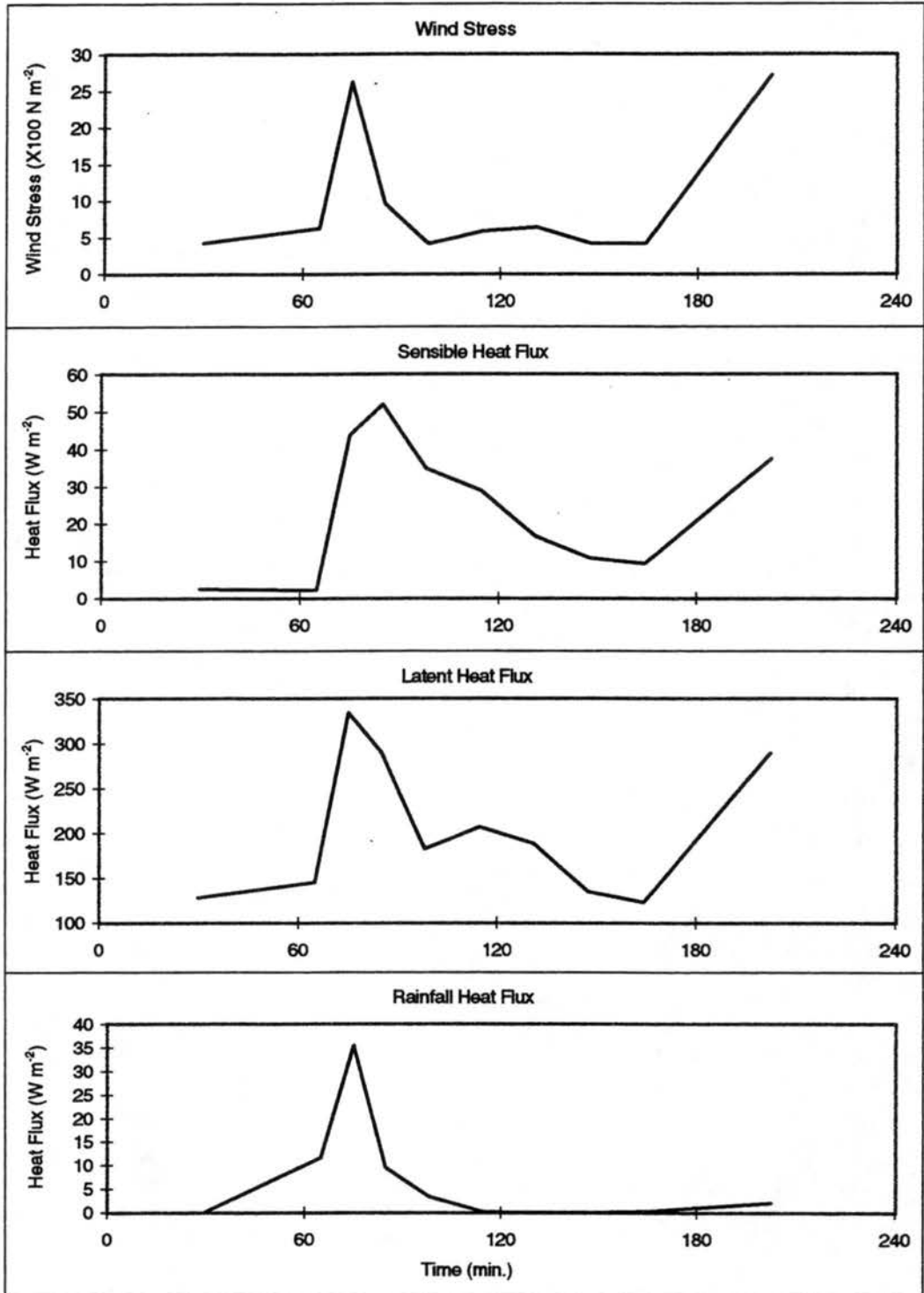
04 December 1992



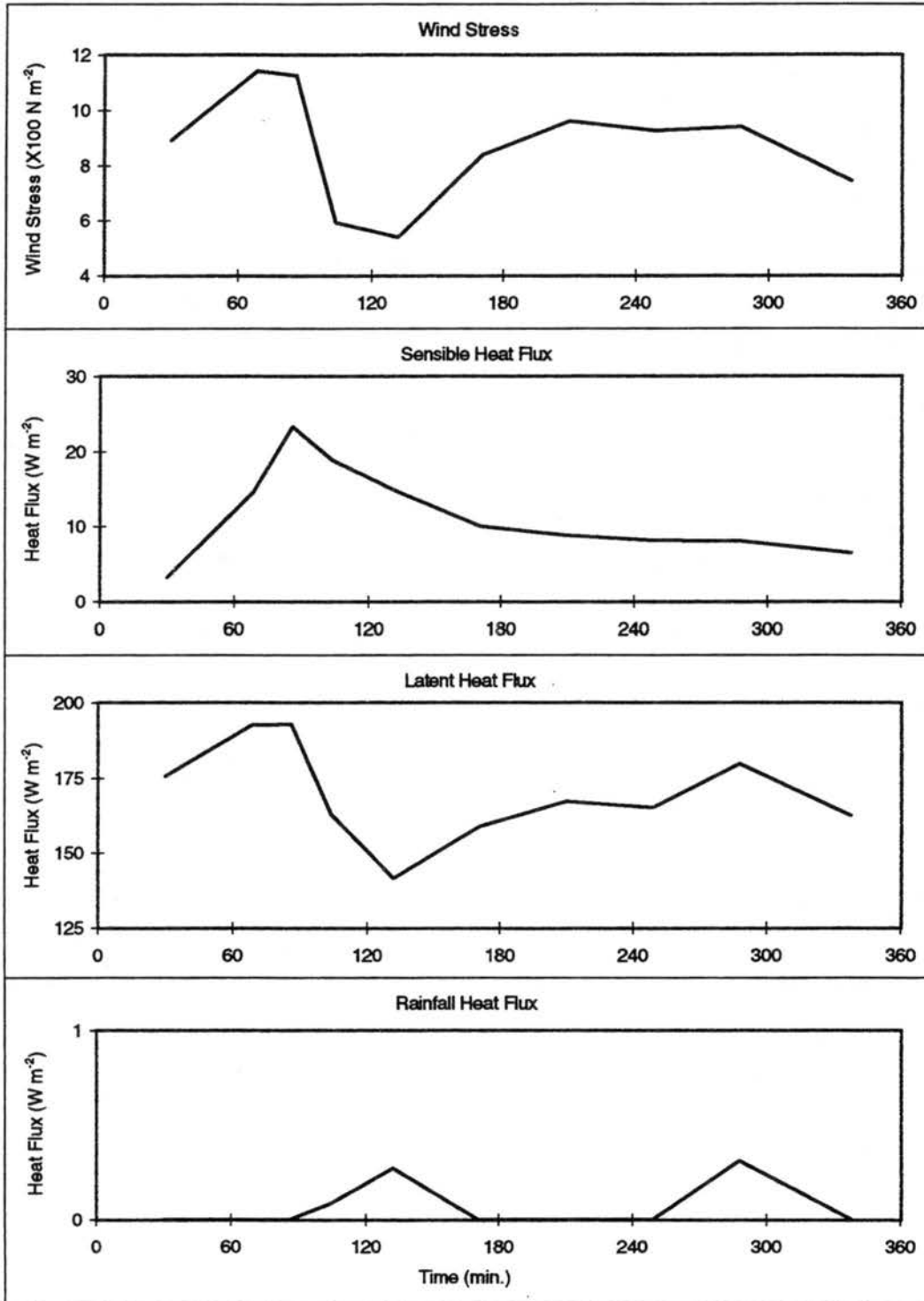
08 January 1993



30 January 1993



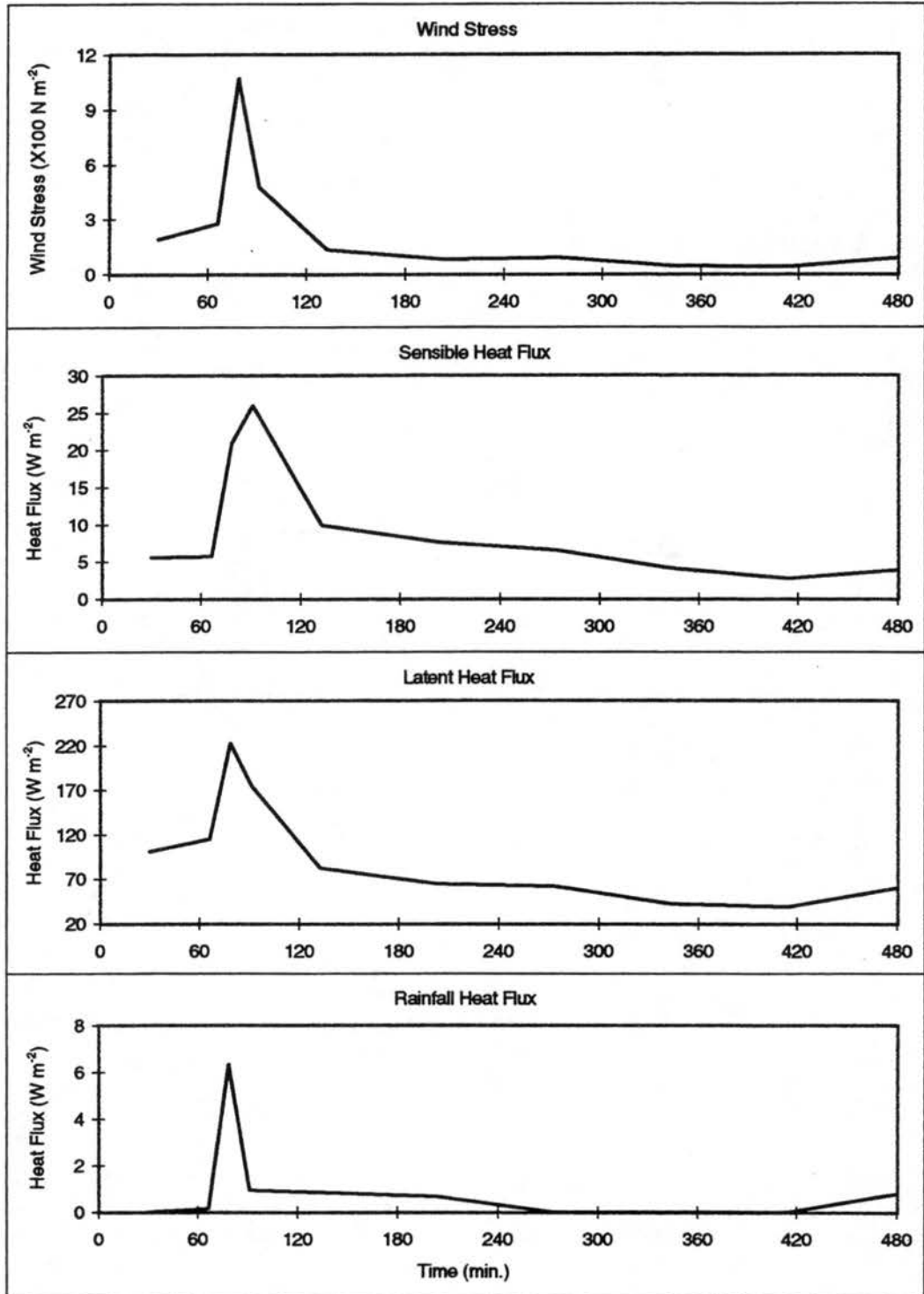
11 February 1993



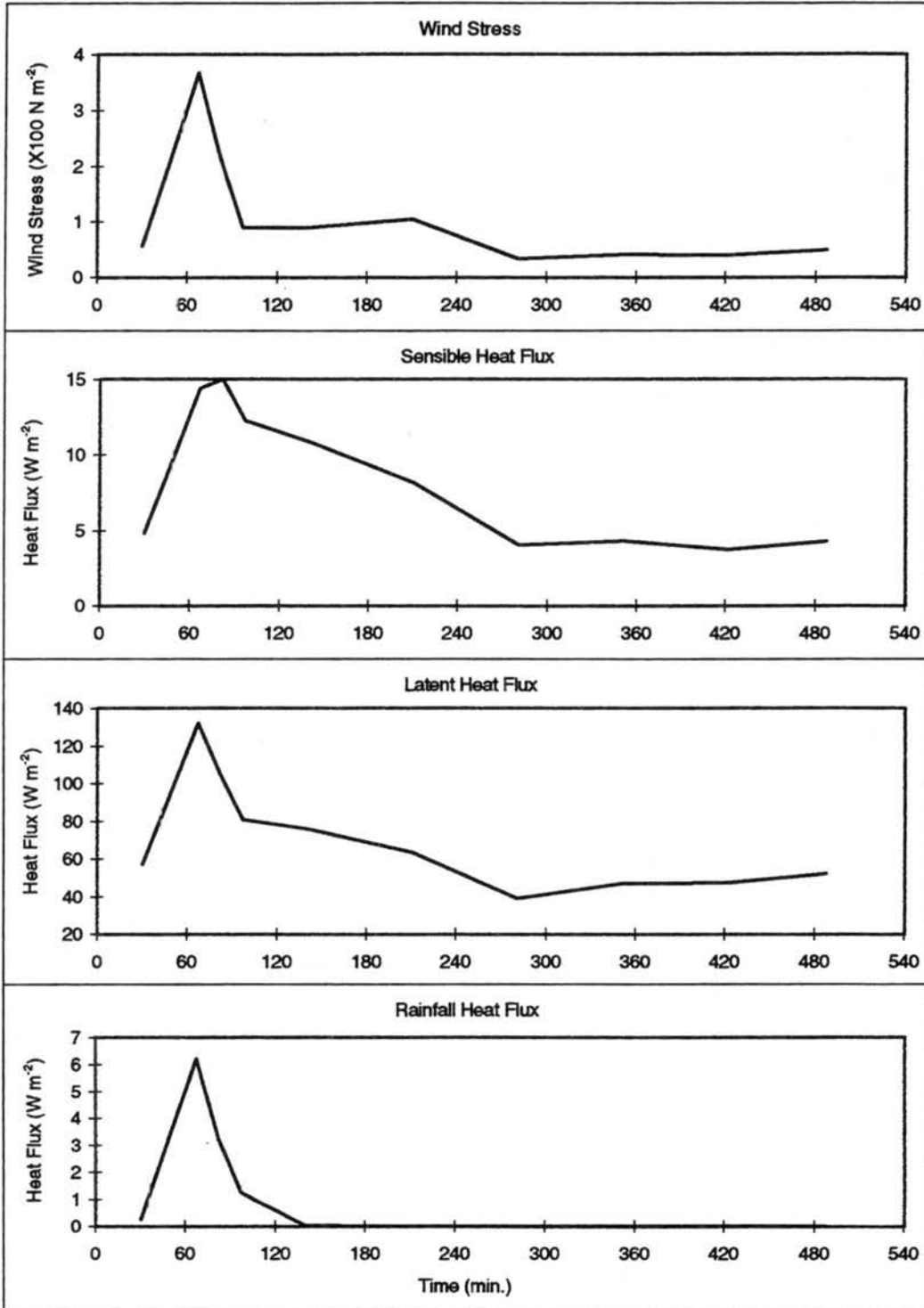
APPENDIX B

INDIVIDUAL SUB-MCS SCALE LINEAR EVENTS

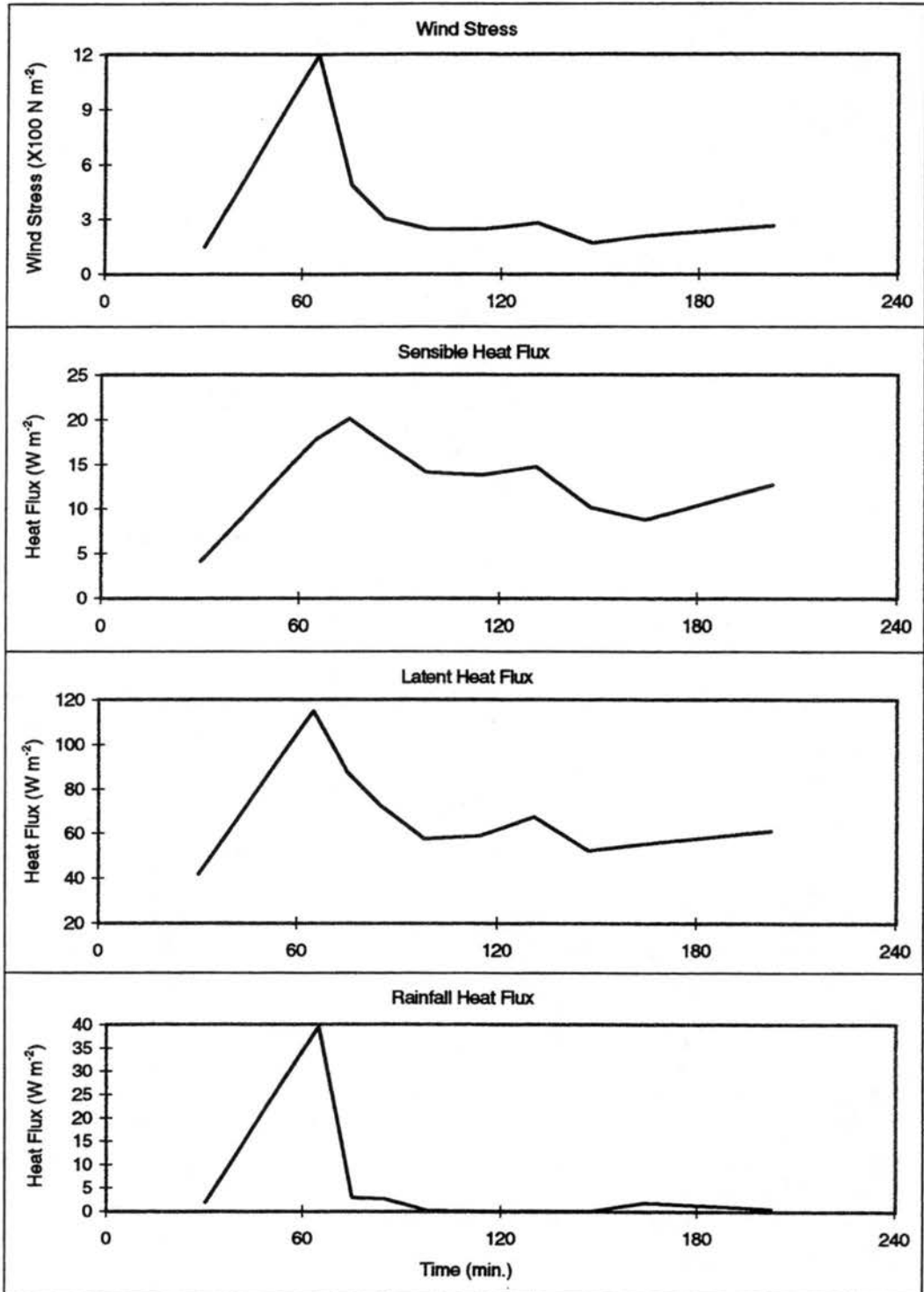
24 November 1992



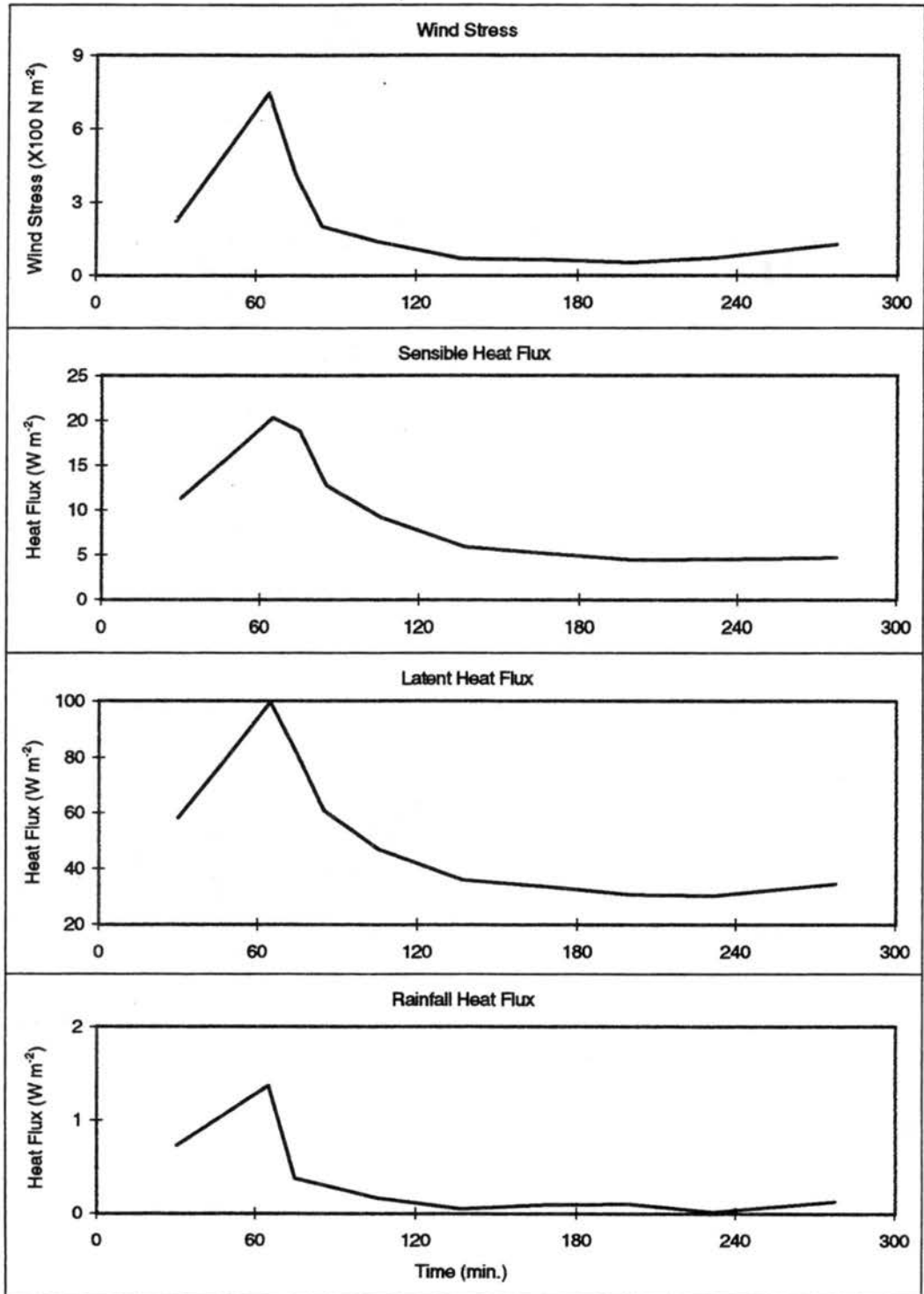
02 December 1992



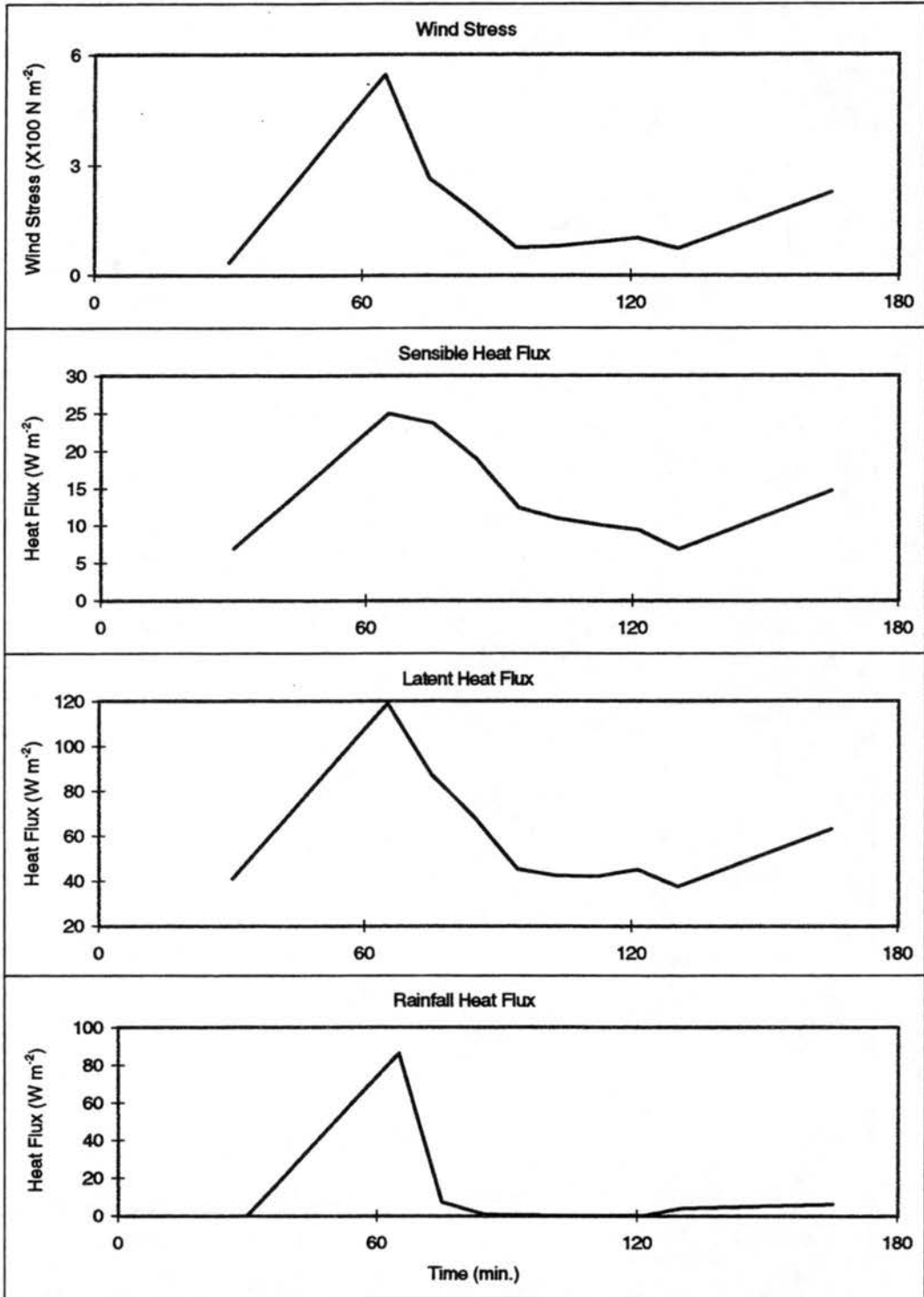
27 December 1992 (Case 1)



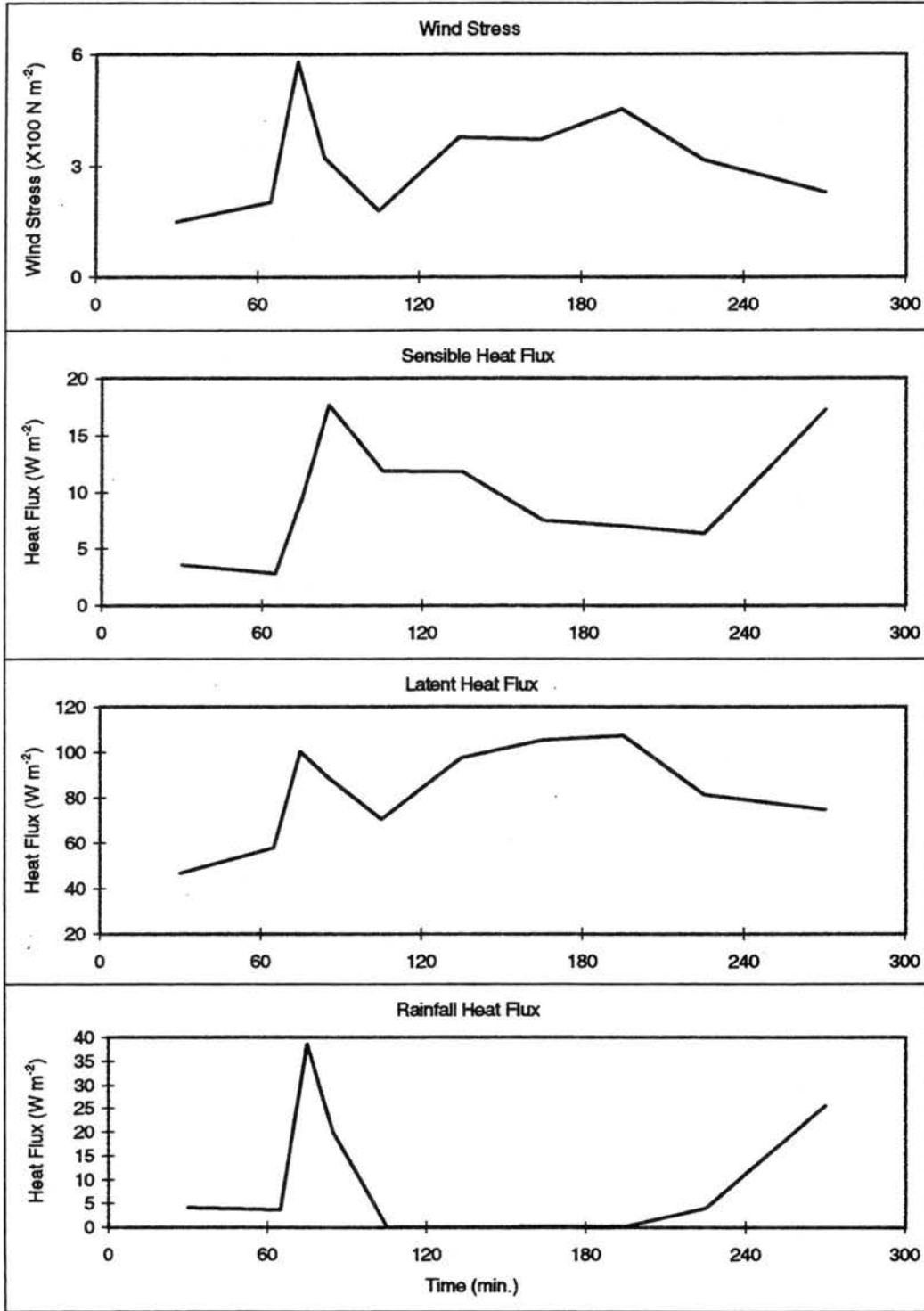
27 December 1992 (Case 2)



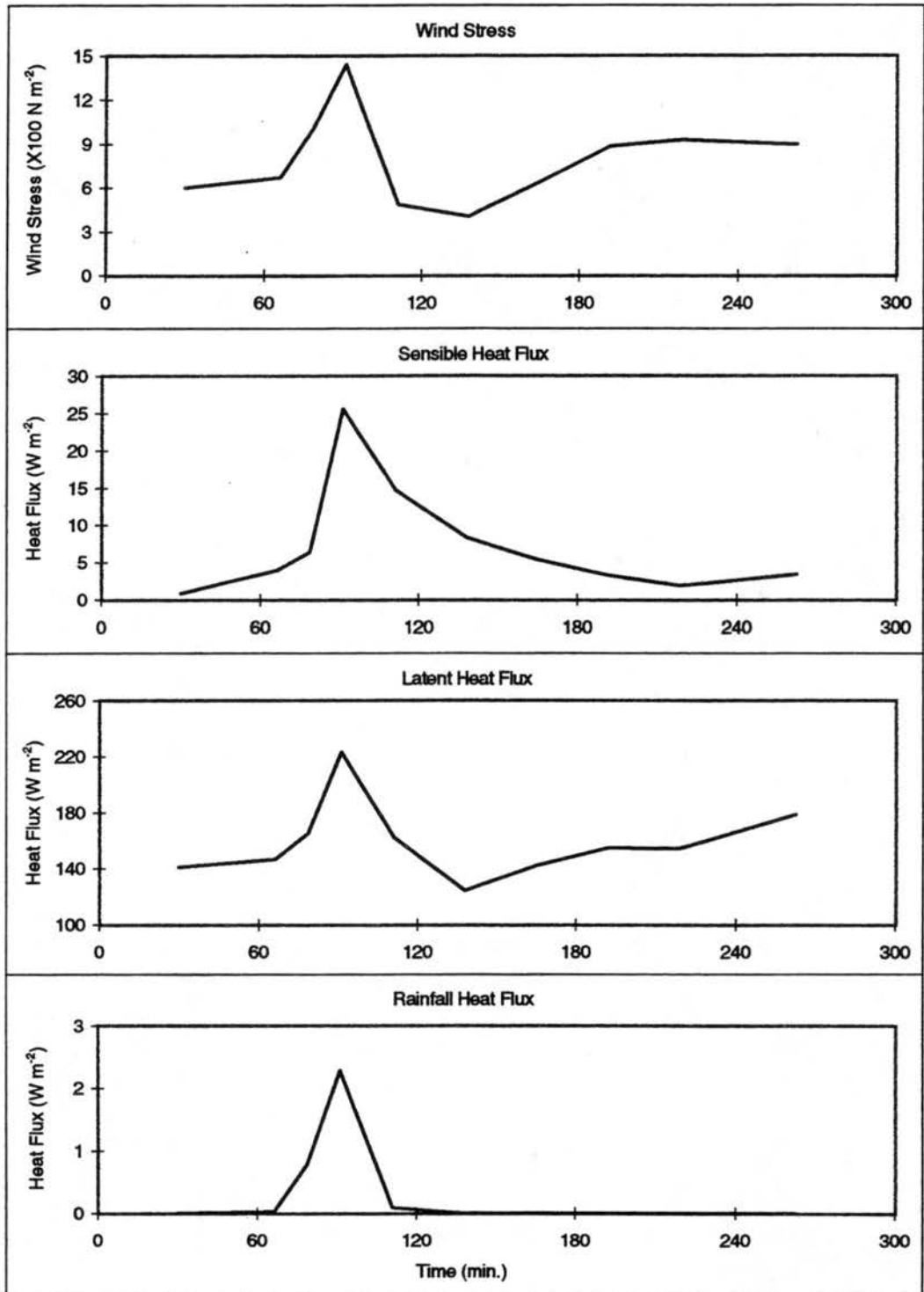
04 January 1993 (Case 1)



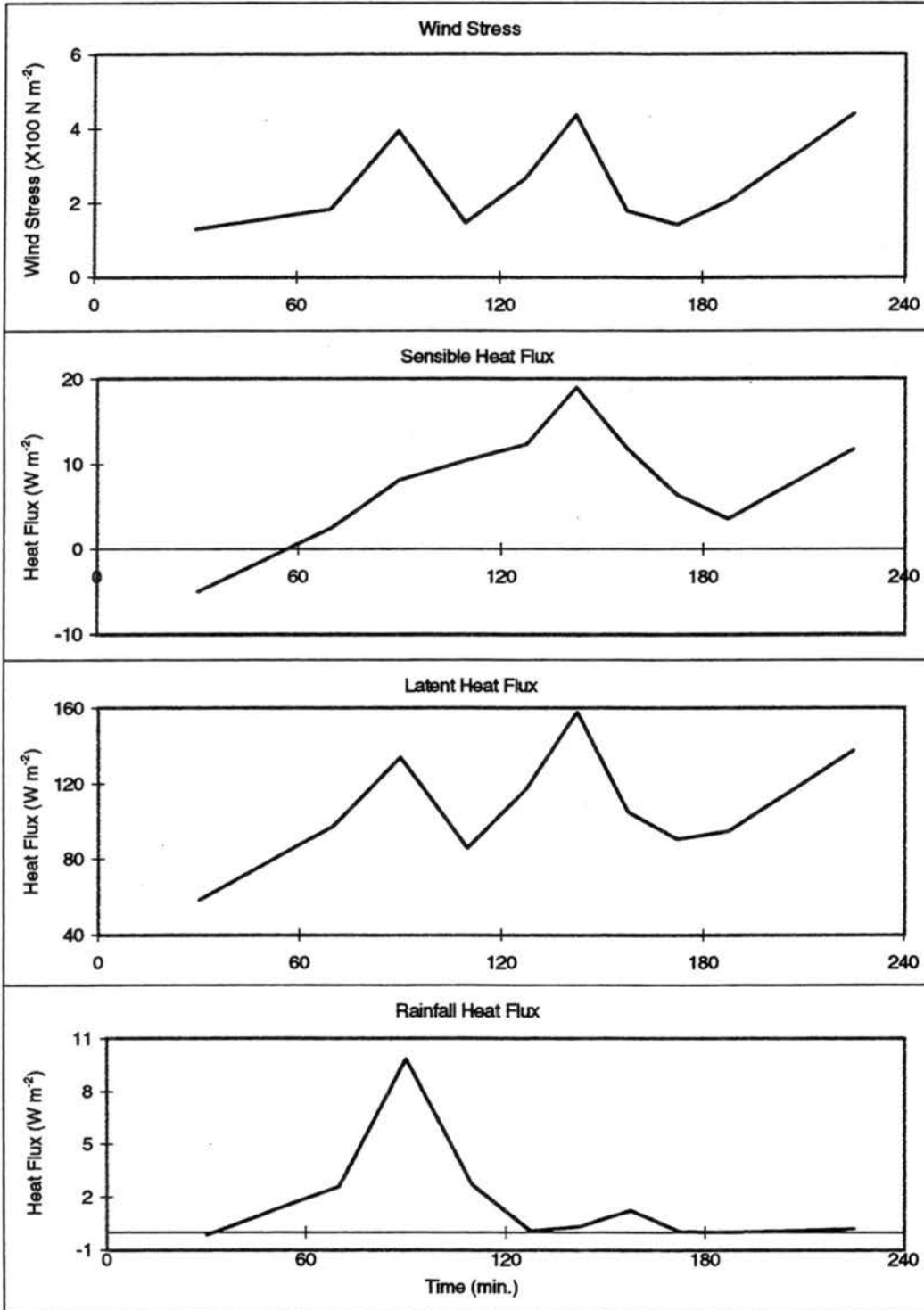
04 January 1993 (Case 2)



10 February 1993



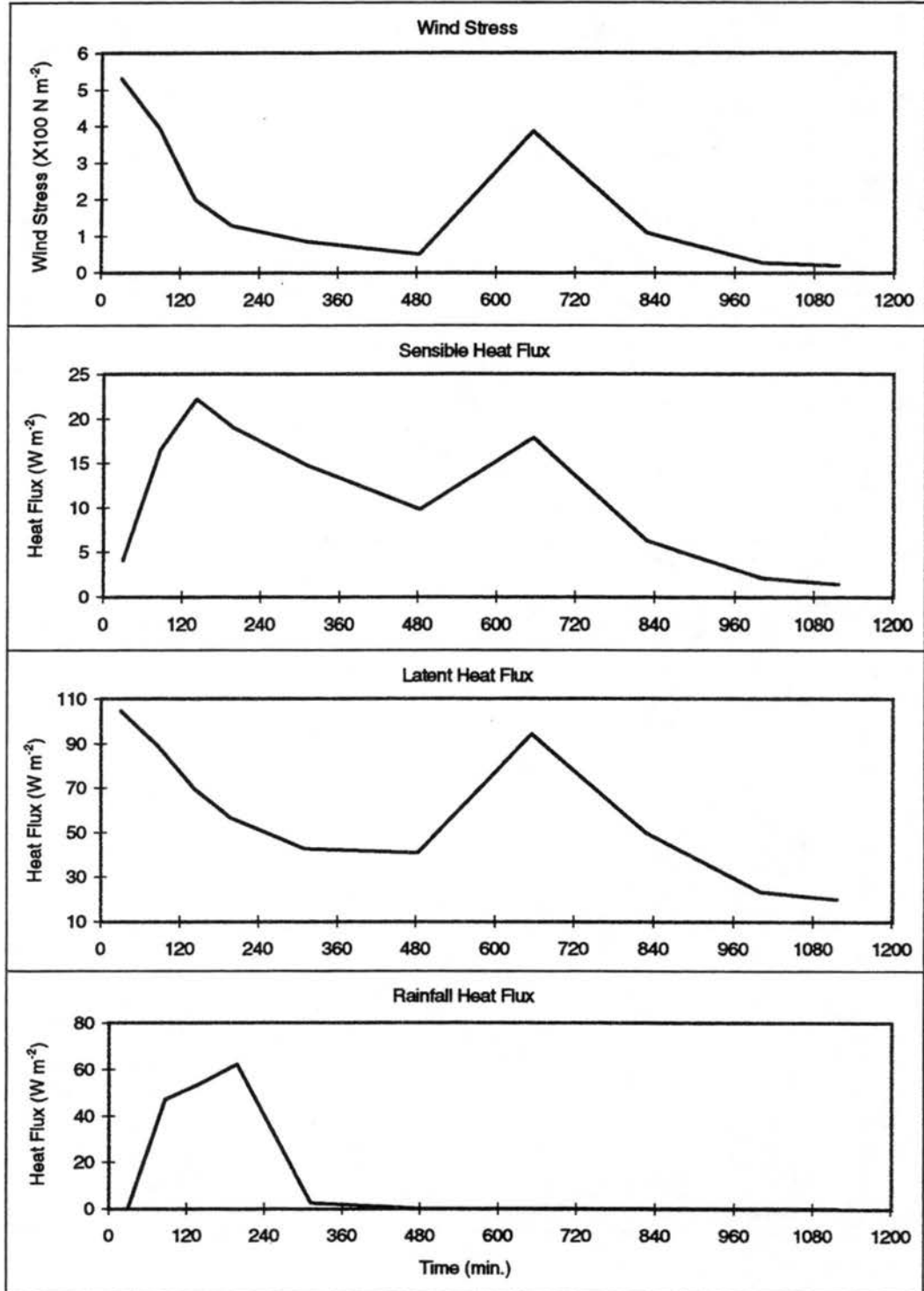
17 February 1993



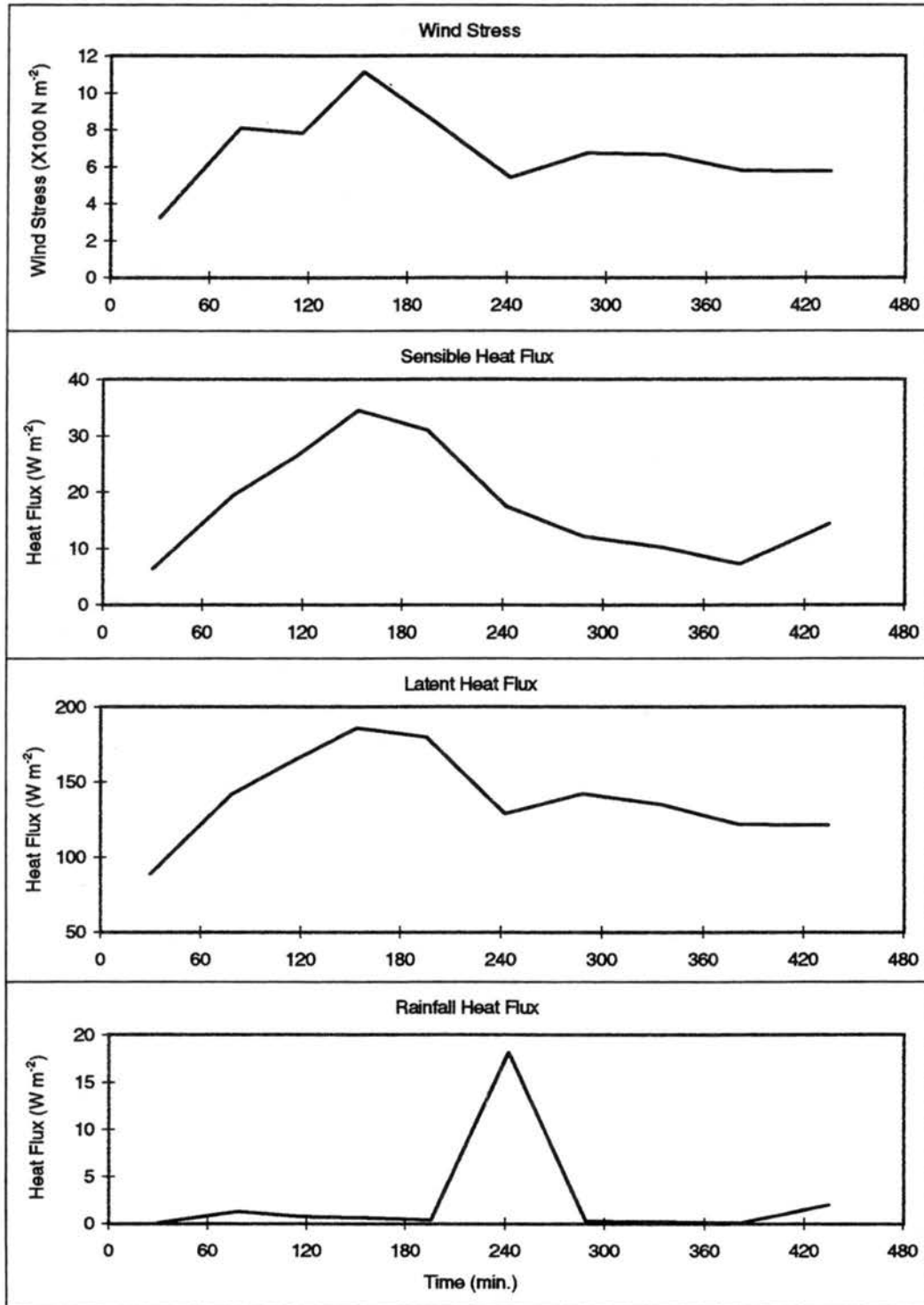
APPENDIX C

INDIVIDUAL MCS SCALE NON-LINEAR EVENTS

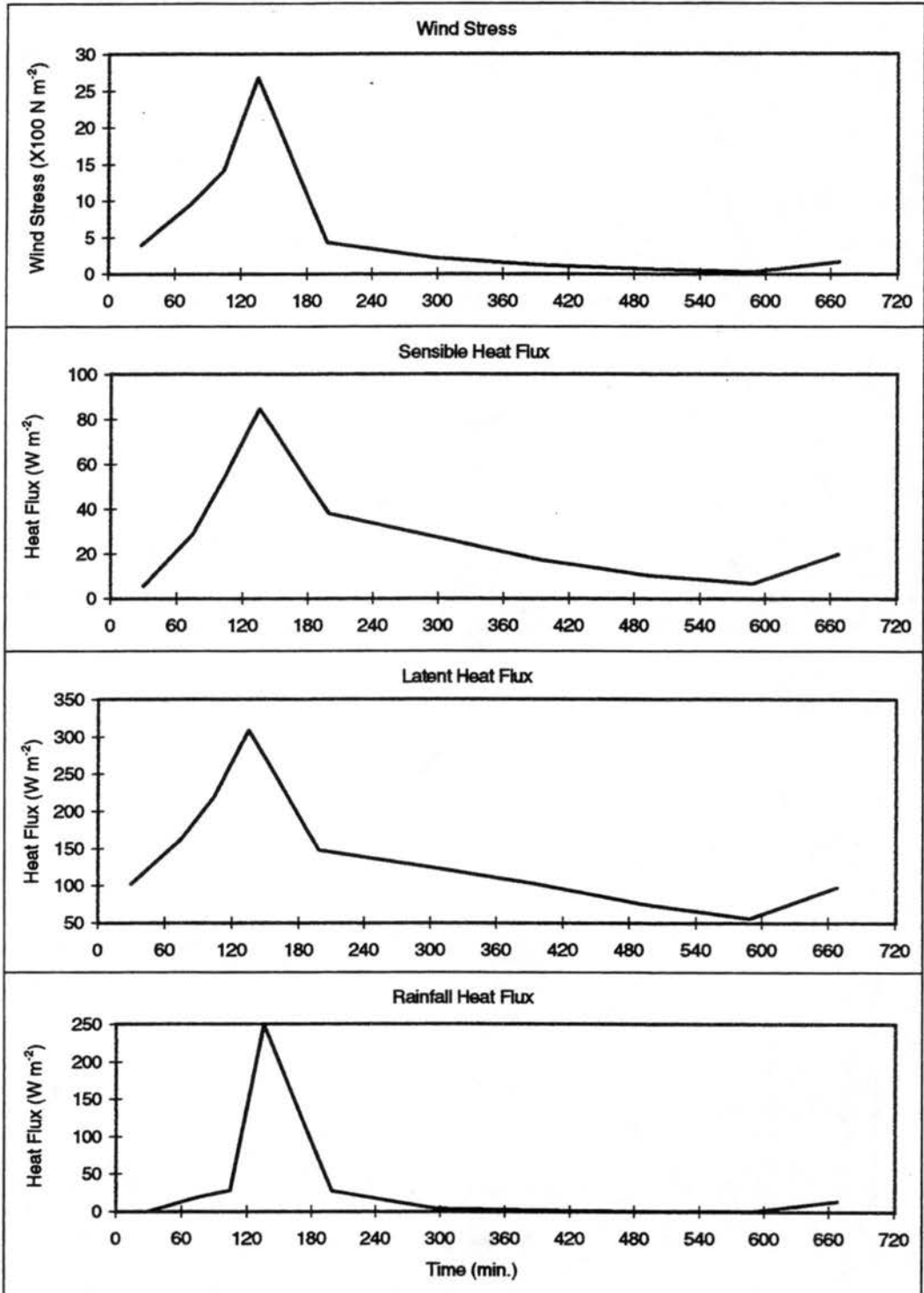
04 January 1993



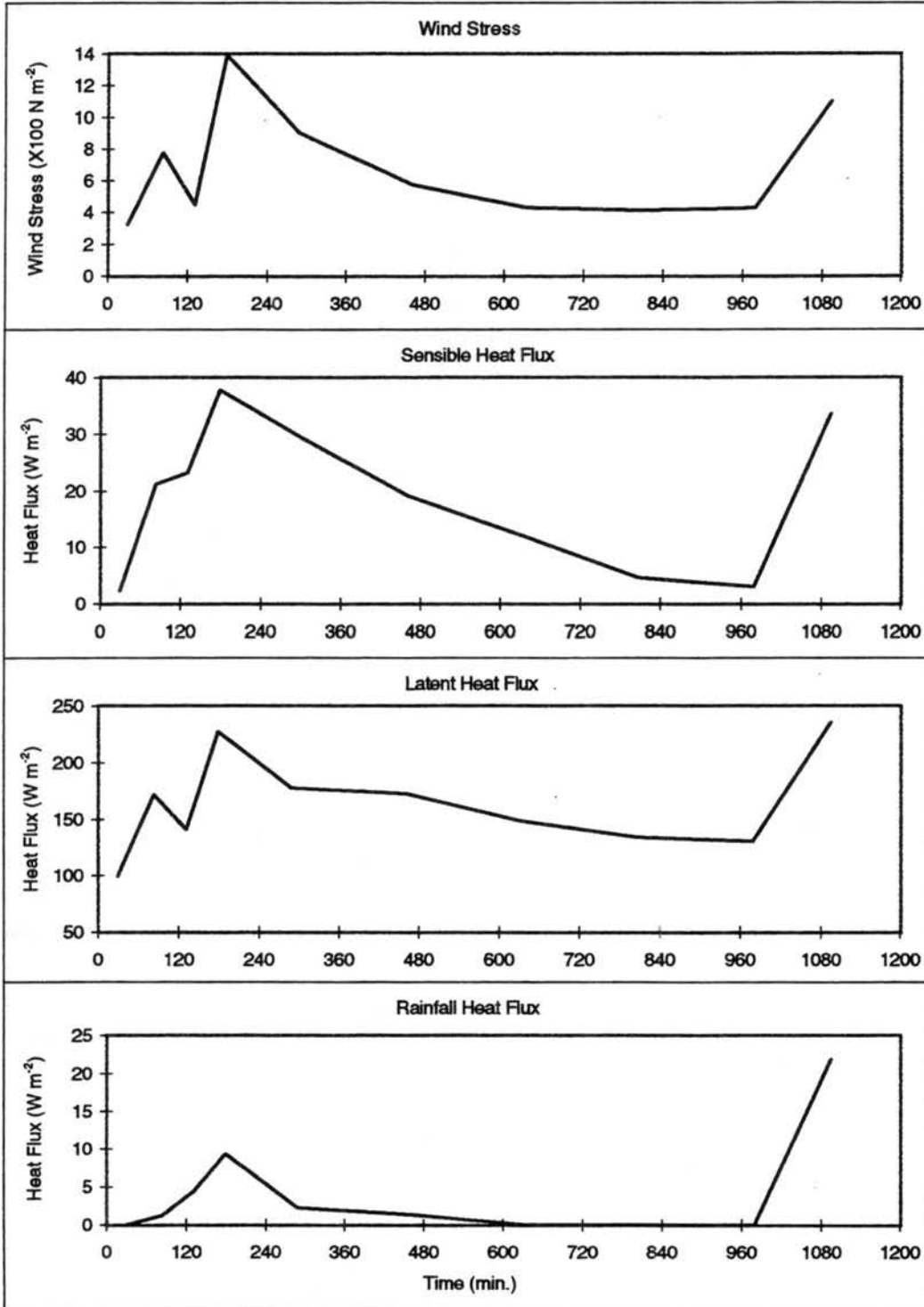
17 January 1993 (Case 1)



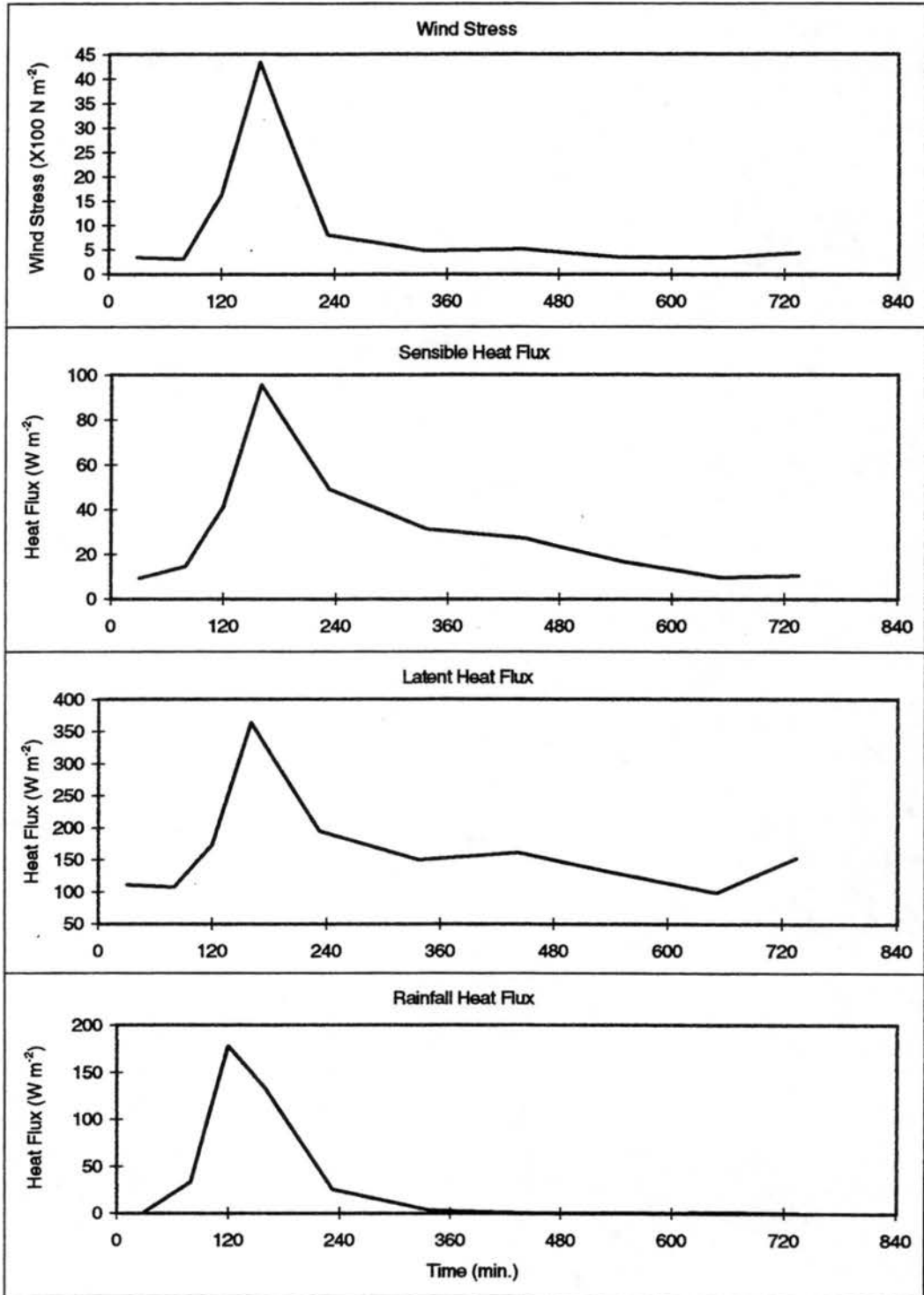
17 January 1993 (Case 2)



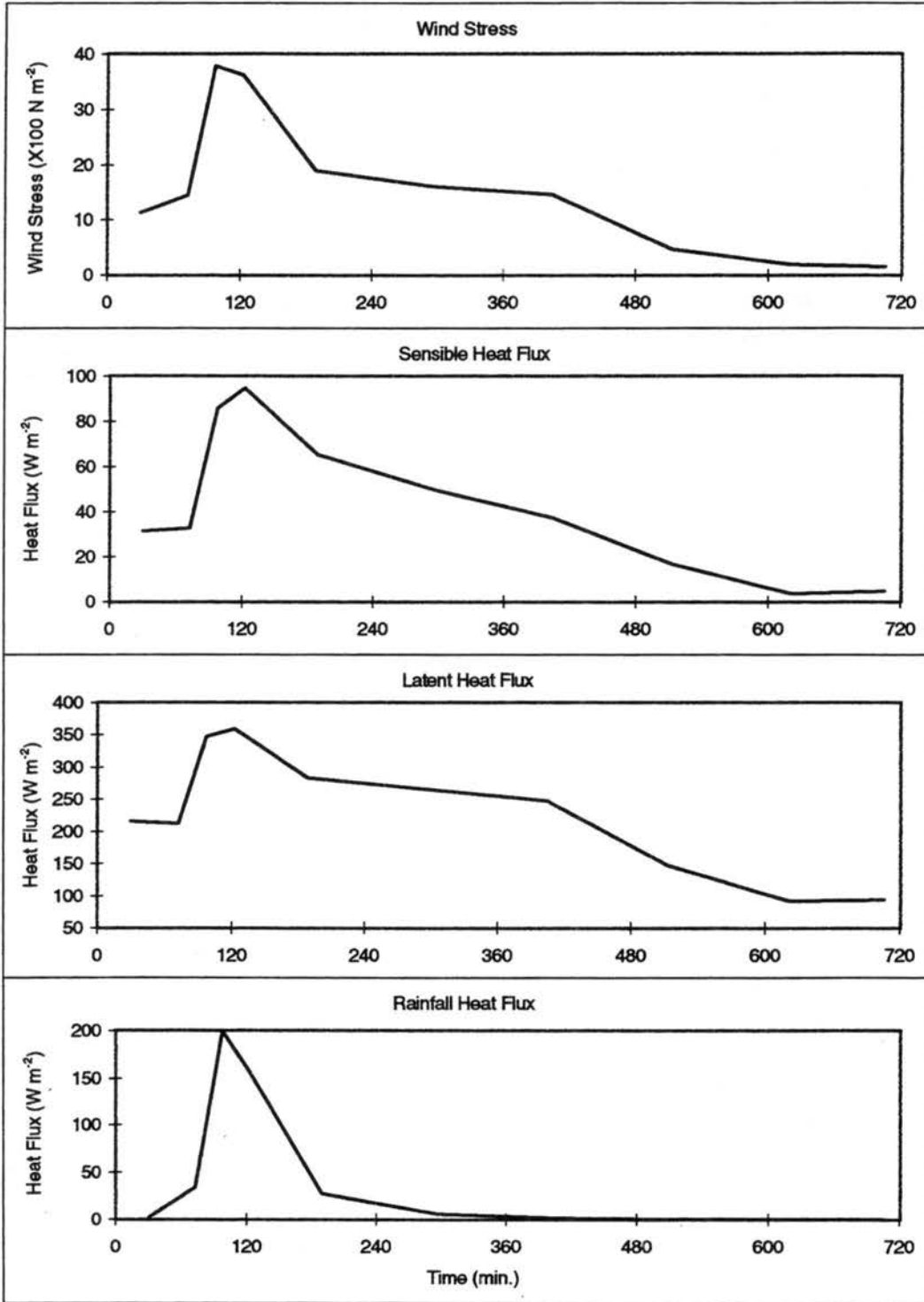
29 January 1993



11 February 1993



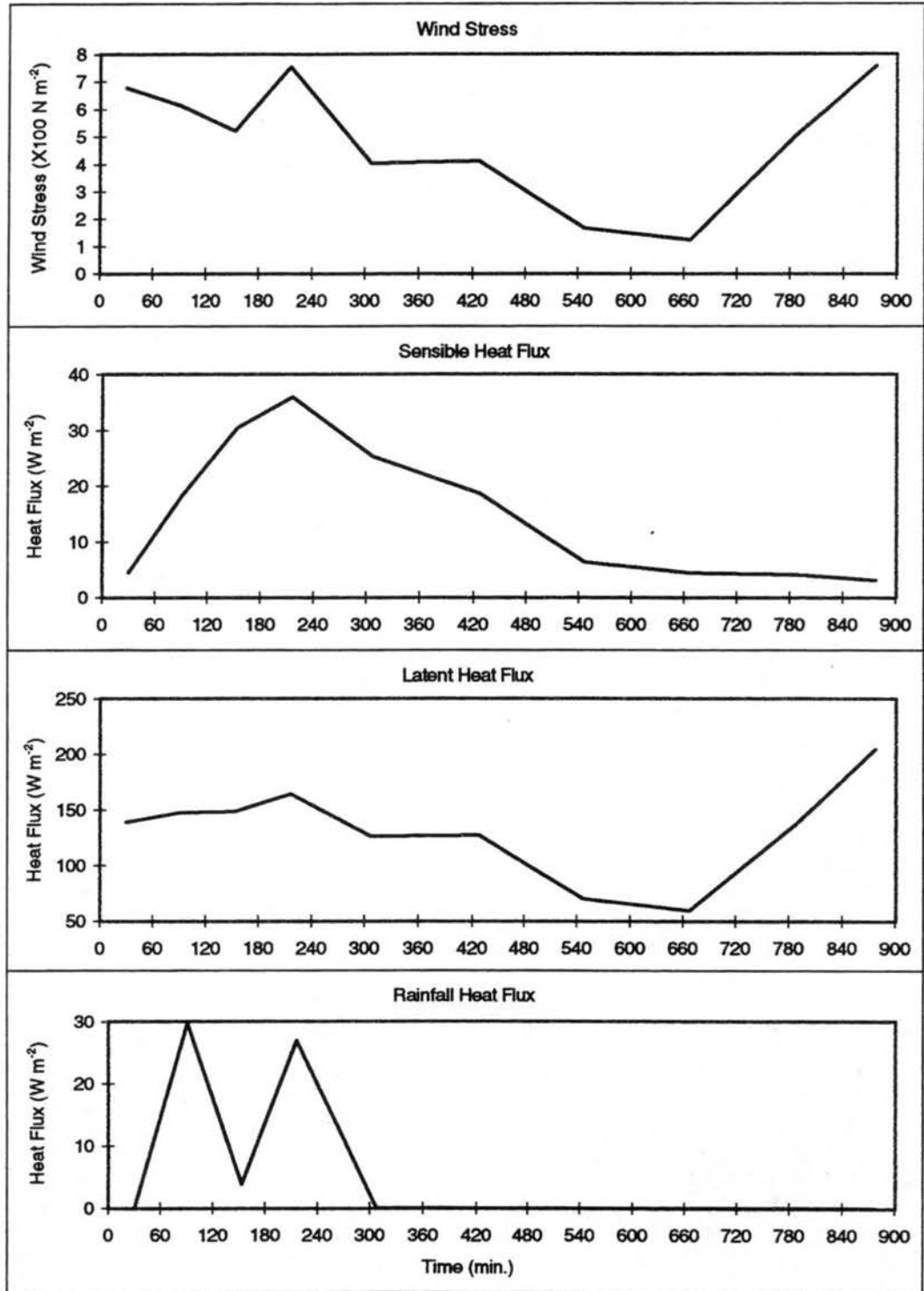
19 February 1993



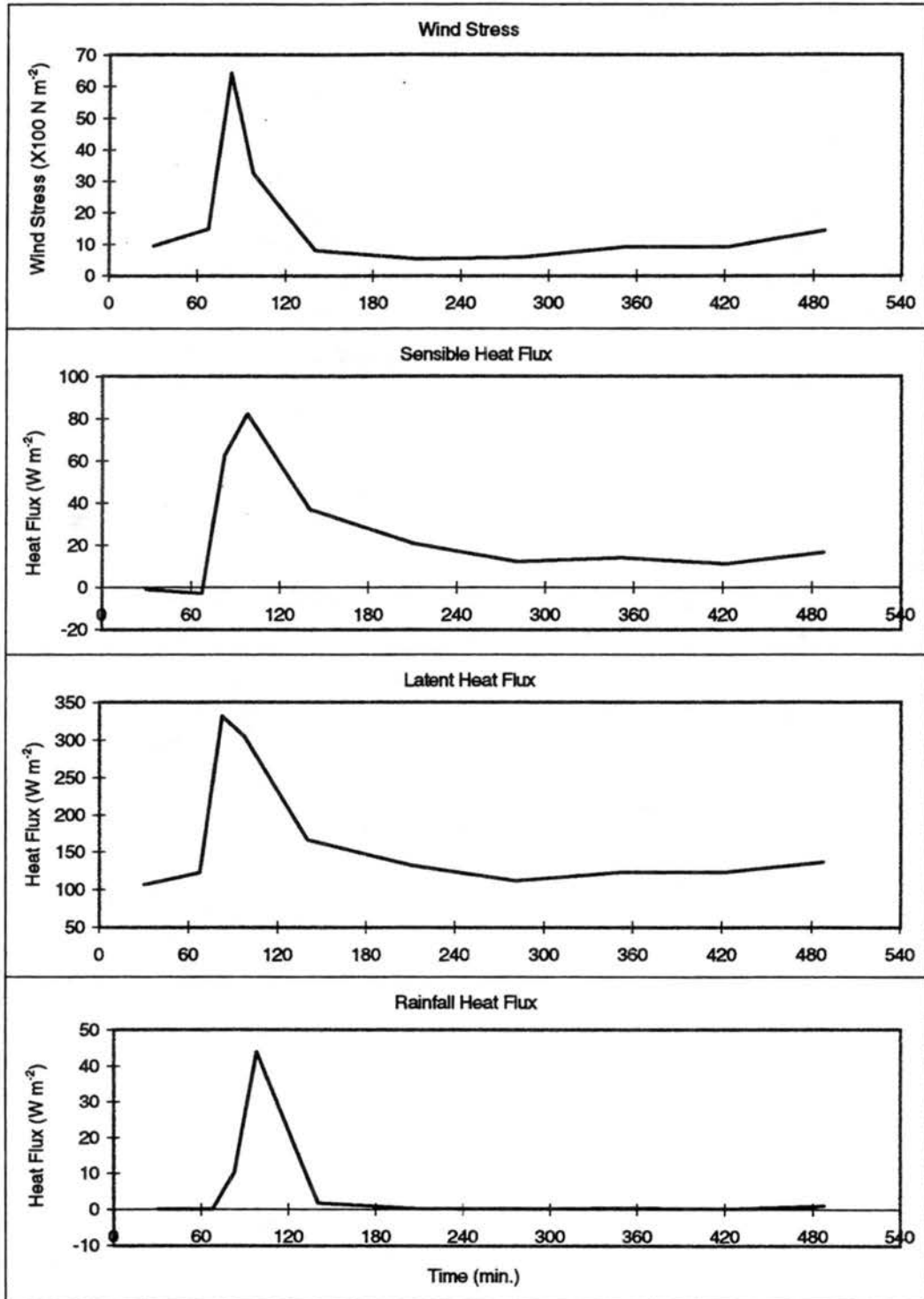
APPENDIX D

INDIVIDUAL MCS SCALE LINEAR EVENTS

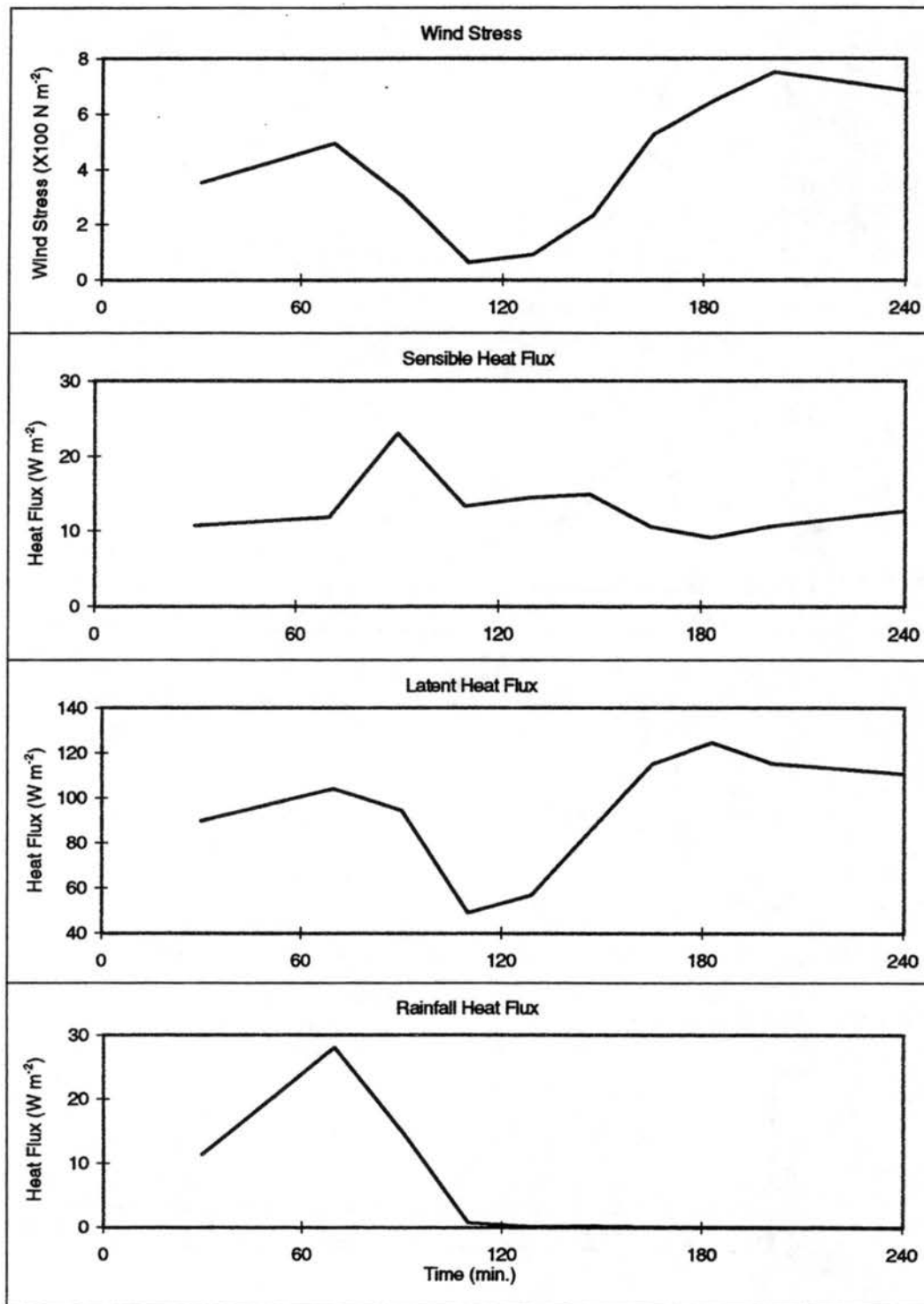
11 November 1992



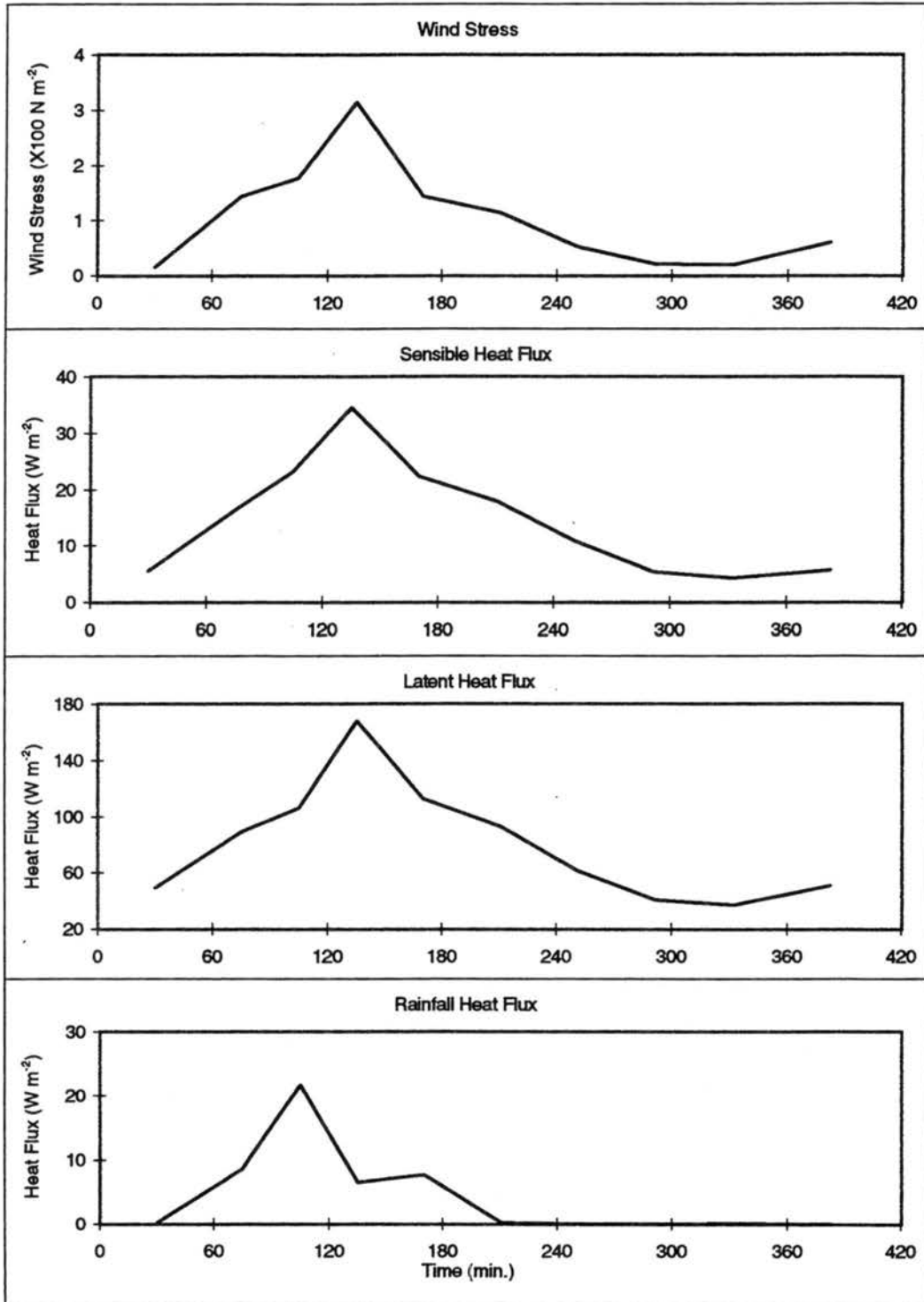
26 December 1992



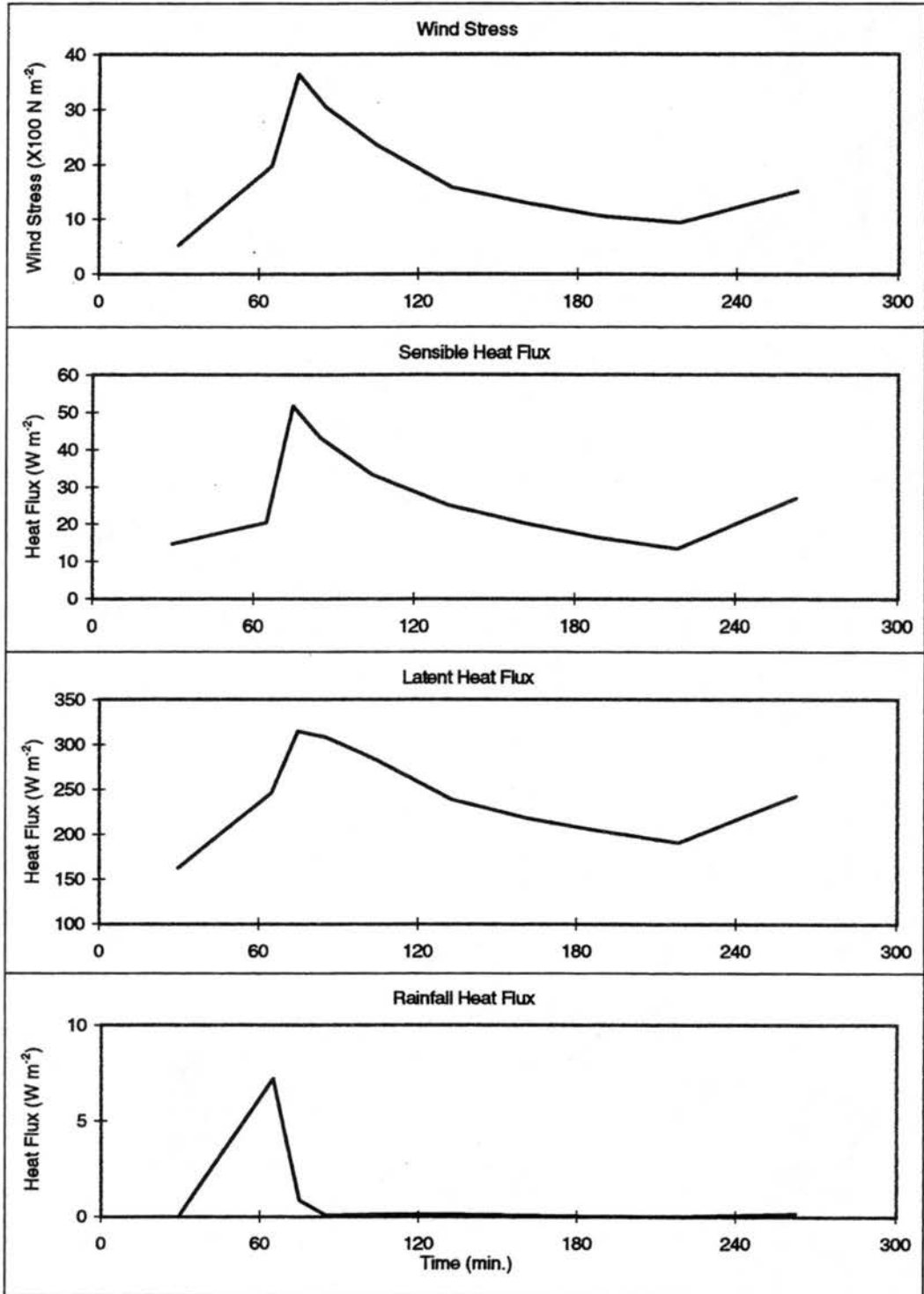
04 January 1993



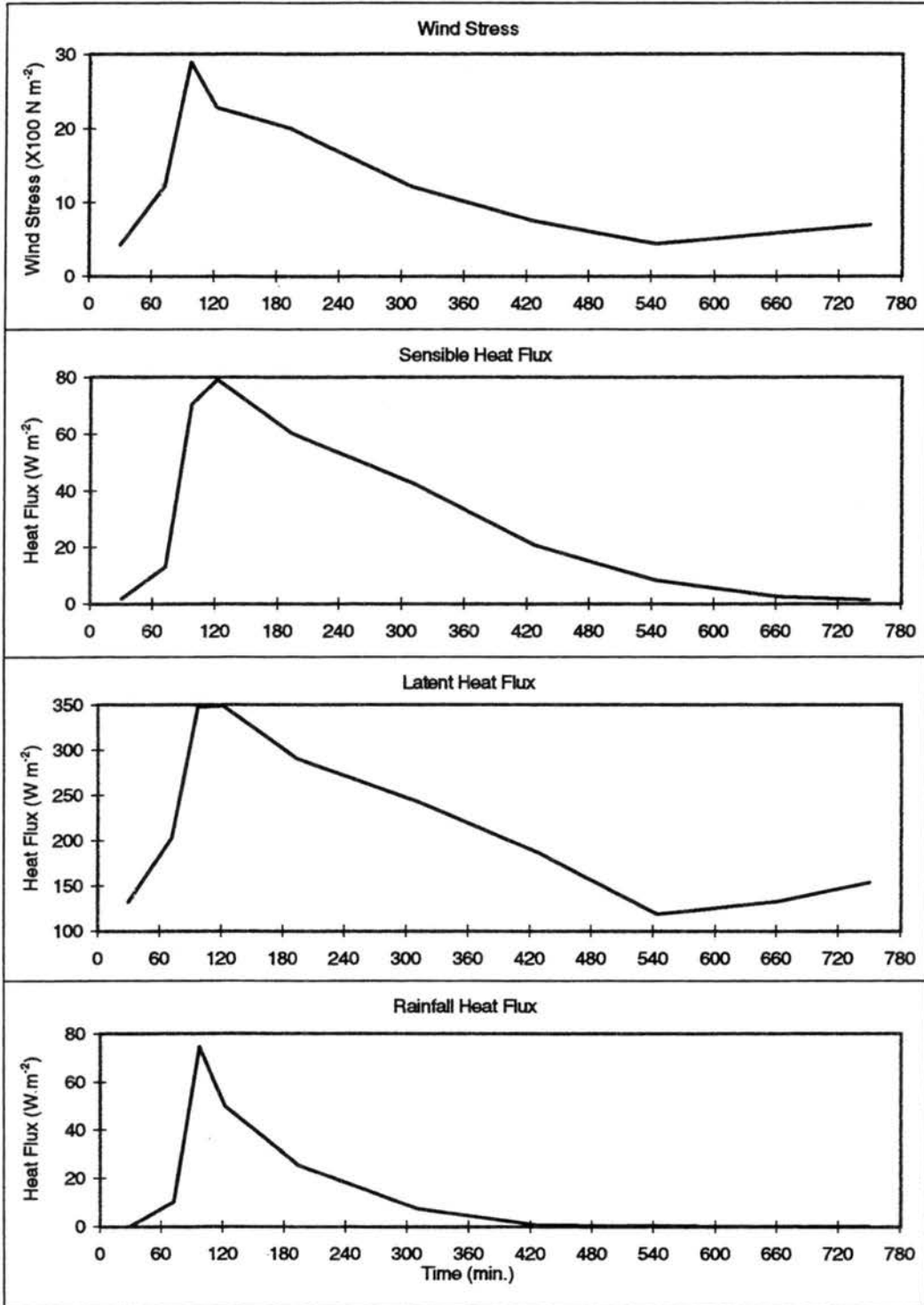
18 January 1993



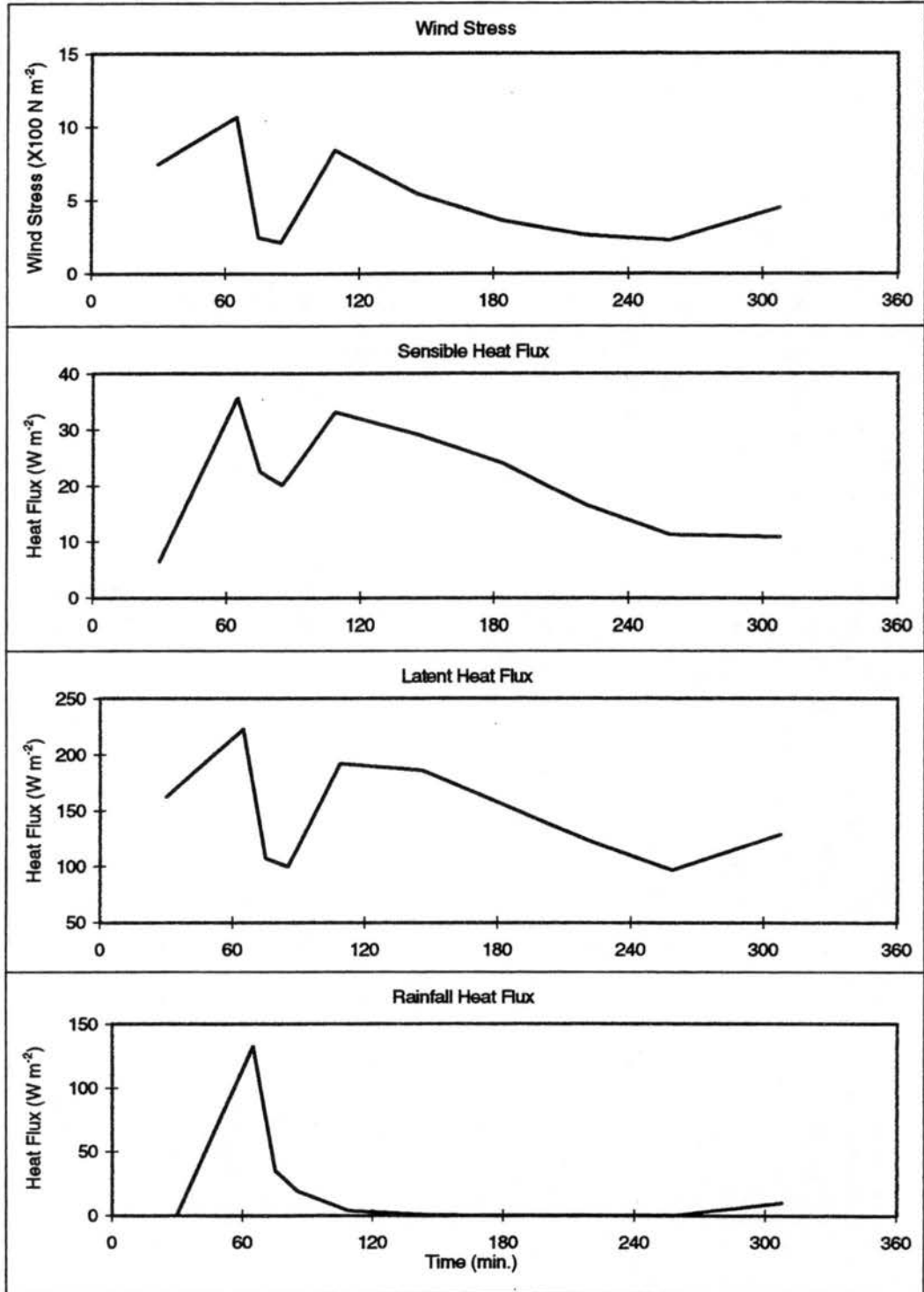
30 January 1993



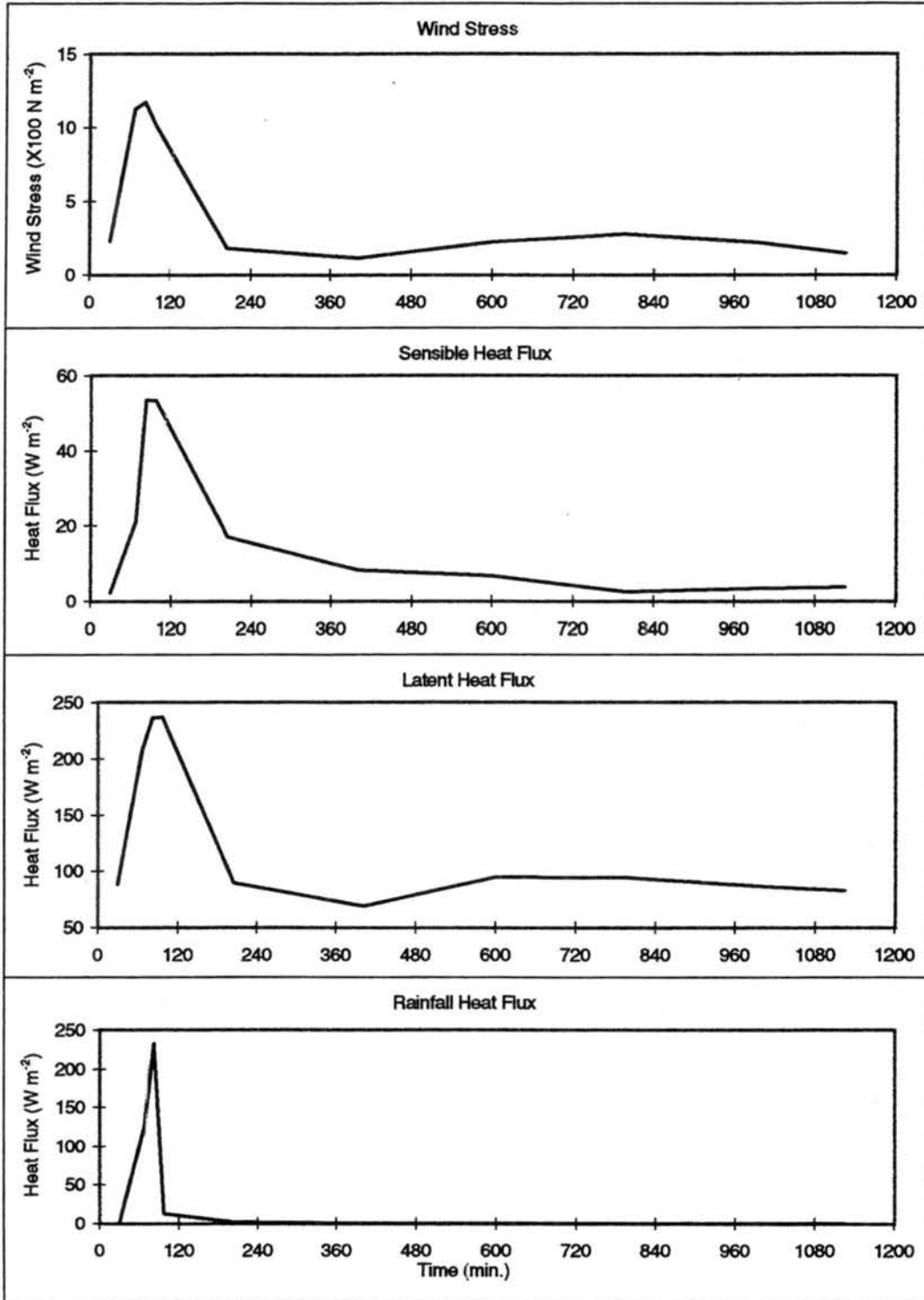
10 February 1993



11 February 1993



12 February 1993



19 February 1993

